Auroral Region Morphology and the Influence of Earth's Rotation on Geospace Dynamics

Margot Decotte

Thesis for the degree of Philosophiae Doctor (PhD)
University of Bergen, Norway
2024

UNIVERSITY OF BERGEN

Auroral Region Morphology and the Influence of Earth's Rotation on Geospace Dynamics

Margot Decotte

Thesis for the degree of Philosophiae Doctor (PhD)
at the University of Bergen

Date of defense: 07.06.2024

© Copyright Margot Decotte

The material in this publication is covered by the provisions of the Copyright Act.

Year: 2024

Title: Auroral Region Morphology and the Influence of Earth's Rotation on Geospace Dynamics

Name: Margot Decotte

Print: Skipnes Kommunikasjon / University of Bergen

Scientific environment

The research project presented in this Thesis was carried out at the Birkeland Centre for Space Science (BCSS) Norwegian Centre of Excellence (until its conclusion in 2023), within the Department of Physics and Technology at the University of Bergen, Norway. The project was funded by the Trond Mohn Foundation in the Starting Grant project "What Shapes Space?".

.

Acknowledgements

My PhD experience would have been significantly different without the guidance of my awesome supervisor and his eccentric ideas. Kalle, thank you for buying me more Legos than I could have ever dreamed of (it turned out to give me nightmares). It didn't exactly propel my side research –the so-called PhD– forward, but it was a true motivation to see happiness in your eyes every time we discussed the Lego project. Thank you also for being so supportive during moments of burnout and for introducing me to the concept of parallel working when I needed a break ☺. I'm not sure which world you live in, but I've come to appreciate it (not). Last but not least, thank you for saying one day: "I completely don't understand anything." If it didn't help much with the plots we were looking at, it made me feel much better about myself and life in general. I would also like to thank my co-supervisors Spencer and Jone. Thank you to the three of you, for your encouragement, mentorship, and patience. I can't believe I (almost) made it through this PhD without you noticing that I don't know anything and should have never gotten this job in the first place. To Hilde, thank you for always encouraging me to blame Kalle for everything. Ask him for a demonstration of *Earth's apparent varying rotation rate* (he says it's a thing) if you want to make him dance :).

To all my fellow fourth-floor PhDs, thank you for bringing joy and kindness into the office during this challenging journey. Your presence made the tough moments bearable and the good times memorable. Special thanks to the five fantastic humans who made all of this more than worth it. Michael, having you as a 24/7 mate was intense and I (mostly) loved it. I'm glad we made the best use of those plasma physics books during our tennis games on the staircase. I always win, but thank you for trying anyway. Eldho, you were the first to notice the mango in me, and I can't unsee the Elfo in you. Thank you for introducing me to your circle, it changed my life. Ingrid, you are a true gem, even if you prefer the atmosphere over space and even if you hold my gin hostage at your place (is there any left?). Simon, I couldn't have completed this PhD with my sanity intact (I'm totally okay) without your support and sweetness. You have been a ray of sunshine in Bergen's sky. A few more days to go, but so far still no suitcase in the office! (Update at D-2 before submission: the couch is not too bad). Finally, Jo, I don't know any English (nor French) words that would express the impact you've had on me. But I can tell one thing: you shaped my heart just as profoundly as the Earth's rotation shapes geospace ♡.

To all of you, thank you for being much more than just **cow**orkers. The most precious aspect of my PhD journey has been the friendship we've shared (and the Legos, obviously).

Lastly, to my parents, thank you for staying away from me... and giving me the space to pursue my dreams; your support means everything to me. Et à mes bestas sistas, amour toujours.

Margot
Bergen, 186274 breakdowns later


Sacrebleu!
I'm okey
GIN
AH!
Kamelåsa
That's what she said
coca cola no sugar

Sãcrêbleú, I'm okay

Abstract

The coupling between the solar wind, magnetosphere, and ionosphere is crucial for understanding the space environment and its impact on Earth. The Earth's polar upper atmosphere, and the auroral zone in particular, constitutes a region of convergence of the electromagnetic and kinetic energy provided by the magnetosphere. As such, the morphology of the region where auroral activity concentrates, typically known as the auroral oval, has been widely investigated in recent decades. The influx of charged particles guided by magnetic field lines connecting the magnetosphere and ionosphere, along with magnetic field disturbances, offer distinct perspectives on the aurora and, more broadly, on the solar wind-magnetosphere-ionosphere coupling.

This thesis aims to investigate the auroral region morphology, with a focus on asymmetries, to contribute to the understanding of the complex interplay between the magnetosphere and Earth's upper atmosphere. Notably, we place a large emphasis on elucidating the role of the planet's rotation in shaping convection flows within the magnetosphere, which in turn influence the auroral zone.

In Papers I and II, we develop a statistical method to characterise the auroral region morphology by deriving the occurrence probability of aurora based on measurements of particle precipitation (Paper I) and magnetic field fluctuations (Paper II) in the polar ionosphere. Despite major differences, these two studies reveal interesting common features in terms of spatial distributions in magnetic latitude and local time. Statistically, there is an extended region of high occurrence probability for both particle precipitation and magnetic field fluctuations, indicating large-scale, long-term patterns. This region of high probability forms, to first order, an oval around the pole and exhibits a dawn-dusk asymmetry, with a persistently wider oval in the dawn sector compared to dusk. In Paper I, we suggest that, from a fluid perspective, the width asymmetry in the occurrence probability of electron precipitation may reflect the amount of magnetospheric magnetic flux being convected around Earth. In this picture, the Earth's rotation could play a role in transporting more plasma toward dawn. Following this hypothesis, in Paper III, we estimate the extent to which magnetospheric plasma corotates at large distances from the ionosphere. We find that some regions in the magnetosphere follow Earth's rotation, despite a lag in the corotation velocity, while others are stationary. We show that the sub-corotation of the magnetospheric plasma may have broader implications in terms of ionospheric electrodynamics and magnetic field topology, further impacting the auroral region.

When considered as a whole, the studies constituting this thesis emphasise that electron precipitation and magnetic field fluctuations in the ionosphere can be used as indicators of the large-scale coupling between magnetospheric dynamics and auroral region. Our findings demonstrate that the dawn-dusk asymmetry in the auroral region is partly due to the Earth's rotation driving plasma more eastwards than westwards in the magnetospheric plasma sheet.

Sammendrag

Koblingen mellom solvinden, magnetosfæren, og ionosfæren er avgjørende for å forstå verdensrommet og dens påvirkning på Jorden. I de øvre lagene av atmosfæren ved polene, spesielt i området kjent som auroraregionen, møtes elektromagnetisk og kinetisk energi fra magnetosfæren. Dette området, ofte kalt auroraovalen, har blitt mye studert de siste tiårene. Strømmen av ladde partikler langs magnetfeltlinjer fra magnetosfæren til ionosfæren, og forstyrrelser i magnetfeltet, gir oss unike innsikter i auroraen og solvind-magnetosfære-ionosfære koblingen.

Denne avhandlingen undersøker formen og asymmetriene i auroraområdet for å bedre forstå det komplekse samspillet mellom magnetosfæren og jordens øvre atmosfære. Vi ser spesielt på hvordan jordens rotasjon påvirker strømmen av plasma i magnetosfæren, som igjen påvirker auroraen.

I Artikkel I og II utvikler vi en statistisk metode for å beskrive auroraområdets form ved å utlede sannsynligheten for forekomst av aurora basert på målinger av partikkelnedbør (Artikkel I) og svigninger i magnetifeltet (Artikkel II) i den polare ionosfæren. Til tross for store forskjeller, avslører studiene interessante felles trekk med hensyn til fordelinger i magnetisk bredde og lokal tid. Statistisk sett er det en utvidet region med høy forekomstsannsynlighet for både partikkelnedbør og magnetfeltsvingninger, noe som indikerer store, langsiktige mønstre. Denne regionen med høy sannsynlighet danner, i første orden, en oval rundt polen og viser en morgen-kveld asymmetri, med en vedvarende bredere oval i morgensektoren sammenlignet med kveld. I Artikkel I foreslår vi, fra et væskeperspektiv, at breddeasymmetrien i forekomstsannsynligheten for elektronnedbør reflektere mengden av magnetisk fluks i magnetosfæren som blir transportert rundt Jorden. Videre foreslår vi at jordens rotasjon kanskje spille en rolle i å transportere mer plasma mot morgesektoren. Basert på denne hypotesen, anslår vi i Artikkel III i hvilken grad det magnetosfæriske plasmaet koroterer med store avstander fra ionosfæren. Vi finner at noen regioner i magnetosfæren følger jordens rotasjon, til tross for en forsinkelse i korotasjonshastigheten, mens andre er stasjonære. Vi viser at sub-korotasjonen av det magnetosfæriske plasmaet kan ha bredere implikasjoner for hvordan ionosfæren og magnetfeltet oppfører seg, og påvirker auroraområdet.

Samlet sett viser disse studiene at observasjoner av elektronnedbør og magnetfeltsvingninger kan fortelle oss mye om samspillet mellom magnetosfæren og auroraområdet. Våre funn tyder på at forskjellen mellom morgen- og kveldssiden i auroraområdet delvis kan forklares med jordens rotasjon, som skyver plasmaet mer mot øst enn mot vest i det magnetosfæriske plasmaskjiktet.

List of Publications

This thesis consists of an introductory part (chapters 1 to 9), and a compilation of three scientific papers, either published or under review in international peer-reviewed journals.

Paper I M. Decotte, K.M. Laundal, S.M. Hatch, J.P. Reistad (2023), *Auroral Oval Morphology: Dawn-Dusk Asymmetry Partially Induced by Earth's Rotation*, JGR Space Physics, Vol. 128, Issue 6, doi: 10.1029/2023JA031345.

Paper II M. Decotte, K.M. Laundal, S.M. Hatch, J.P. Reistad (2024), *Occurrence probability of magnetic field disturbances measured with Swarm: Mapping the dynamic magnetosphere-ionosphere coupling*, JGR Space Physics, Vol. 129, Issue 2, doi: 10.1029/2023JA032191.

Paper III M. Decotte, K.M. Laundal, J.A. Salice, S.M. Hatch, S. Haaland, A. Ohma, *Revealing the effect of Earth's rotation on geospace*, Submitted to Nature Communications on 15-March-2024.

During my PhD studies, I have also contributed to the following papers:

A J.A. Salice, H. Nesse, N. Partamies, E. Kilpua, A. Kavanagh, M. Decotte, E.M. Babu, and C. Smith-Johnsen (2024), *The High-Energy Tail of Energetic Electron Precipitation: Solar Wind Drivers and Geomagnetic Responses*, Front. Astron. Space Sci., Vol. 11, doi: 10.3389/fspas.2024.1352020.

B S.J. Walker, K.M. Laundal, J.P. Reistad, A. Ohma, S.M. Hatch, G. Chisham, M. Decotte (2024), *A Comparison of Auroral Oval Proxies With the Boundaries of the Auroral Electrojets*, Space Weather, Vol. 22, doi: 10.1029/2023SW003689.

C A. Ohma, K.M. Laundal, M. Madelaire, S.M. Hatch, S. Gasparini, J.P. Reistad, S.J Walker, M. Decotte, *Robust estimates of spatiotemporal variations in the auroral boundaries derived from global UV imaging*, JGR Space Physics (in production as of 12-April-2024), doi: 10.1029/2023JA032021.

Contents

Scientific environment i

Acknowledgements iii

Abstract vii

Sammendrag ix

List of Publications xi

1 Introduction 1

2 The Solar wind – magnetosphere – ionosphere coupling 7
2.1 The fluid perspective . . . 7
2.2 Solar wind - magnetosphere coupling . . . 8
2.3 Plasma Circulation in the magnetosphere-ionosphere system . . . 10
2.3.1 The Dungey cycle . . . 10
2.3.2 Expanding-contracting polar cap paradigm . . . 11
2.3.3 Plasma circulation on other planets . . . 13
2.3.4 Convection and currents in the polar ionosphere . . . 15
2.3.5 Magnetospheric substorms . . . 18
2.4 The auroral region . . . 19
2.4.1 Auroral particle precipitation . . . 19
2.4.2 Dynamics and morphology of the auroral region . . . 23
2.5 Fluid versus kinetic descriptions of the plasma . . . 24

3 Data 27
3.1 Particle precipitation – DMSP/SSJ . . . 27
3.2 Magnetic field in space – Swarm/VFM . . . 28
3.3 Magnetospheric convection – Cluster/EDI . . . 30
3.4 Solar wind properties and geomagnetic activity indices – OMNI . . . 31
3.5 Substorm epochs . . . 31

4 Methods 33
4.1 Auroral boundary detection based on Sun-synchronous satellites: The local time bias issue . . . 33
4.2 Auroral occurrence probability (AOP) . . . 34
4.2.1 Concept . . . 34
4.2.2 Auroral electron precipitation occurrence probability (POP) . . . 34
4.2.3 Disturbed magnetic field occurrence probability (dBOP) . . . 35
4.2.4 MLT variation of POP and dBOP . . . 36
4.3 Corotation in the magnetosphere . . . 37
4.3.1 Convection velocity maps . . . 37

4.3.2 Corotation MLat profiles 37
4.3.3 Potential implications on ionospheric electrodynamics 39
4.4 Uncertainties 41

5 Summary of papers **43**

6 Conclusions and future trajectories **47**

7 LEGO model of the magnetosphere **51**
7.1 Principle 51
7.2 Development 52
7.3 Result 52

List of abbreviations **55**

Bibliography **55**

Scientific results **71**
Paper I 73
Paper II 93
Paper III 115

1 Introduction

The Sun continually releases energy through a flux of charged particles known as the solar wind. The Sun's magnetic field lines are frozen into the solar wind as the latter propagates away from the star into interplanetary space. When in proximity to magnetised planets (notably Earth, but also Jupiter and Saturn, for example), the solar wind and its embedded interplanetary magnetic field (IMF) interact with the celestial body's magnetic environment – the magnetosphere –, inducing changes in its configuration. At Earth, the inner magnetosphere, located near the planet's surface, exhibits a dipole shape, while the influence of the solar wind causes the outer magnetosphere to deviate from this dipolar configuration. The outer magnetosphere is positioned at around 10 Earth radii (R_E) on the dayside (facing the Sun) and extends over hundreds of R_E on the nightside, forming the region referred to as the magnetotail. The solar wind plasma is consequently mainly deflected around the magnetosphere, and separated from the geomagnetic field by the magnetopause. Although this boundary restricts mass, momentum, and energy transfers between the two environments, the solar wind plasma may penetrate into the magnetosphere when the interplanetary and planetary magnetic field lines merge on the dayside. This process is known as dayside reconnection and results in the opening of Earth's magnetic field lines to interplanetary space. Open field lines are subsequently dragged to the nightside to form the magnetospheric lobes, where the kinetic energy from the solar wind is converted into magnetic energy. This is followed by a rearrangement of magnetic field lines in the magnetotail, namely nightside reconnection. These magnetic reconnections initiate a large-scale movement of plasma within the Earth's magnetosphere, which, according to the prevailing paradigm, is largely governed by the solar wind and IMF conditions (*Cowley and Lockwood*, 1992). Figure 1.1 shows an artist's view of the solar wind and Earth's magnetosphere.

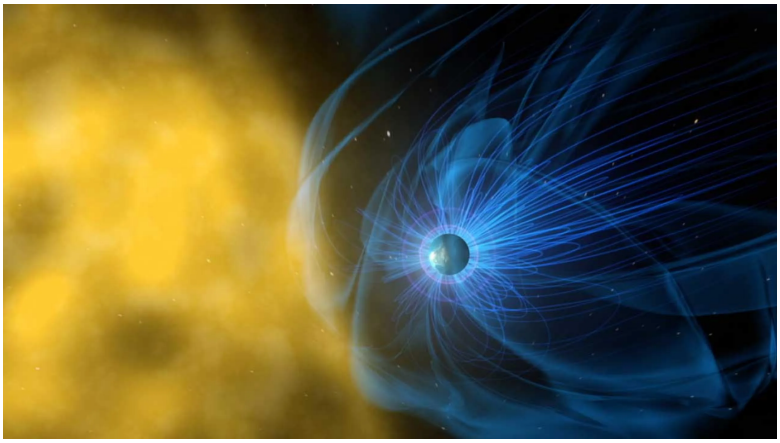

Figure 1.1: NASA illustration of the solar wind interacting with the magnetosphere surrounding Earth.

The dynamics of the magnetosphere and its internal plasma transport significantly influence the planet's upper atmosphere. In particular, the ionosphere – a region where a significant fraction of the atmosphere's constituents are ionised, as opposed to the neutral atmosphere – has an intricate relationship with the magnetosphere, commonly identified as magnetosphere-ionosphere (M-I) coupling (*Blanc*, 1988). Various phenomena contribute to geospace dynamics. Particularly, currents and wave propagation play crucial roles in facilitating the exchange of energy, mass, and momentum between the magnetosphere and ionosphere (*Vasyli*, 2012; *Thayer and Semeter*, 2004; *Borovsky and Valdivia*, 2018). Additionally, the transfer of magnetic energy into kinetic energy during nightside reconnection drives charged particles towards Earth. As protons and electrons travel along magnetic field lines with footpoints in the polar ionosphere, they may precipitate and collide with atmospheric constituents such as oxygen and nitrogen, ultimately leading to the formation of light displays known as aurora (see Figure 1.2).

The aurora has been observed by humans for thousands of years. One of the earliest scientific descriptions of the Aurora Borealis ("Northern Dawn", in Latin) was documented by Galileo Galilei in the 1600s. The next couple of centuries saw more systematic observations and the development of mathematical models to explain the aurora. In particular, in the late 19th – early 20th centuries, Kristian Birkeland, a Norwegian scientist and early pioneer in space physics, made significant contributions to our understanding of the interactions between the solar wind, Earth's magnetosphere, and aurora. With the advent of space exploration in the mid-20th century, the deployment of satellites and high-altitude rockets equipped with instruments and sensors provided a new perspective on the aurora and marked a significant advancement in our knowledge of auroral phenomena and their connection to magnetospheric dynamics. Auroral studies led to the establishment of the auroral oval concept in the 1960s (*Feldstein*, 2016). More recent advances in technology, including satellite observations, ground-based instruments, numerical simulations, and modelling, have allowed for more detailed and comprehensive studies of the aurora. It is now generally accepted that the auroral region exhibits an approximate oval shape, at high latitudes, centered around the magnetic poles (*Zmuda*, 2012). Additionally, it is well known that the intensity and extent of the auroral region are governed by geomagnetic activity (*Akasofu*, 1963). However, the precise dynamics of the boundaries of the auroral region, and, thereby, the interconnection between magnetospheric mechanisms and auroral region morphology, remain an active field of research (*Ohma et al.*, 2023).

Objectives The underlying purpose behind most space physics studies is to enhance our predictive capabilities regarding the variety of dynamic complex events occurring in the near-Earth space environment that are influenced by the Sun – commonly referred to as space weather events. A comprehensive understanding of space weather is indispensable for forecasting and minimizing potential impacts on communication, navigation, and other technologies reliant on space-based infrastructure.

On a less pragmatic yet fascinating note, space weather also significantly impacts auroral phenomena. In fact, the connections between magnetospheric dynamics and the auroral region morphology serve as the focal point of the investigations carried out in this thesis. Ultimately, the aim is to unravel the complexities of the M-I coupling. Moreover, while conventional approaches often overlook the impact of planetary rotation in favour of the

solar wind's influence, we place a particular emphasis on understanding the effect of Earth's rotation in shaping the near-Earth space environment.

The overarching research questions guiding the work conducted in this thesis can be summarised as follows:

- **What do ionospheric observations from the auroral region tell us about magnetospheric dynamics?**
- **What is the influence of Earth's rotation on shaping the auroral region?**

The papers composing this thesis aim to provide insights into these questions by addressing specific aspects.

In Paper I, our main emphasis is on analysing the morphology of the auroral region in terms of asymmetries between dawn and dusk. Using a large dataset of ionospheric electron energy flux measurements, we derive the occurrence probability of detecting aurora in the polar region and examine the variation in auroral extent depending on the magnetic local time and geomagnetic conditions. Assuming a topological mapping between auroral electron precipitation and the magnetosphere, we implement a simple fluid model representing the magnetospheric magnetic flux to explore the potential role of Earth's rotation in shaping the asymmetric auroral region.

Paper II aims to further explore the auroral zone morphology and investigate connections between magnetic perturbations measured in the polar ionosphere and magnetospheric dynamics. We analyse the occurrence probability of detecting substantial magnetic field fluctuations across various frequency bands and external conditions, and determine which mode of the M-I coupling (direct/dynamic or indirect/large-scale steady-state) is represented by each frequency range. Furthermore, we evaluate whether magnetic field fluctuations can serve as a proxy for the auroral region by comparing their spatial occurrence probability distribution with that of auroral electron precipitation from Paper I.

Paper III builds upon the findings of the two preceding papers and concentrates on uncovering the influence of Earth's rotation on the magnetosphere and the auroral region. We seek to empirically validate the hypothesis proposed in Paper I, which suggests that Earth's rotation plays a role in the transport of magnetic flux within the magnetosphere. Using magnetospheric convection measurements, we measure the in-situ eastward velocity and assess the degree of synchronisation between Earth's rotation and plasma motion across different regions of the magnetosphere. We further relate our findings to the auroral zone and the dawn-dusk asymmetry observed in Papers I and II.

Outline Chapter 2 offers a thorough review of the current understanding of the mechanisms and main features of the coupling between the solar wind, magnetosphere, and ionosphere, with a particular focus on the auroral region. Basic concepts in space plasma physics are introduced along the way, and the chapter concludes with a discussion on the contrasting fluid and kinetic descriptions of plasma within the M-I system. Ultimately, this chapter provides the reader with the theoretical framework necessary for understanding the research papers forming the core of this thesis. Chapter 3 describes the data employed in this thesis, and Chapter 4 outlines the methodologies used to de-

rive the results presented herein. The uncertainties related to the data and methods are discussed at the end of Chapter 4. Detailed summaries of the three papers constituting the thesis are given in Chapter 5. In Chapter 6, we establish a clear connection between the central questions and objectives posed in this thesis and the insights emerging from the trio of papers comprising the body of this work. Expanding upon the main findings, prospective research is also briefly discussed in this chapter. Finally, the three papers are showcased in the last chapter of this thesis.

Figure 1.2: Aurora in Longyearbyen, Svalbard.

2 The Solar wind – magnetosphere – ionosphere coupling

This chapter provides the scientific foundation to understand the fundamental interactions between the solar wind, magnetosphere and ionosphere that shape the geospace and auroral region. Most of the concepts presented in the following chapter rely on a fluid description of the plasma in the system. Section 2.1 introduces the basic space plasma physics principles associated with such a fluid perspective. Section 2.2 reviews essential aspects of the coupling between the solar wind and magnetosphere. Section 2.3 describes how magnetospheric and ionospheric dynamics are connected through plasma circulation. Section 2.4 details the fundamental features of the auroral region. Finally, Section 2.5 concludes the chapter with a discussion regarding the benefits and limitations of the fluid and kinetic approaches.

2.1 The fluid perspective

A plasma is an ionised gas in which electrons and ions are approximately in equal abundance and move freely within the system. While plasmas are most accurately described by particle distribution functions derived from kinetic theory, analysing their macroscopic quantities, such as density, momentum and energy, gives further insight into the plasma's physical properties. This approach is particularly valid when investigating the large-scale dynamics of plasmas, as they are governed by collective behaviours rather than individual particle interactions.

Magnetohydrodynamics (MHD) is widely used in physics to describe the macroscopic behaviour of electrically conducting fluids, such as plasmas, in the presence of a magnetic field. In MHD, conservation laws for mass, momentum and energy are coupled with Maxwell's equations, which describe the interaction between charged particles and electromagnetic fields. MHD principles provide a useful framework for describing many large-scale plasma phenomena from a fluid perspective (e.g., *Parker*, 1996; *Vasyli*, 2010).

In MHD, the plasma is treated as a single fluid with mass density $\rho = n_i m_i + n_e m_e \approx n m_i$ under the quasi-neutral approximation ($n_i \approx n_e \approx n$), where only one ion species is considered. In the ideal MHD approximation, more assumptions are made to simplify the description. Notably, the plasma is assumed to be a perfectly conducting adiabatic fluid, i.e., the electric charges move freely without any diffusion or dissipation and there is no heat exchange with the plasma's surroundings. The plasma is also considered collisionless, meaning that the particles primarily interact through electromagnetic forces rather than collisions with each other. Additionally, the frozen-in assumption states that, in an ideal MHD plasma, the magnetic field lines are frozen into the plasma. That means that the bulk motion of plasma does not cross magnetic field lines. In other words, as long as the ideal MHD approximation holds, the magnetic field lines remain frozen in the plasma, and any movement or deformation of the plasma will carry the magnetic field lines along with it. In turn, the magnetic field exerts tension and pressure forces back on the plasma.

The frozen-in assumption is fundamental for understanding plasma convection and the dynamics of the solar wind interacting with the magnetosphere. Ideal MHD conditions are typically valid in the solar wind, magnetosphere and upper ionosphere (*Schunk and Nagy*, 2018). However, some exceptions arise in the magnetosphere, for example in regions of magnetic reconnection and acceleration of auroral particles (*Baumjohann and Treumann*, 2012). In such regions, ideal MHD falls short of capturing the complexity of plasma behaviour.

In summary, the fluid description allows for a conceptual understanding of the large-scale plasma dynamics in the magnetosphere. In the subsequent sections, the coupling between the solar wind, magnetosphere and ionosphere is explored from a fluid perspective. However, we will see that a kinetic treatment is required when describing auroral dynamics. In Section 2.5, we elaborate on the fluid approximation, further highlighting its benefits and limitations.

2.2 Solar wind - magnetosphere coupling

The solar wind plasma and its frozen-in magnetic field (the IMF) transport energy and mass from the Sun to the Earth. Upon reaching the magnetic environment surrounding Earth, the IMF and geomagnetic field interact through complex mechanisms.

The Earth's magnetic field deflects most of the solar wind, thereby creating the magnetopause, a boundary determined by the pressure balance between the solar wind and the geomagnetic field. However, at the front magnetopause, interplanetary and geomagnetic field lines can reconnect if they have anti-parallel components, giving the magnetosphere its characteristic shape and transferring parts of the solar wind energy and mass to the magnetospheric plasma population. Figure 2.1 illustrates the magnetosphere's characteristic shape, main regions and magnetic reconnection sites. Figure 2.2 shows the flanks of the magnetosphere, as seen from the tail, in an attempt to capture its 3D aspect.

The IMF orientation controls the reconnection geometry. A pure southward pointing IMF gives the most suitable configuration for reconnection at the subsolar point (defined by the intersection of the Earth-Sun axis and the magnetopause). However, IMF orientations with a northward component can also result in reconnection at the magnetopause, generally at higher latitudes compared to the subsolar point, in the lobes (*Frey et al.*, 2019).

Numerous attempts have been made to characterise the efficiency of magnetic reconnection at the magnetopause in terms of energy transfer between the solar wind and the magnetosphere (e.g. *Perreault and Akasofu*, 1978; *Kan and Lee*, 1979; *Wygant et al.*, 1983; *Milan et al.*, 2012). A commonly used proxy is the Newell's coupling function (*Newell et al.*, 2007):

$$\epsilon_N = v^{4/3} \left(\sqrt{B_y^2 + B_z^2} \right)^{2/3} \sin^{8/3} (\theta_c/2) \,, \tag{2.1}$$

where v denotes the solar wind speed, B_y and B_z are components of the IMF in the Geocentric Solar Magnetospheric (GSM) coordinate system and $\theta_c = \arctan2(B_y, B_z)$ is the IMF clock angle. In GSM coordinates, the X-axis points from the centre of Earth

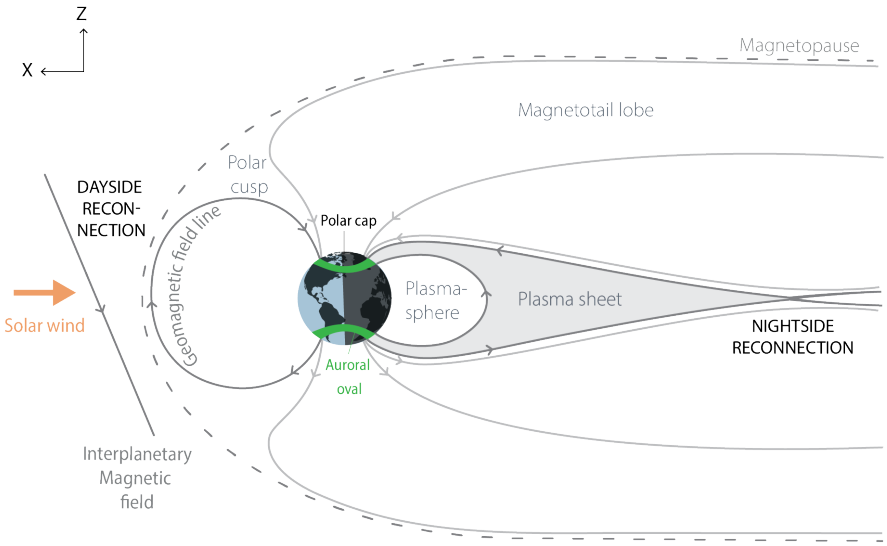

Figure 2.1: Illustration of the geospace in the XZ plane. *Adapted from Paper I.*

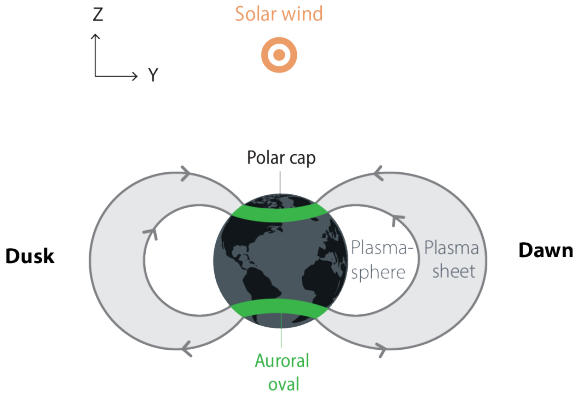

Figure 2.2: Same as Figure 2.1 but in the YZ plane, as seen from the magnetotail.

towards the Sun, the XZ plane contains the Earth-Sun line and the magnetic dipole axis, and the Y-axis points towards dusk, perpendicular to the XZ plane (*Laundal and Richmond*, 2017). In this system, "northward" and "southward" oriented magnetic field relate to IMF $B_z > 0$ and $B_z < 0$, respectively (*Milan*, 2015).

While the process of magnetic reconnection is usually described by kinetics, its effects can be effectively interpreted within a fluid framework (see the following sections).

2.3 Plasma Circulation in the magnetosphere-ionosphere system

The magnetic reconnection process between the IMF and Earth's magnetosphere reconfigures field lines, resulting in the redistribution of plasma and magnetic flux within the magnetosphere (*Cowley*, 1981). This, in turn, primarily controls the M-I coupling (*Moore et al.*, 1989).

2.3.1 The Dungey cycle

The Dungey cycle describes a steady-state magnetic flux transport in the magnetosphere, initiated by the dayside reconnection between the IMF and closed geomagnetic field lines (*Dungey*, 1961).

The dayside reconnection comes with the opening of the previously closed terrestrial magnetic flux. The open magnetic field lines are still connected to Earth but at one end only, while the other end is connected to the solar wind. As the magnetic field is frozen into the plasma, the newly open magnetic field lines are dragged anti-sunward by the solar wind flow and stretched hundreds of R_E, forming the magnetotail lobes on the nightside of Earth. Magnetic field lines have opposite orientations between the Northern and Southern Hemisphere lobes. Consequently, they can merge again and close the open magnetic flux, such that the newly closed field lines have both footpoints on Earth. This process is referred to as nightside reconnection. The closed field lines form a region in the magnetotail known as the plasma sheet.

During nightside reconnection, the magnetic energy stored in the lobes is transferred to the plasma sheet, resulting in a bursty (i.e., not steady state) flux of plasma towards the Earth. As the plasma flow approaches the Earth, the stretched field lines forming the plasma sheet become more and more dipolar. Upon reaching just a few R_E, the plasma is finally diverted towards the flanks of the magnetosphere (see Figure 2.2). The Dungey cycle is completed as the closed flux proceeds to the dayside, where the magnetic field lines can once again merge with the IMF and start a new cycle. Figure 2.3 summarises the different stages of the Dungey cycle.

Since plasma and magnetic fields largely move together in the magnetosphere and ionosphere (i.e., frozen-in condition), the global plasma circulation in the magnetosphere, as described by the Dungey cycle, consequently maps down to the ionosphere. We return to this in Sections 2.3.2 and 2.3.4.

The Dungey cycle is a simplistic model that does not capture all aspects of the complex solar wind-magnetosphere interactions and subsequent dynamics. For example, it assumes identical rates of dayside and nightside reconnection and does not describe the

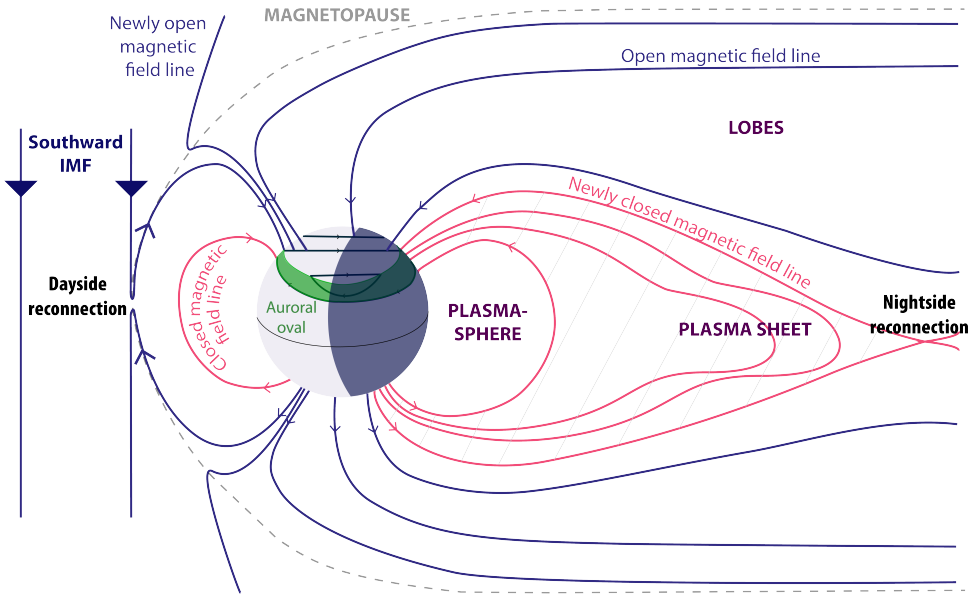

Figure 2.3: Schematic illustration of the Dungey cycle, which describes the large-scale circulation of plasma and magnetic flux initiated by dayside reconnection between interplanetary and geomagnetic field lines, during southward IMF. The solar wind comes from the left. Open and closed magnetic field lines are shown in blue and red, respectively.

plasma circulation driven by a northward IMF. However, despite its limitations, the Dungey model provides a fundamental framework for understanding the coupling between the solar wind and the Earth's magnetosphere.

2.3.2 Expanding-contracting polar cap paradigm

The Expanding-Contracting Polar Cap (ECPC) paradigm is a modern view of the Dungey cycle in which the convection is described in relation to reconnection, magnetic flux transport within the magnetosphere, associated polar ionospheric flows and changes of the polar cap size (*Cowley and Lockwood*, 1992; *Milan*, 2015). In this model, the magnetosphere is topologically connected to the ionosphere, and dayside and nightside reconnection processes are no longer assumed to occur at the same rate.

In the ionosphere, there is a magnetic boundary between the regions of open and closed magnetic field lines. This boundary is referred to as the "open-closed boundary" (OCB), and further delimits the polar cap. Figures 2.1 and 2.3 depict the mapping between magnetospheric regions and the ionosphere. The open magnetic field lines forming the magnetotail lobes map to the polar cap, while the closed magnetic field lines constituting the plasma sheet map equatorward of the OCB.

The auroral oval is the preferred region for the precipitation of particles originating from the magnetospheric plasma sheet, which often results in auroral activity (see Section 2.4). In the ECPC paradigm, OCB and poleward boundary of the auroral oval correspond to the same limit, which is a widely used assumption. Since the amount of open flux varies

throughout the Dungey cycle, the size of the polar cap varies and so does the location of the OCB, consequently impacting the auroral region. Specifically, the opening of magnetic flux results in the OCB being displaced equatorward. Conversely, the closure of magnetic flux leads to a decrease in the polar cap surface and shifts the OCB poleward. Therefore, monitoring the polar cap size provides a reliable method for assessing the balance between dayside and nightside reconnection rates (*Siscoe and Huang*, 1985).

The ECPC paradigm primarily predicts the size of the polar cap. In a simplistic extension of this model, we posit that the auroral region expands and contracts at a rate proportional to the nightside and dayside reconnection rates. Figure 2.4 demonstrates the variation in polar cap (P) and auroral oval (A) areas (fluxes) along with the corresponding displacement of OCB (red line) associated with variations in the open/closed flux. In Figure 2.4 (a), the low latitude OCB is characteristic of a period of greater reconnection rate on the dayside compared to the nightside. The hashed area illustrates the contraction of the polar cap following an impulse of nightside reconnection (closure of flux), and the associated expansion of the auroral oval. In contrast, the OCB lies at higher latitudes in Figure 2.4 (b), indicative of a period of higher nightside reconnection rate compared to the dayside. This time the hashed area depicts an impulse of dayside reconnection (opening of flux), leading to the expansion of the polar cap, which consequently reduces the size of the auroral oval.

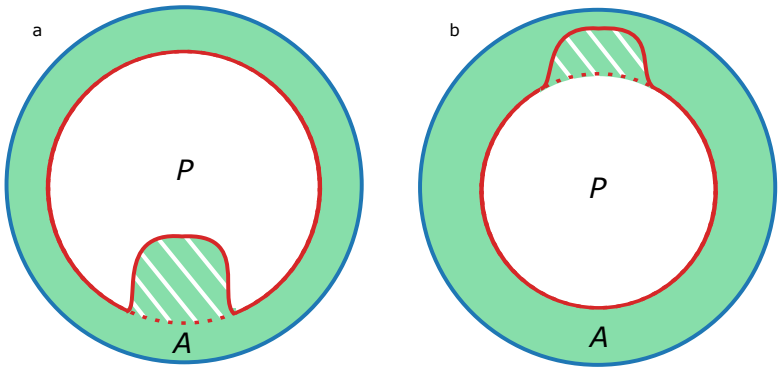

Figure 2.4: Expanding-contracting polar cap and auroral oval, viewed from above the pole; a) contraction of the polar cap in response to nightside reconnection b) expansion of the polar cap in response to dayside reconnection. The OCB is represented by the red line, encircling the polar cap and delimiting the poleward edge of the auroral oval. *Taken from Ohma et al. (2023).*

This model of auroral flux is applied in Paper I to represent the 1D steady-state plasma sheet magnetic flux. However, the notion that dayside reconnection reduces the spatial extent of the aurora was found to be either too simplistic or undetectable by the UV camera on the Imager for Magnetopause-to-Aurora Global Exploration (IMAGE) satellite (*Ohma et al.*, 2023).

Many studies have explored the intricate connection between magnetospheric processes, OCB position and auroral region dynamics (e.g. *Milan et al.*, 2003; *Newell et al.*, 2004; *Laundal et al.*, 2010; *Milan*, 2015; *Chisham et al.*, 2022). In contrast, the current knowledge about the equatorward boundary of the auroral oval and its behaviour within the

framework of the ECPC paradigm remains limited. While it has been shown to evolve over longer time scales than the auroral oval poleward boundary (*Ohma et al.*, 2023), there is no established model or standardised method for predicting the location of the equatorward boundary. A better understanding of the full spatial distribution of the auroral region is crucial for a thorough comprehension of M-I dynamics (see Section 2.4).

Equatorward of the auroral oval, the low to mid-latitude ionosphere maps to the magnetospheric plasmasphere (see Figure 2.1–2.3). This region is characterised by a cold, dense plasma environment, where magnetic field lines have a dipole-like configuration. Located in the inner magnetosphere (plasmapause at about $2 - 7$ R_E (*Moldwin et al.*, 2002)), the plasmasphere is only occasionally directly impacted by interactions between the solar wind and magnetosphere. Nevertheless, it is commonly accepted that the rotation of the Earth impacts the plasma circulation in this region (*Sandel et al.*, 2003; *Burch et al.*, 2004) (see also Sections 2.3.3 and 2.5 regarding the influence of planetary rotation on plasma convection).

2.3.3 Plasma circulation on other planets

The Dungey cycle predominantly influences magnetospheric convection on slow-rotating planets like Earth and Mercury (*Dungey*, 1961; *Slavin et al.*, 2009; *Blanc et al.*, 2005). Conversely, on Jupiter and Saturn, which are rapid rotators with strong magnetic fields, plasma convection is primarily driven by the planetary rotation and the solar wind only plays a minor role (*Gombosi et al.*, 2009). Since the papers constituting this thesis emphasise the influence of Earth's rotation on geospace, we consider the dynamics of Jupiter and Saturn more closely.

In the Jovian and Kronian magnetospheres, the plasma primarily originates from the moons' activity (internal mass loading). As the magnetospheric plasma is transported by corotation into the nightside tail, there is an outward transport of mass which ultimately enables the release of plasma by magnetotail reconnection. This process constitutes the Vasyliunas cycle (*Vasyliunas*, 1983; *Gombosi et al.*, 2009; *Xu et al.*, 2021).

During a transit of the magnetotail, magnetospheric flux tubes filled with plasma (closed field lines) rotate from the dayside around the dusk flank. As they progress towards the nightside, the mass-loaded flux tubes are gradually elongated into the tail under the effect of inertia (centrifugal force) of their mass content. On the nightside, the outward mass transport leads to significant stretching of the field lines, resulting in their break off (through magnetic reconnection) and release of their plasma content into a plasmoid. Subsequently, the field lines in the tail lobes may reconnect, sunward of the plasmoid. This process ejects the plasmoid down the tail and concurrently generates empty closed flux tubes that can be convected back towards the planet. The cycle of magnetic flux transport is completed as the closed field lines corotate back to the dayside via the dawn flank (return flow) (*Southwood et al.*, 2015; *Gombosi et al.*, 2009; *Vogt et al.*, 2020; *Xu et al.*, 2021; *Forsyth et al.*, 2010).

Figure 2.5 illustrates the Vasyliunas cycle. On the left panel, the magnetosphere is seen from above, in the XY (equatorial) plane, with the Sun on the left, while the right panel shows a sequence of meridional cuts of the magnetotail, during its rotation around the

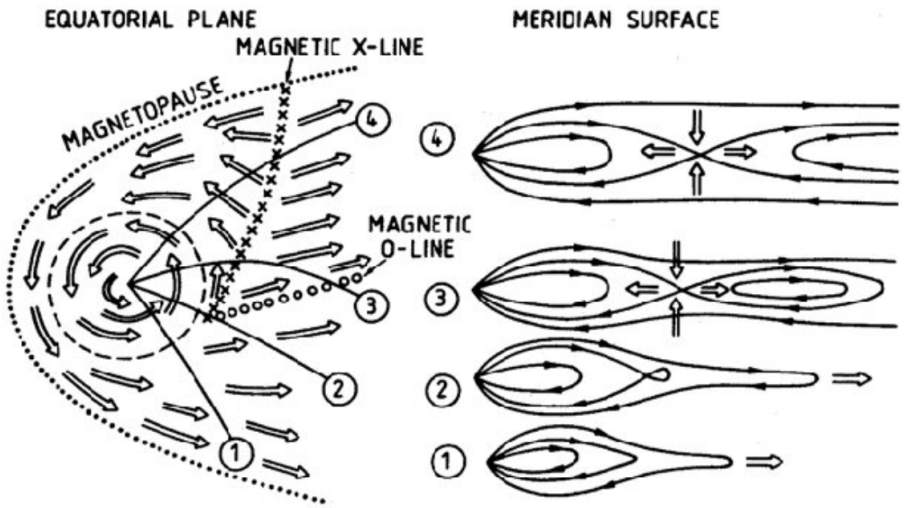

Figure 2.5: Schematic representation of the Vasyliunas cycle. The corotating plasma flow is shown in the equatorial plane on the left panel. At right, the sequence of meridional cuts shows the plasma flow and associated magnetic field lines configuration, ultimately leading to magnetic reconnection and release of a plasmoid. *Original Source: Vasyliunas (1983) (taken from Gombosi et al. (2009)).*

planet. The plasma flow and associated closed magnetic field lines forming the tail of the magnetosphere transit from dayside to nightside towards dusk and return to the dayside towards the dawn flank. On the dayside, the plasma motion is contained by the magnetopause, such that the magnetic field lines follow a corotation-like motion around the planet (steps $1-2$). This phase involves the stretching of field lines into the magnetotail. On the nightside, where dynamic pressure from the solar wind is absent, the plasma encounters less resistance and tends to move outwards, dragging the field lines along until reaching the magnetic O-line. There, the field lines form a magnetic loop and produce a plasmoid (step 3). The plasma blob evolves into a pinching of the field lines, eventually forming the X-line, where magnetic field lines can reconnect (step 4). The resulting magnetic stress pulls the field lines towards the planet, restoring the flow to corotation, while the plasmoid is pushed tailward.

Although the giant planets' magnetospheres are predominantly controlled by the Vasyliunas cycle, it is actively debated whether the plasma convection is a combination of two circulation systems, namely the solar wind-driven (Dungey) and the corotation-driven (Vasyliunas) cycles (*Cowley et al.*, 2003, 2004; *Badman and Cowley*, 2007; *Milan et al.*, 2005; *Masters et al.*, 2011; *Chané et al.*, 2013). However, on Earth, the rotation of the planet is traditionally treated as a constant background and the frictional transfer of momentum between the atmosphere and magnetospheric plasma is often neglected beyond the low-latitude plasmasphere (*Matsui et al.*, 2003; *Sandel et al.*, 2003; *Burch et al.*, 2004). In this thesis, and specifically in Papers I and III, we challenge the conventional paradigm according to which Earth's rotation does not affect the magnetosphere.

2.3.4 Convection and currents in the polar ionosphere

High-latitude ionosphere

The ionosphere constitutes the transition region, spanning approximately $100 - 1000$ km altitude, between the fully ionised magnetospheric plasma environment and the neutral atmosphere. As such, the ionosphere comprises a mixture of plasma (ionised gas) and neutral particles ($\sim 99\%$) (*Schunk and Nagy*, 2018; *Baumjohann and Treumann*, 2012). The two main sources of ionisation in the upper atmosphere are solar UV radiation and particle precipitation. At polar latitudes, in the $80 - 200$ km altitude range, the ionisation by precipitation often exceeds the photoionisation. In addition to the dissipation of kinetic energy flux by particle precipitation, the excess energy resulting from the interactions between the solar wind and magnetosphere dissipates in the high-latitude ionosphere through Joule heating (dissipation of electromagnetic flux). Therefore, the polar ionosphere constitutes a key region for the transfer of mass, momentum and energy between the magnetosphere and the upper atmosphere (*Thayer and Semeter*, 2004; *Rae et al.*, 2022).

In this thesis, we are primarily interested in the F-region (> 150 km), the highest and most ionised ionospheric layer, where ideal MHD conditions prevail. At lower altitudes (E-region and below), the collisional coupling between ions and neutrals becomes significant and the ideal MHD approximation is no longer valid.

Ionospheric convection

As magnetic field lines convect within the magnetosphere (see Section 2.3.1), their motion is communicated to the ionosphere (*Cowley*, 2000).

Figure 2.6 shows the ionospheric convection pattern resulting from the reconfigurations of magnetic field lines during southward IMF, as per the Dungey cycle. The opening of field lines at the magnetopause subsolar point and their subsequent transport to the nightside of the magnetosphere by the solar wind flow results in the antisunward motion of their ionospheric footpoints across the polar cap. On the other hand, the sunward convection of closed magnetic field lines around the Earth's flanks results in the ionospheric "return flow" from the nightside to the dayside. The return flow takes place at auroral latitudes, below the OCB. Overall, these dynamics generate a two-cell convection pattern, whose precise geometry is largely determined by the IMF orientation (*Reistad et al.*, 2021).

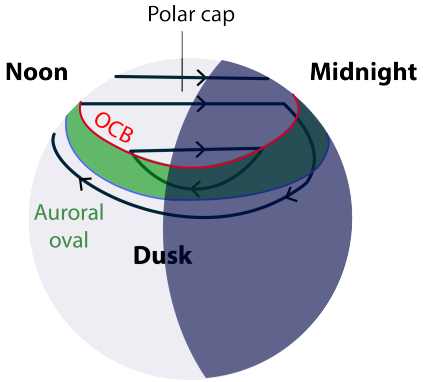

Figure 2.6: Schematic of the horizontal motion (black lines) of the footpoints of magnetic field lines in the ionosphere, following the stages of the Dungey cycle. The illustration primarily shows the dusk side of the two-cell ionospheric convection pattern. The polar cap is delimited by the OCB, depicted by the red line.

Ionospheric current system

In the F-region, the convection of magnetic field lines induces an electric field **E** perpendicular to the magnetic field **B**. Since the electrons are frozen into the plasma and have high mobility along the magnetic field lines, the convection electric field maps down to lower altitudes. In the E-region differential motion between ions and electrons gives rise to the Hall and Pederson currents, which flow horizontally in the ionosphere, given radial magnetic field lines (which is usually a reasonable assumption at high latitudes). The steady-state horizontal ionospheric current system can be described by the ionospheric Ohm's law, here in its height integrated form (with **E** given in the reference frame of the neutrals) (e.g., *Baumjohann and Treumann*, 2012):

$$\mathbf{J} = \Sigma_P \mathbf{E} + \Sigma_H (\hat{\mathbf{b}} \times \mathbf{E}), \tag{2.2}$$

where **J** is the horizontal sheet current density and Σ_H and Σ_P represent the Hall and Pedersen conductances, respectively. $\hat{\mathbf{b}}$ is the unit vector of the magnetic field **B**. The ionospheric Ohm's law is most relevant in the E-region at 110 km altitude (see also Section 4.3.3), which corresponds to where the Hall and Pederson conductivities peak in the ionosphere (*Richmond*, 2007). The ionospheric Ohm's law is derived from the momentum fluid equation, under specific assumptions such as steady-state, charge neutrality, known neutral wind velocity, thermal equilibrium and isotropic pressure.

The Field-Aligned Currents (FACs) (also named Birkeland currents) complete the ionospheric current system by flowing in and out of the ionosphere, parallel to the magnetic field lines. These currents can be described in terms of the divergence of **J**.

Figure 2.7 illustrates the ionospheric high-latitude steady-state current system. The large-scale average FAC flows in two distinctive regions, namely Regions 1 and 2 (*Iijima and Potemra*, 1976a,b, 1978). Region 1 FACs are coincident with the OCB at the poleward edge of the auroral zone, while Region 2 FACs are located near the equatorward edge of the auroral zone (*Burrell et al.*, 2020; *Xiong et al.*, 2014). At dusk, the Region 1 current is upward, and the Region 2 current is downward, while the dawn side exhibits an opposite configuration. Pointing in the same direction as the ionospheric electric field, Pedersen currents flow across the auroral region between downward and upward FACs, as well as from dawn to dusk across the polar cap to close the Region 1 FACs. Anti-parallel to the convection direction, Hall currents flow sunward across the polar cap and anti-sunward on the flanks, forming the eastward and westward auroral electrojets in the dusk and dawn auroral region, respectively. The strength of Hall and Pedersen currents depends on the collisional friction between plasma and neutrals, quantified in terms of ionospheric conductance. The conductance is determined by the level of insolation and the ionisation of the atmosphere (see also Section 2.4.1). As such, the conductance varies diurnally, seasonally and with the 11-year solar cycle, but is generally low in the polar cap and enhanced in the auroral oval as well as sunward of the solar terminator (*Milan et al.*, 2017). This results in strong currents flowing in the auroral region (as indicated by the large arrows).

As depicted in Figure 2.7, the Region 1 and 2 currents are typically oriented in the east-west direction around the pole. The resulting current sheets are associated with

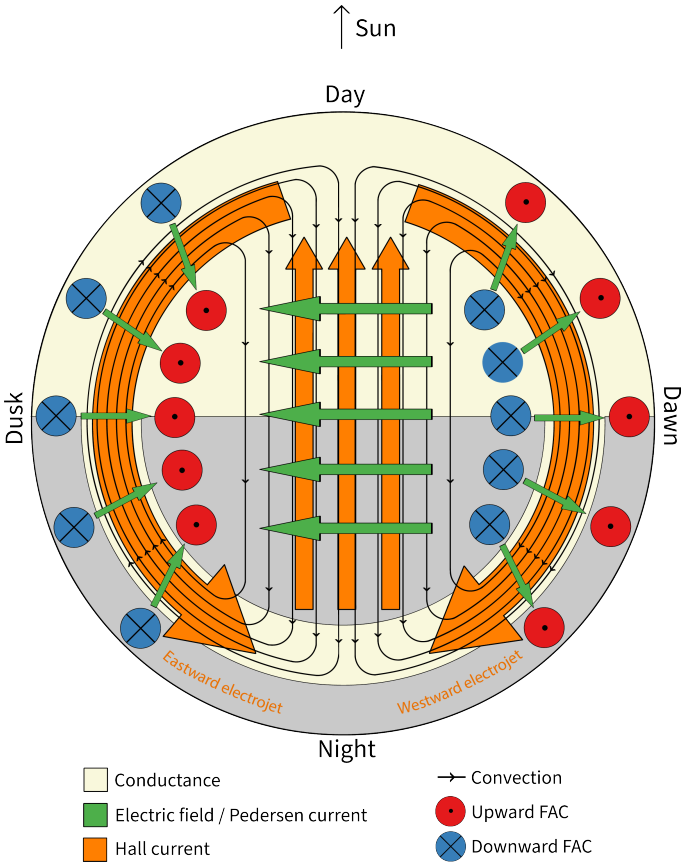

Figure 2.7: Schematic illustration of the steady-state current system in the polar ionosphere during southward IMF. The horizontal Hall and Pederson currents are depicted by the coloured arrows. Upward and downward FACs are shown as blue and red circles, respectively. The black lines and arrows form two cells and indicate the magnetic field line convection pattern. The dayside and auroral regions are coloured in light yellow to highlight enhanced conductance. *Credit: Mîchéllė Mãdelàirę.*

large-scale perturbations in the magnetic field. While FACs constitute quasi-static large-scale structures coupling the magnetosphere and high-latitude ionosphere, Alfvén waves propagate along the magnetic field lines and reflect the smaller-scale dynamic coupling (*Nagatsuma et al.*, 1996), further communicating the motion of the magnetospheric field lines to the ionosphere. Together, they facilitate the exchange of energy, mass and momentum between the magnetosphere and ionosphere (*Lysak and Song*, 2006). Furthermore, FACs and Alfvén waves are associated with the precipitation of electrons along magnetic field lines in the auroral region (see Section 2.4), and Alfvén waves also play a key role in particle acceleration processes (*Hasegawa and Mima*, 1976; *Goertz*, 1984; *Seki et al.*).

2.3.5 Magnetospheric substorms

Dayside reconnection facilitates the conversion of solar wind kinetic energy into magnetic energy. As a result, the magnetotail lobes constitute a region of accumulation of magnetic flux and energy. At some point, the field lines from the two lobes can reconnect and close the open magnetic flux. Among the various magnetospheric mechanisms initiated by the magnetic reconnection process, magnetospheric substorms play a significant role in redistributing energy and plasma within the M-I system, beyond the scope of the Dungey cycle model. Substorms are dynamic transient events occurring in the magnetotail and resulting in a variety of phenomena such as magnetic field disturbances, particle acceleration, and enhanced auroral activity.

A substorm can be decomposed into three phases (*McPherron*, 1970; *Akasofu*, 1964). The loading of open magnetic flux in the magnetotail lobes corresponds to the substorm growth phase. The sudden and explosive release of the energy stored in the lobes following the closing of open flux through nightside reconnection determines the onset of the substorm. This is immediately followed by a brief expansion phase, often associated with the reconfiguration of the stretched field lines in the tail, which become increasingly dipolar, simultaneously accelerating plasma towards Earth. The expansion phase leads to dynamic and intense auroral activity, along with an intensification of ionospheric currents (particularly, the westward auroral electrojet) and enhanced ionospheric convection. In particular, the dipolarisation region in the magnetosphere maps to the "bulge", which corresponds to the region of most intense auroral activity (*Liou et al.*, 2002). Following this peak of activity, the magnetosphere gradually returns to its pre-substorm state during the recovery phase. The rate of nightside reconnection is then diminished, along with weakened auroral activity and currents (*Juusola et al.*, 2011).

As per their role in closing the magnetic flux stored in the lobes, substorm dynamics influence the location of the OCB, which consequently impacts the auroral region morphology at its poleward edge. Additionally, substorm activity induces variations in the location of the low-latitude boundary of the auroral region (*Milan et al.*, 2007; *Laundal et al.*, 2010). During the growth phase, the auroral region's equatorward boundary expands in the midnight sector, where auroral activities are initiated at the substorm's onset. The expansion phase is associated with the contraction of the polar cap, coincident with auroral structures expanding poleward, as well as towards the dusk and dawn sides. Eventually, there is an equatorward and eastward drift of auroral features during the recovery phase, thought to be associated with the large-scale plasma convection (*Akasofu*, 2017). Substorms are the most common type of large-scale auroral disturbances. Moreover, substorm activity correlates with the distribution of electron precipitation (*Gjerloev et al.*, 2008; *Newell et al.*, 2010).

Assuming that substorms can be understood as a result of the combination of a directly driven process (solar wind-magnetosphere dynamo) and an unloading process (explosive nightside reconnection), *Akasofu* (1985) developed an analogy using a pitcher and a tippy bucket. Should the reader be curious, they shall find, in Chapter 7, a semi-approximate Lego model of the M-I coupling relying on *Akasofu* (1985)'s bucket analogy. Our model further highlights the role of the interaction between the IMF and magnetosphere in leading to ionospheric convection and auroral activity.

2.4 The auroral region

As introduced in the preceding sections, the aurora results from the large-scale circulation of plasma and magnetic flux initiated by dayside reconnection between the IMF and magnetosphere. The auroral region commonly refers to the preferred region for the precipitation of particles in the ionosphere, generally associated with FACs and Alfvén waves. Given the mapping between the ionosphere and magnetosphere (Figures 2.1–2.3), ionospheric processes related to auroral activity can, in turn, significantly impact magnetospheric dynamics. For instance, the particles responsible for producing the aurora also enhance ionospheric conductivity, thereby altering interactions between the ionosphere and magnetosphere, including plasma convection. Hence, a thorough understanding of the aurora allows us to gain insights into the dynamics of the magnetosphere and the broader M-I coupling (*Chisham et al.*, 2008).

This section offers a comprehensive overview of the auroral region and its intrinsic phenomena. Note that our focus shifts from the collective behaviour of plasma as a fluid to the individual motion of particles within it (kinetic approach). We begin by exploring the characteristics of the auroral region in terms of particle precipitation in Section 2.4.1. In Section 2.4.2, we provide a summary of how the global dynamics and morphology of the auroral region are ordinarily characterised based on particle precipitation and magnetic field perturbations in the ionosphere.

2.4.1 Auroral particle precipitation

This subsection starts with an examination of the primary magnetospheric source regions for precipitating particles. We then describe the basic plasma physics principles regarding particle precipitation and the specific mechanisms that give rise to the spectacular aurora. We end the subsection with a review of the various types of auroral precipitation.

Source regions for auroral particles

The dayside reconnection between the IMF and the geomagnetic field opens the magnetosphere to the solar wind and provides energy to the local plasma populations. Energetic particles can consequently precipitate into the upper atmosphere. Precipitating particles relate to source regions and processes in the magnetosphere; different regions of the magnetosphere correspond to different plasma populations, with different energies, mapping to specific ionospheric regions (*Newell et al.*, 1996).

Auroral precipitation consists of particles with typical energies ranging from hundreds to thousands of electronvolts (eV) , characterised by intense fluxes. Such particles cause detectable emissions that can be utilised to infer the boundaries of the auroral region and the topology of the magnetosphere (*Sotirelis et al.*, 1998). On the nightside, the main source regions for precipitation are the high-latitude (at the edge of the lobes) and central plasma sheet (*Borovsky et al.*, 1998; *Elphic et al.*, 1999). While both are regions of hot dense plasma confined within closed magnetic field lines, they have different plasma properties (*Baumjohann et al.*, 1988, 1989; *Boakes et al.*, 2014), thus inducing different types of aurora (see dedicated subsection hereafter). The inner boundary of the plasma sheet aligns with very low-energy particles, often coinciding with the plasmapause (*Horwitz et al.*, 1986). Most of the auroral precipitation is observed poleward of this

boundary (*Newell et al.*, 1996). The auroral region poleward boundary is marked by a significant decay of the energy flux over a narrow latitude range. Beyond this limit, the polar cap region is dominated by very low-energy ($\sim$ eV) particle precipitation, referred to as the polar rain (*Newell et al.*, 2004).

Although auroral precipitation predominantly occurs along closed field lines, some low-energy precipitation may occur along open field lines and generate dayside aurora, which can be of various types (*Frey*, 2007; *Frey et al.*, 2019). For example, the cusp aurora is associated with the polar cusp, which is the region in the magnetosphere formed by newly open magnetic field lines (see Figure 2.1), such that the cusp particles reflect their original solar wind kinetic energy, that is approximately $\sim$ 1 keV (*Newell et al.*, 1991a; *Newell and Meng*, 1992; *Newell et al.*, 2004).

Particle motion and precipitation

Charged particles of various origin are trapped within the magnetosphere. One significant source is the solar wind, where the particles can enter the magnetosphere through interactions between the IMF and the magnetosphere. Assuming a dipole magnetic field, individual particles undergo three types of motion: they gyrate around the field line, bounce back and forth between mirror points in either hemisphere and drift either eastwards or westwards, depending on the particle charge, as shown in Figure 2.8 (*Baumjohann and Treumann*, 2012).

A particle's mirror point is defined as the point along the field line where the angle between the particle's velocity vector and the local magnetic field lines (pitch angle α) reaches 90°. When the mirror point is located deep in the atmosphere, the particle's pitch angle lies within the "loss cone" (see Figure 2.8); this results in the particle precipitating and becoming lost to the atmosphere as its kinetic energy is lost due to collisions with the atmospheric neutral constituents (*Baumjohann and Treumann*, 2012). Pitch-angle scattering into the atmospheric loss cone is usually driven by wave-particle interactions in the magnetosphere (*Koskinen and Kilpua*, 2022).

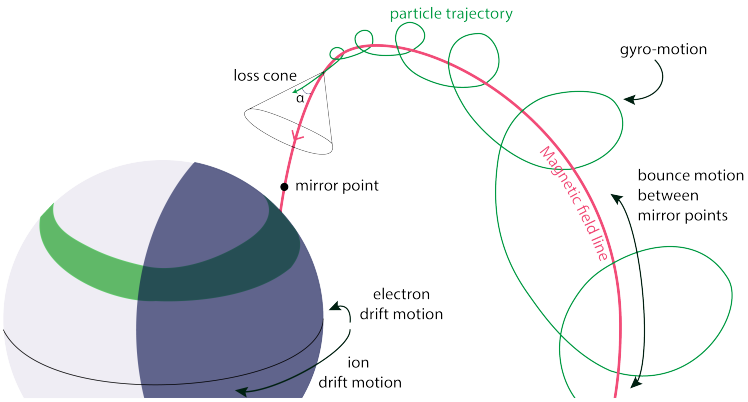

Figure 2.8: Schematic of the trajectory of a particle having its pitch angle (α) within the loss cone. The three types of motion experienced by a particle trapped in a dipole field are shown.

The higher the energy of particles, the further they penetrate the atmosphere. For example, electrons with an energy of 300 keV can reach as far down as about 70 km altitude, while those with an energy of 1 keV are typically stopped at around 150 km altitude (*Baumjohann and Treumann*, 2012). Particles stop their progression down when their kinetic energy is lost to various processes: heating (50%) of the neutral atmosphere (similar to the deposition of electromagnetic flux through Joule heating), as well as ionisation (45%) and excitation of the neutral molecules (5%) (*Thayer and Semeter*, 2004; *Vasyli*, 2010).

The aurora

The population of auroral particles consists primarily of electrons and ions (protons) with energies from a few eV to hundreds of keV originating from the magnetospheric plasma sheet and polar cusp. Auroral particles precipitate into the ionosphere at high latitudes, generally poleward of 70° magnetic latitude.

When atmospheric neutral constituents are excited by such charged particles, they relax to their original energy state by photo-emission, potentially in the visible light spectrum, giving rise to the aurora. The wavelength of the aurora is primarily determined by the excited atom or molecule and the degree to which it is excited. Oxygen atoms, which are predominantly found between 100 and 200 km altitude, primarily emit green light ("auroral green line" at 557.7 nm), yielding the prevalent colour of auroras. Charged particles can also excite higher-altitude (above 300 km) oxygen atoms to a different energy state, usually resulting in red aurora. Weaker shades of red, as well as violet and blue aurora (more scarce), are produced by lower-energy particles colliding with nitrogen molecules, principally found at $100 - 200$ km altitude. Other wavelengths of the aurora, including emission lines in the ultraviolet and infrared ranges, can arise depending on the energy of the precipitating particles, as well as the specific atmospheric conditions. The strongest auroral emissions occur at an altitude of approximately 110 km, coincident with the peak in Hall and Pederson conductances (*Brekke*, 2013; *Baumjohann and Treumann*, 2012).

Imaging the aurora using ground-based optical (all-sky) cameras and space-based imagers (see Figure 2.9) showed that the large-scale aurora exhibits a characteristic shape, often forming an oval at high latitudes around the geomagnetic poles, therefore commonly referred to as the "auroral oval" (*Feldstein*, 2016). Note that the auroral region encompasses more than just the auroral displays perceivable to the naked eye. The aurora can be faint yet exert significant influence on the ionosphere (for example diffuse aurora, see next subsection).

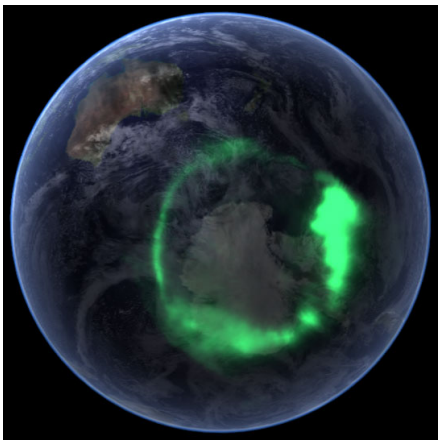

Figure 2.9: Aurora australis (southern lights) captured by the IMAGE satellite. *Image courtesy NASA.*

Different types of auroral precipitation

Aurora can be classified into various types based on the precipitation characteristics, including distinctions in energy spectrum or whether the precipitating particles have undergone specific acceleration processes (which are not detailed here). While ion precipitation also induces auroral phenomena (proton aurora), electron precipitation contributes approximately $80 - 85\%$ of the particle energy input into the ionosphere, making it a crucial factor in the transfer of solar wind energy to the Earth via M-I coupling (*Newell et al.*, 2009; *Dombeck et al.*, 2018). In this subsection, we discuss the different types of electron aurora as categorised by *Newell et al.* (2009).

Discrete aurora When electrons are accelerated along the field lines, leading to their precipitation, they can produce discrete aurora. Depending on the energy spectrum of the precipitating particles, the discrete aurora can be of two types. If the auroral electrons are characterised by high fluxes in only a small range of energies, dominating over the other energies, the precipitation is classified as "monoenergetic". This is the most common type of discrete aurora in terms of deposition of energy flux in the ionosphere (*Newell et al.*, 2009). These monoenergetic events are usually associated with quasi-static electric fields aligned with the magnetic field. On the other hand, "broadband" precipitation refers to high fluxes of electrons occurring over a wide range of energies. Broadband aurora is produced by dispersive Alfvén waves and is often called wave aurora, or even Alfvén aurora (*Ergun et al.*, 1998; *Chaston et al.*, 2003). The broadband aurora does not contribute much to the global precipitation budget during quiet times but becomes important during active conditions. As such, it is the most dynamic auroral type. Broadband aurora is further thought to affect ionospheric heating (*Newell et al.*, 2009). The magnetospheric source region for discrete aurora is typically the high-latitude plasma sheet (*Newell et al.*, 1991a).

Diffuse aurora When electrons precipitate into the ionosphere without prior acceleration, they can generate diffuse aurora. The low-energy electrons (from a few eV to hundreds of eV) that produce this type of aurora indirectly originate from the central plasma sheet (*Newell et al.*, 1991a; *Thorne et al.*, 2010; *Dombeck et al.*, 2018). Diffuse auroral precipitation is often initiated by wave-particle interaction processes scattering the trapped magnetospheric electrons into the loss cone (e.g., *Khazanov and Glocer*, 2020; *Thorne et al.*, 2010). Although generally not visible, electron diffuse aurora represents approximately 60% of the energy flux into the ionosphere. When including the proton aurora, which is of the diffuse type, diffuse aurora contributes up to $\sim 75\%$ of the total precipitating energy flux. Although not as dynamic as discrete aurora, diffuse precipitation also increases rapidly with heightened solar wind driving, bringing the faction of the total precipitating budget to almost 85% (*Newell et al.*, 2009).

A table from *Newell et al.* (2009) is displayed in Figure 2.10, which permits a comprehensive comparison of the hemispheric contribution of each type of aurora, highlighting the predominance of electron diffuse aurora over the three other types of auroral precipitation.

	Low Solar Wind Driving	High Solar Wind Driving	All Conditions	High/Low Ratio
Diffuse ions	2.3 (21%)	4.9 (14%)	3.4 (16%)	2.1
Diffuse electrons	6.8 (63%)	20.2 (57%)	12.6 (61%)	3.0
Monoenergetic	1.1 (10%)	5.8 (15%)	3.3 (16%)	5.3
Broadband	0.6 (6%)	4.8 (13%)	1.5 (6%)	8.0

Figure 2.10: Fractions of the total precipitating energy flux for each type of aurora. *Taken from Newell et al. (2009).*

2.4.2 Dynamics and morphology of the auroral region

The auroral region is traditionally characterised by examining the average auroral energy flux, or by deriving particle precipitation boundaries (*Shue et al.*, 2001; *Newell et al.*, 2009, 2014; *Dombeck et al.*, 2018). While in-situ precipitating particle measurements offer the most direct approach to studying the auroral zone and its dynamics and morphology, observations of magnetic field perturbations of field-aligned current sheets also yield valuable information (e.g., *Wu et al.*, 2017; *Nagatsuma et al.*, 1996; *Xiong et al.*, 2014; *Xiong and Lühr*, 2014). Additionally, several studies have underscored the global role and impact of Alfvén waves in the dynamics of the aurora, notably in accelerating auroral electrons (e.g., *Goertz*, 1984; *Knudsen et al.*, 1998; *Chaston et al.*, 1999, 2003; *Wu et al.*, 2020; *Stasiewicz et al.*, 2000), leading to the recent introduction of the "Alfvénic oval" concept (*Keiling*, 2021), emphasising the importance of FACs and Alfvén waves in shaping the auroral region.

While it exhibits distinct features, the Alfvénic oval shares many similarities with the well-established auroral oval, which commonly refers to particle precipitation. Furthermore, studies using simultaneous magnetic field and particle precipitation measurements have demonstrated the relationship between FAC signatures and precipitating particle energy flux (*Xiong et al.*, 2020), supporting the idea that both types of measurements can be used as proxies for the auroral region.

The auroral region morphology has been investigated in average energy flux studies (e.g., *Newell et al.*, 2009) and discussed in relation to changes in geomagnetic activity (*Feldstein*, 1964; *Feldsten and Starkov*, 1967; *Holzworth and Meng*, 1975). While highly variable, the auroral region shows repeatable patterns, such as asymmetries between dayside and nightside as well as between dawn and dusk (e.g., *Karlsson et al.*, 2017). The dawn-dusk asymmetry has standardly been explained through the scope of kinetic dynamics (e.g. *Ni et al.*, 2016). In this context, the prevalent eastward transport of electrons that leads to the prominent dawn sector in the auroral region is typically interpreted as resulting from a combination of the sunward $\mathbf{E} \times \mathbf{B}$ drift and the gradient drift (see Figure 2.8).

Nevertheless, while average precipitating energy flux models explain the dynamics of the intense discrete aurora, they often fail to accurately describe the weaker diffuse auroral precipitation. This is problematic since diffuse aurora constitutes most of the total auro-

ral energy precipitated into the ionosphere. Moreover, boundary models commonly rely on a circular or elliptical fit of the auroral oval shape, which hinders their ability to capture subtle asymmetries in the spatial distribution of the auroral region. Additionally, these models are typically scaled by a single parameter (such as the geomagnetic Kp index), which falls short of capturing the complexity of auroral dynamics. Consequently, traditional models of the auroral region overlook crucial information, particularly regarding the soft auroral precipitation, and asymmetries within the auroral region.

In this thesis and its associated papers, we develop a novel method of characterisation of the auroral region which does not rely on boundaries nor average precipitating energy flux, notably preserving information about weak precipitation and ideally suited to explore the spatial distribution of the auroral region, specifically in terms of its extent asymmetries. The method relies on the probability of occurrence of the aurora, with aurora as defined from both electron precipitation (Paper I) and magnetic field fluctuation measurements (Paper II). The method is described in detail in Section 4.2. Furthermore, we argue that the dawn-dusk asymmetry observed in our auroral occurrence probability can be partly explained from a fluid perspective, in addition to the typical kinetic framework (see next section).

2.5 Fluid versus kinetic descriptions of the plasma

Geospace dynamics can be understood from both fluid and kinetic perspectives, each offering unique insights. The Dungey cycle and the ECPC paradigm describe the combined action of subsolar and magnetotail reconnections and the consecutive circulation of magnetic flux and plasma in the magnetosphere through a fluid point of view. This entails an emphasis on the bulk motion of plasma rather than on the behaviour of individual particles within the plasma. On the other hand, we saw in Section 2.4 that a kinetic description becomes essential to describe the mechanisms leading to the aurora. In this section, we address the benefits and limitations of both types of perspectives within the context of this thesis.

Kinetic perspective

The behaviour of individual particles might significantly deviate from the bulk plasma motion, particularly in high-energy particle populations. A conventional MHD description is no longer appropriate when the distribution of particle velocities stops following a Maxwellian distribution; necessitating a kinetic approach to accurately model the particle dynamics. The kinetic theory treats the plasma as a collection of particles and accounts for the simultaneous gyration, bouncing and drift motions experienced by particles trapped in a dipole magnetic field (*Baumjohann and Treumann*, 2012) (see Section 2.4.1 and Figure 2.8). The kinetic approach also distinguishes between electron and ion behaviour. This is particularly relevant in understanding the auroral region morphology, as the differential drift motion between electrons and ions is responsible for the dawn-dusk asymmetric pattern in the auroral electron precipitation (see Section 2.4.2)

Why is the fluid description valuable?

While kinetic theory provides a detailed understanding of plasma dynamics at the particle level, it is a complex approach which can present challenges in both computation and interpretation. The kinetic description involves solving a set of non-linear equations to determine the distribution function, which represents the probability of finding particles within an abstract mathematical coordinate system (the phase space). By deriving physical quantities related to the bulk plasma properties (density, velocity, pressure, etc.) from the velocity moments of the particles' distribution function, fluid models offer a simplified yet insightful view of the plasma behaviour. MHD specifically gives a "human-readable" description of the collective behaviour of charged particles and how they induce variations in the surrounding electromagnetic field, which the kinetic theory fails to do.

In summary, both perspectives complement each other. While kinetic descriptions are indispensable for understanding fine-scale processes and high-energy particle behaviour within the magnetosphere, the fluid perspective is valuable for comprehending large-scale plasma dynamics both qualitatively and quantitatively.

In this thesis, the emphasis is on the large-scale qualitative description of the M-I coupling. Therefore, our findings, interpretations and hypotheses largely stem from a fluid depiction of the plasma and frozen-in magnetic field lines in the M-I system. In particular, our conceptual reflections concerning the influence of Earth's rotation on the M-I coupling are derived from the fluid perspective. The naive view is that the particles from the neutral atmosphere – presumed to be synchronised with the Earth's rotation – transfer some of their momentum to the plasma in the upper atmosphere through frictional forces. As such, Earth's rotation contributes to dragging the ionospheric plasma at high altitudes. Given the topological mapping between the ionosphere and magnetosphere, the momentum and associated bulk motion in the ionosphere are further communicated to the magnetosphere, illustrating that the M-I coupling goes both ways (e.g., *Dai et al.*, 2024; *Chisham et al.*, 2008).

The perspective wherein Earth's rotation plays a role in moving the large-scale fluid in the magnetosphere is commonly accepted in the plasmasphere, which is known to corotate with Earth to some extent, and has also been largely described on planets such as Jupiter and Saturn (see Section 2.3.3). Moreover, it has been shown that the corotation-driven ionospheric and magnetospheric flows and currents shape the aurora on the giant planets (*Cowley et al.*, 2004; *Cowley and Bunce*, 2003; *Cowley et al.*, 2003; *Zhang et al.*, 2021). In this thesis, we expand upon this conceptual framework to encompass Earth's outer magnetosphere. When treated as a fluid sensitive to the motion of the atmosphere, how does the magnetospheric plasma shape the auroral region?

3 Data

This chapter offers an overview of the various datasets used in this thesis. Sections 3.1 and 3.2 introduce particle precipitation and magnetic field data, respectively, sourced from ionospheric observations. Section 3.3 outlines plasma convection data obtained from the magnetosphere. Section 3.4 presents the IMF measurements and geomagnetic indices that are integrated with our main datasets. The particle precipitation and magnetic field data are complemented by a list of substorms briefly detailed in Section 3.5. We employed the Python library Vaex (*Breddels, Maarten A. and Veljanoski, Jovan*, 2018) to efficiently handle and analyse the large particle precipitation and magnetic field datasets since they respectively contain approximately 10^9 and 10^8 data points.

3.1 Particle precipitation – DMSP/SSJ

The auroral particle precipitation measurements from the US Defense Meteorological Satellite Program (DMSP) constitute one subset of the three main datasets used in this work. They are the basis of our work in Paper I.

DMSP consists of a series of polar, low Earth ($\sim$ 850 km altitude), Sun-synchronous, orbiting satellites operated by the US Air Force Space Command and the National Oceanic and Atmospheric Administration. Typically used to deliver environmental information related to weather and climate, DMSP is also equipped to detect particles from the near-Earth space environment that precipitate into the ionosphere.

Precipitating particles are magnetospheric particles with pitch angles within the loss cone, resulting in their loss into the atmosphere (see Section 2.4.1). The Special Sensor J (SSJ) consists of four electrostatic analyzers (two low-energy and two high-energy) that record precipitating particles as they flow past the spacecraft towards the Earth, providing a complete energy spectrum of electron and ion fluxes ranging from 30 eV to 30 keV, captured at a 1-second cadence. SSJ versions 4 and 5 are particularly well-suited to monitor particles that cause the aurora due to the sensors' optimal viewing geometry, making them sensitive to particles within the loss cone at auroral latitudes. Additionally, SSJ5 has the advantage of a wider field of view compared to SSJ4 (*Redmon et al.*, 2017).

The DMSP/SSJ data has been widely used and proven valuable for investigating the auroral region and its boundaries (e.g., *Hardy et al.*, 1985; *Newell et al.*, 1996, 2009; *Kilcommons et al.*, 2017; *Burrell et al.*, 2020). In Paper I, we use measurements from the 10 energy channels of the high-energy electron detector, covering auroral electron energies from approximately 1 to 30 keV. Using *Redmon et al.* (2017)'s new DMSP database of precipitating electrons and ions, our dataset assembles measurements from SSJ4 on board DMSP F12, F13, F15, F16, and from SSJ5 on board DMSP F18, covering non-continuous data from 2000 to 2016. Figure 3.1 displays the latitude versus local time coverage resulting from our selection of satellites, presented in geographic and magnetic coordinates for both hemispheres. All orbits are dawn-dusk oriented and form thin lines in geographic latitude and local time as DMSP spacecraft are Sun-synchronous. However,

in magnetic coordinates, the satellites' orbital planes span a broader area due to the offset between the magnetic and geographic poles. This offset is larger in the south, leading to better coverage for the Southern Hemisphere compared to the Northern Hemisphere. In Section 4.1, we discuss how the Sun-synchronous orbits can constitute a source of bias in the detection of the auroral region boundaries.

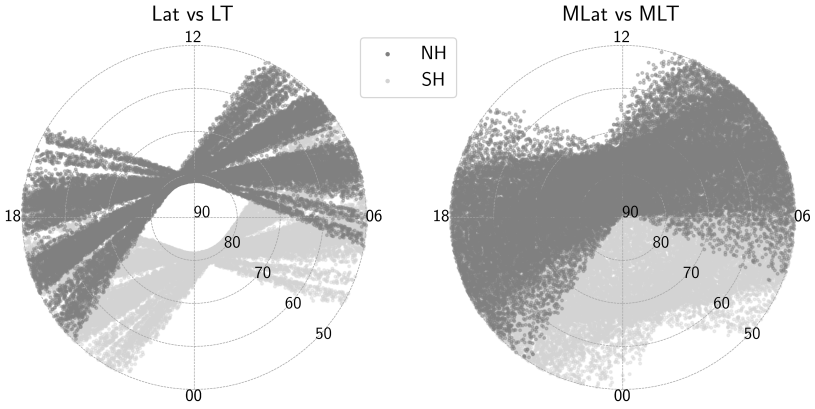

Figure 3.1: Combined coverage obtained from DMSP F12, F13, F15, F16 and F18's orbits, shown in the geographic (left) and magnetic (right) latitude vs local time planes. Only 0.1% of the data is displayed.

In the end, we gather a substantial electron energy flux dataset covering approximately 20 years at a resolution of 1 second (about a billion measurements). This provides us with adequate material for conducting a robust statistical analysis of the auroral region, with a comprehensive coverage of all MLT sectors between 60° and 90° MLat when both hemispheres are combined. However, coverage of the post-noon and post-midnight regions below 70° is poor, prompting a cautious interpretation of our results when evaluating the global morphology of the auroral region.

3.2 Magnetic field in space – Swarm/VFM

The magnetic field perturbation measurements from the Swarm satellites form the second main dataset used in this thesis (Paper II).

Swarm is a European Space Agency (ESA) mission consisting of a near-polar low-orbiting constellation of three identical satellites; Swarm A and C orbit side-by-side at $\sim$ 450 km altitude while Swarm B flies about 50 km higher, thereby sampling different local times than Swarm A and C. The mission's central objective is to study the Earth's magnetic field and electric currents. Swarm has demonstrated remarkable capabilities in providing highly accurate measurements of magnetic signals that stem from various sources within and around the planet, including Earth's ionosphere and magnetosphere (*Friis-Christensen et al.*, 2008).

Particularly relevant for this thesis, the Vector Field Magnetometer (VFM) measures the strength and direction of the ambient magnetic field. Mounted on an ultra-stable

structure (optical bench) located halfway along the satellite's boom, the VFM sensor is coupled with star trackers, which provide extremely accurate attitude measurements, ensuring the precise determination of the magnetic field vector with a resolution of up to 50 Hz. The combination of a multi-satellite configuration, sophisticated instrument design, and optimised data calibration enables unique accuracy and precision. Figure 3.2 shows an artist's representation of the Swarm constellation, highlighting the characteristic boom.

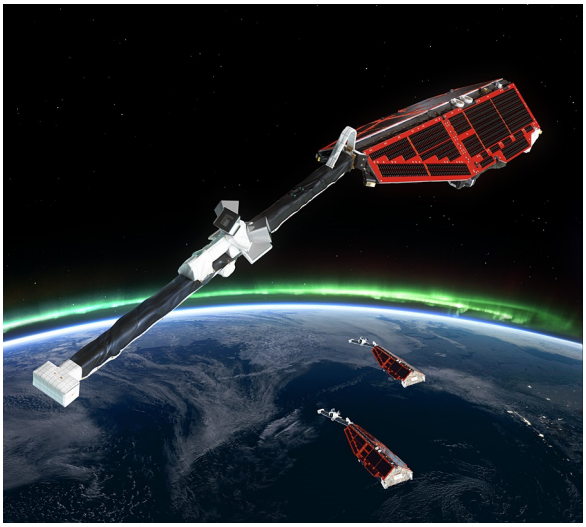

Figure 3.2: Artist's illustration of the constellation of Swarm satellites, notably depicting the distinctive instrument setup.

Swarm/VFM has been featured in several studies related to the electric current systems of the auroral zone, which are often focused on field-aligned currents (*Wu et al.*, 2020; *Ritter et al.*, 2013; *Lühr et al.*, 2019). In Paper II, we use the Level 1B high-resolution magnetic field vector data from Swarm A and B between 2014 and 2021. The original data product is downsampled to 10 Hz by selecting every fifth measurement. Using the International Geomagnetic Reference Field (IGRF) model of the Earth's main magnetic field, we extract the magnetic field perturbation vector from the total magnetic field measured by Swarm: $\mathbf{\Delta B} = \mathbf{B}_{\text{meas}} - \mathbf{B}_{\text{IGRF}}$. We further isolate the east-west component of $\mathbf{\Delta B}$ in magnetic Apex coordinates (*Richmond*, 1995), such that time series of $\Delta \text{B}_{\text{EW}}$ specifically inform us about the large-scale fluctuations in the auroral region (*Hatch et al.*, 2020).

This dataset ultimately comprises approximately 100 million measurements of east-west magnetic field fluctuations, identified from nearly $2 \cdot 10^5$ polar region crossings in both hemispheres. Unlike the DMSP spacecraft, the Swarm constellation's orbit ensures coverage of all local times within five years (*Lühr et al.*, 2019). Thus, our dataset provides complete coverage of the auroral region.

3.3 Magnetospheric convection – Cluster/EDI

The magnetospheric convection measurements from the Cluster satellites constitute the third main dataset used in this thesis (Paper III).

Cluster is a 4-spacecraft ESA mission designed to provide insight into the Earth's magnetic environment and its interaction with the solar wind. The four identical satellites (C1–C4) fly in tetrahedral formation between roughly 20.000 and 120.000 km above the Earth. They operate in an elliptical polar orbit, with their perigee and apogee at approximately 4 and 19 R_E geocentric distance, respectively. This orbit allows Cluster to sample the magnetotail and the cusp regions of the magnetosphere where the plasma structures can be explored in three dimensions, enabled by the simultaneous four-point measurements. Of interest for this study, the Electron Drift Instrument (EDI) , onboard satellites C1 to C3, monitors the plasma convection velocity.

The electron-drift technique determines the strength of the ambient electric and magnetic fields by measuring the drift velocity of artificially injected electrons after one gyration orbit around the spacecraft (*Paschmann et al.*, 2001; *Quinn et al.*, 2001). EDI is particularly well suited for regions of low plasma density and stable magnetic fields such as the lobe regions (low plasma parameter β). In such domains, the drift velocity is proportional to the convective electric field. EDI thus offers a high-quality set of high-latitude convection measurements (*Förster and Haaland*, 2015). In contrast, plasma instruments usually suffer from poor accuracy due to low count rates and wake effects caused by photo emissions in these regions (e.g., *Grard et al.*, 1983).

Cluster/EDI has been employed in several studies on plasma convection in the magnetosphere (*Paschmann et al.*, 2021; *Haaland et al.*, 2008; *Matsui et al.*, 2004; *Förster et al.*, 2007). In Paper III, we use EDI convection measurements that have been mapped from the Cluster orbit into the polar ionosphere at 300 km altitude, using the T2001 magnetic field model (*Tsyganenko*, 2002a,b) and assuming equipotential conditions along the geomagnetic field lines. The mapping procedure is described in detail in *Haaland et al.* (2007). Such mapping enables the combination of magnetospheric measurements along a given field line, facilitating a robust statistical analysis and allowing the comparison between magnetospheric convection and ionospheric observations. Uncertainties related to this mapping are discussed in Section 4.4

Figure 3.3 depicts the distribution of our Cluster/EDI dataset in the GSM XZ plane, with Earth centred at (0,0). It can be seen that the central plasma sheet (small Z values) is mostly not sampled, such that the majority of our dataset originates from the high-latitude plasma sheet and the lobes. The measurements are largely taken at radial geocentric distances between 5 and 8 R_E.

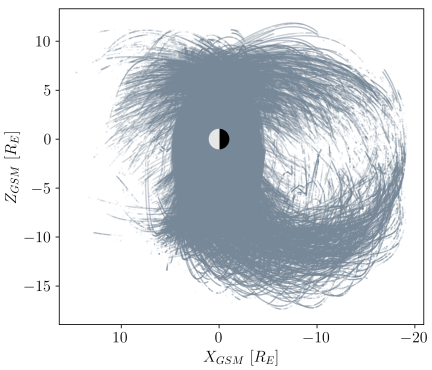

Figure 3.3: Distribution of Cluster/EDI measurements in the magnetosphere.

Our final dataset comprises about 10^6 1-min resolution Cluster/EDI measurements spanning from 2001 to 2018, mapped into the ionosphere and covering all magnetic latitudes between 50° and 90° in both hemispheres.

3.4 Solar wind properties and geomagnetic activity indices – OMNI

As we aim to investigate the response of precipitating electrons (Paper I), magnetic field fluctuations (Paper II), and convection measurements (Paper III) to various geomagnetic conditions, all three datasets (Sections 3.1–3.3) are combined with measurements of the IMF and geomagnetic indices. We use the OMNIWeb database (*Papitashvili*, 2005), which aggregates data from multiple spacecraft located in geocentric orbit or orbiting around L1 (Lagrange point), along with geomagnetic activity indices obtained from ground-based magnetometers. Particularly, we make use of the 1-min resolution IMF B_y and B_z components and the Auroral Lower (AL) and Symmetric Horizontal disturbance (SYM-H) geomagnetic indices between 2000 and 2014.

The IMF parameters represent near-Earth estimates of solar wind properties, as the original upstream observations have been time-shifted to the Earth's bow shock nose (*King and Papitashvili*, 2005). The AL index corresponds to the minimum perturbation in the horizontal (H) component of the magnetic field, measured by a selection of twelve magnetometer stations located along the auroral zone in the Northern Hemisphere. The AL index is primarily sensitive to the westward electrojet. At lower latitudes, ground magnetometers can derive the SYM-H index, which is a higher resolution version of the Disturbance Storm Time (Dst) index (1 min versus 1 hour). Both are designed to measure the equatorial magnetic field variations during storms (*Wanliss and Showalter*, 2006) and are primarily sensitive to the ring current. Therefore, the AL and SYM-H indices serve as proxies for geomagnetic activity levels.

In Papers I and II, the OMNI data is temporally aligned with our 1-second resolution datasets by associating each DMSP/SSJ and Swarm/VFM measurement with the OMNI data point from the nearest preceding minute.

3.5 Substorm epochs

In Papers I and II, the particle precipitation and magnetic field datasets are also organised and studied with respect to substorm phases. We use the list of substorm onsets identified by *Ohtani and Gjerloev* (2020), designed to provide a catalogue of isolated clear events determined with a high degree of confidence. Their identification technique relies on the SML index, which is the SuperMAG equivalent to the AL index (see previous section). The SML index is similarly sensitive to changes in the westward electrojet but, in contrast to the AL index, it incorporates data from all available magnetometers at the time of the index, covering magnetic latitudes between 40° and 80°, and focuses on the northward component (local magnetic north) (*Gjerloev*, 2012).

The list spans the time ranges covered by the DMSP/SSJ and Swarm/VFM datasets, allowing for large superposed epoch analyses including $\sim$ 12000 and 3500 isolated substorm onsets, respectively.

4 Methods

This chapter presents an overview of the diverse methodologies used in this thesis for characterising the morphology of the auroral region, extracting insights from ionospheric observations into the dynamics of the magnetosphere, and evaluating the role of Earth's rotation on magnetospheric convection patterns. Section 4.1 briefly describes a method for describing the shape of the auroral region that, while ultimately not utilised in our analysis, had a role in shaping our research trajectory and refining our methodology. Section 4.2 provides condensed summaries of the methodologies implemented for determining the "auroral occurrence probability", as extensive explanations are available in Papers I and II. In contrast, we present more detailed discussions regarding the quantification of corotation in magnetospheric convection data and the potential implications for ionospheric electrodynamics in Section 4.3, as they are less thoroughly described in Paper III due to format constraints. Last, we address the uncertainties associated with the various data and techniques used throughout this thesis in Section 4.4.

4.1 Auroral boundary detection based on Sun-synchronous satellites: The local time bias issue

In the project's early stages, we considered replicating *Kilcommons et al.* (2017)'s algorithm to identify the auroral oval boundaries based on DMSP/SSJ data and extending the existing dataset. We intended to adapt this algorithm to POES and MetOp/TED and MEPED data, thereby assembling a comprehensive database of auroral boundaries derived from particle precipitation measurements from different satellites. Our objective was to conduct a statistical analysis of these boundaries to elucidate the large-scale evolution of the auroral region depending on solar wind and magnetospheric drivers.

While auroral boundary datasets based on particle precipitation have provided valuable insights in many previous studies analysing the shape of the auroral oval (e.g., *Newell et al.*, 1991b, 1996; *Kauristie et al.*, 1999; *Redmon et al.*, 2010; *Niu et al.*, 2015; *Kilcommons et al.*, 2017), we are concerned that in situ measurements collected by Sun-synchronous satellites such as DMSP or POES/MetOp might produce a statistically biased estimate of the auroral oval boundaries. In fact, such satellites consistently pass over the same latitude at the same local time during each orbit, which results in a distribution of measurements that is biased towards specific local times. A detailed example of how this can lead to misestimation of the boundary position by several degrees is given in Paper I. This type of error can have a significant impact when determining the extent of the auroral region. Expanding the data coverage by employing a variety of satellites with diverse orbits ensures a more accurate estimation of the auroral boundaries. However, despite the extensive global coverage provided by the DMSP fleet (see Section 3.1), the issue of local time bias persists as long as not all MLT sectors at auroral latitudes exhibit a high density of measurements.

These experimental findings led us to adopt a different approach early in the study,

which proved to be more effective in achieving our research objectives.

4.2 Auroral occurrence probability (AOP)

4.2.1 Concept

The auroral occurrence probability (AOP) offers an alternative approach to address the problem of local time bias inherent in statistical analyses derived from in situ Sun-synchronous satellite measurements. The concept of auroral occurrence probability is based on the first steps of *Kilcommons et al.* (2017)'s algorithm for auroral boundary identification, that is, the determination of the portions of the satellite orbit crossing the aurora. Using the DMSP/SSJ dataset in the context of this thesis, "aurora" refers specifically to auroral electron precipitation. In this context, an auroral observation is recorded whenever an electron energy flux measurement surpasses a specified threshold indicative of auroral precipitation. The determination of whether a portion of the orbit is identified as aurora depends solely on this threshold and is completely independent of the number of measurements in the corresponding MLat–MLT sector, thus excluding a potential local time bias. Additionally, statistics based on a dataset of auroral occurrence probabilities have the advantage of making use of all available observations, including observations of no or low precipitation. In contrast, such observations are discarded when detecting auroral region boundaries, which introduces biases in the data distribution.

The AOP is thereby ideally suited for statistically investigating the morphology of the auroral region. Note the distinction between "auroral region" and "auroral oval". On the one hand, the auroral oval commonly refers to the high-latitude region where particle precipitation results in visible aurora. On the other hand, the AOP is a broader concept that serves the investigation of the auroral region in general and doesn't presume the type of electron aurora (discrete versus diffuse). In fact, in Paper I, we point to the predominance of diffuse aurora in our AOP dataset, which is typically orders of magnitude below the 1 $\mathrm{mW/m^2}$ auroral brightness that *Keiling et al.* (2003) define as visible aurora. Therefore, the AOP may not align precisely with the region enclosed by the auroral oval boundaries. In Paper I, we did not explicitly address this difference, as the terms "auroral electron precipitation" and "auroral oval" were used interchangeably. However, in this chapter, we are more meticulous and precise in our terminology. Furthermore, while we have introduced the concept of AOP as relating to DMSP/SSJ measurements, i.e., auroral electron precipitation (see also Section 4.2.2), we will see that it can be extended beyond precipitation data, notably using satellite-based magnetic field measurements in the auroral region (see Section 4.2.3).

4.2.2 Auroral electron precipitation occurrence probability (POP)

The auroral electron precipitation occurrence probability (POP) is established through a binary time series indicating whether a specific energy flux spectrum of loss-cone electrons, as measured by the DMSP/SSJ instrument, corresponds to an observation of auroral electron precipitation. Using the integrated electron energy flux in the range $1.392 - 30$ keV (*Hardy et al.*, 1985), each entry in our DMSP/SSJ dataset is assessed against an electron energy flux threshold of $2 \cdot 10^9$ $\mathrm{eV/cm^2/s/sr}$, identifying it as either auroral or non-auroral precipitation based on whether it exceeds the threshold.

The probability of occurrence of auroral electron precipitation is calculated across various MLat–MLT sectors covering the polar regions by dividing all positive observations (measurement identified as auroral electron precipitation) by the total number of measurements in each sector. An example of POP distribution can be found in Figure 3 of Paper I.

We use the resulting POP distributions associated with various external conditions, such as geomagnetic activity and substorm phases, to investigate the global shape of the auroral electron precipitation region and its latitudinal extent depending on MLT. We emphasise that the POP distributions constitute a major outcome for this thesis as they not only comprise the base for all results and discussions presented in Paper I but additionally contribute to Paper II's discussion and lead to the conceptual framework of Paper III.

Note that in this thesis, we employ the term POP to denote the precipitation occurrence probability, whereas in Paper I, we refer to the same quantity as AOP for auroral occurrence probability. Although technically accurate, we later recognised the value of using a more specific term since the auroral electron precipitation occurrence probability is only one aspect of the broader concept of AOP. In fact, the AOP is of a different nature in Paper II as it relies on magnetic field perturbations (see next section). In this thesis, auroral occurrence probability designates the general concept encompassing both auroral electron precipitation occurrence probability and auroral disturbed magnetic field occurrence probability.

4.2.3 Disturbed magnetic field occurrence probability (dBOP)

The disturbed magnetic field occurrence probability (dBOP) relies on a similar concept as the POP but uses magnetic field measurements from the VFM instrument on the Swarm satellites. The data processing leading to the calculation of dBOP also involves a few additional steps compared to the POP. Using the perturbation magnetic field in the magnetic east-west direction, the identification as "disturbed" magnetic field depends on a wave power threshold, necessitating the estimation of ΔB_{EW} spectrograms and integrated power spectral density in different frequency bands. The frequency ranges are as follows: $0.05 - 0.5$, $0.1 - 1$ and $2.5 - 5$ Hz. The spectral power estimate for each entry of our Swarm/VFM dataset is deemed disturbed magnetic field when exceeding the 75th percentile in each frequency band. The probability of occurrence of a disturbed magnetic field is eventually calculated in the same MLat–MLT sectors as the POP. The complete methodology for deriving MLat–MLT dBOP distributions is detailed in Paper II, and an overview is provided in Figure 4.1. Examples of dBOP distributions at low and high frequency can be found in Figures 4 and 5, in Paper II.

The resulting dBOP distributions are used to examine the auroral region morphology and its connection to magnetospheric dynamics under varying external conditions. It's important to highlight that while we posit a direct connection between POP and aurora, the corresponding relationship between dBOP and aurora is less evident. However, by definition, the dBOP constitutes a measure of the magnetic field conditions at high latitudes, such that its analysis contributes to characterising the auroral region.

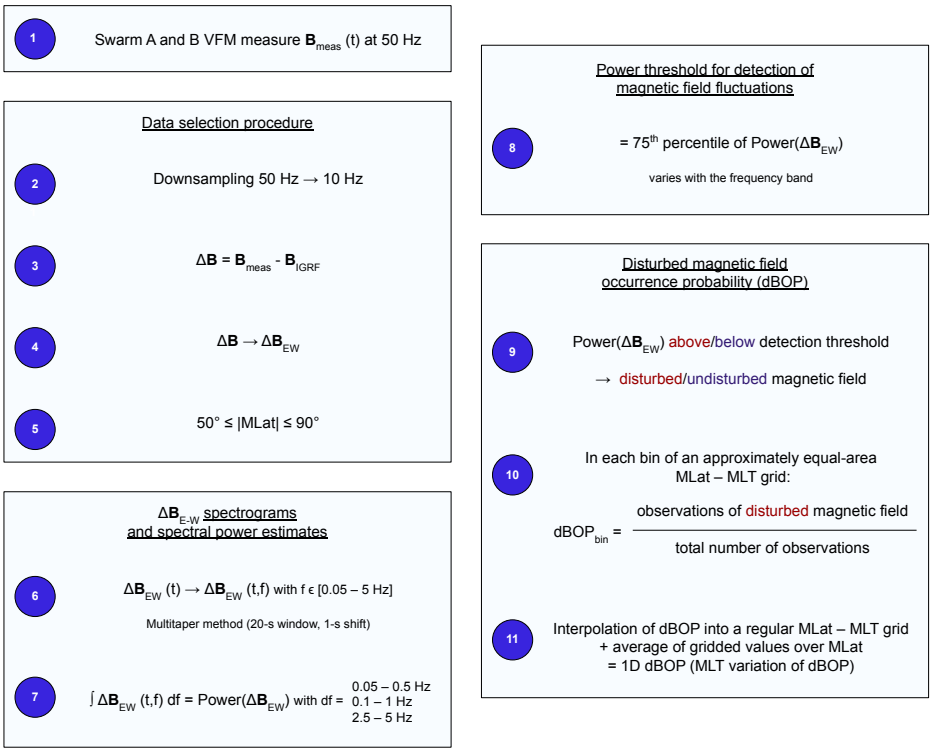

Figure 4.1: Summary of the methodology used to derive the dBOP and 1D dBOP. *Taken from Paper II.*

4.2.4 MLT variation of POP and dBOP

The above-mentioned probabilities are computed for each MLat–MLT bin within an approximately equal area grid, provided that they are covered (> 200 measurements) by DMSP and Swarm orbits. The grid consists of rings with a width of 1° MLat divided into a varying number of cells (varying MLT resolution), with 2 cells in the most poleward circle ($89° - 90°$) and 68 cells in the most equatorward circle ($50° - 51°$).

MLT profiles of POP and dBOP are additionally derived by interpolating the probabilities to a regular MLat–MLT grid (0.5° MLat and a constant 8 min MLT resolution) and averaging the gridded values over the entire range of latitudes ($50° \leq |\text{MLat}| \leq 90°$). The resulting 1D POP and 1D dBOP are not considered probabilities but can be used to assess the variation of POP and dBOP as a function of MLT. These 1D distributions provide a simpler means of visualising potential spatial asymmetries in the auroral electron precipitation and disturbed magnetic field than the complete MLat–MLT distributions. An example of such profiles is given in Figures 4 and 6 of Papers I and II, respectively.

4.3 Corotation in the magnetosphere

In Paper III, we examine the synchronisation between the magnetospheric plasma and Earth's rotation. Sections 4.3.1 and 4.3.2 outline our methods for visualising and quantifying corotation in the magnetospheric plasma flow measured by Cluster/EDI. Section 4.3.3 details the assumptions and methodology used to further interpret our results.

We emphasise that the Cluster/EDI measurements are projected along the magnetic field lines to the ionosphere at 300 km altitude, as detailed in Section 3.3. Therefore, while the MLat–MLT maps and MLat profiles derived in the following section offer a means to visualise convection velocities at ionospheric altitudes, they still characterise the magnetospheric plasma flow.

4.3.1 Convection velocity maps

We bin the northward v_n and eastward v_e components of the mapped EDI convection velocity data into an approximately equal area MLat–MLT grid identical to the one described in Section 4.2.4. The median values of v_n and v_e are used to represent the convection velocity vector within each cell of the grid, provided that it contains at least three measurements. We obtain statistical MLat–MLT distributions of high-latitude magnetospheric convection velocities similar to those presented in *Haaland et al.* (2007), from an extended EDI dataset. Paper III presents such distributions in Figure 1.

4.3.2 Corotation MLat profiles

Estimating the theoretical corotation flow

We define the theoretical corotation flow as a flow of plasma perfectly synchronised with Earth's rotation. In this context, the plasma corotation velocity is determined by Earth's rotation rate, $\omega_0 \approx 2\pi/24$ rad/h, the radius at which the Cluster/EDI measurements are mapped, $R = R_E + 300$ km, and the latitude λ. Following *Laundal et al.* (2022a), the corotation velocity can be expressed as:

$$\mathbf{v_c} = \omega_0 R \cos(\lambda) \hat{\mathbf{e}}. \tag{4.1}$$

This theoretical corotation velocity can be compared with the measured average plasma eastward velocity obtained from Cluster/EDI convection data (as discussed in the following subsection). Alternatively, the integrated vorticity of the theoretical and observed corotation flow can be compared. The calculation of the integrated vorticity, or curl, over a surface A can be simplified using Stokes' theorem; The integration of the vorticity of $\mathbf{v}_c$ over A is equivalent to the line integral of v_c around the boundary curve l of A:

$$\int_A \left(\nabla \times \mathbf{v_c}\right) \cdot \hat{\mathbf{r}}\, dA = \oint_l \mathbf{v_c} \cdot\, d\mathbf{l}. \tag{4.2}$$

For a surface enclosed by a circle of constant latitude λ of length $2\pi R\cos(\lambda)$, the inte-

grated curl of the theoretical flow field is thus:

$$\int_A \left(\nabla \times \mathbf{v_c}\right) \cdot \hat{\mathbf{r}}\, dA = v_c(\lambda) 2\pi R \cos(\lambda). \tag{4.3}$$

The comparison of the theoretical integrated vorticity with its observational counterpart is detailed in the next subsection.

Measuring the observed corotation flow

The observed corotation flow is derived from the binned Cluster/EDI measurements (see Section 4.3.1). Using Stokes' theorem, the integrated vorticity of the observed corotation flow over the surface A enclosed by a circle of latitude λ can be calculated as:

$$\int_A \left(\nabla \times \mathbf{v_e}\right) \cdot \hat{\mathbf{r}}\, dA = \oint_l \mathbf{v_e} \cdot\, d\mathbf{l} = \sum_i v_{e_i} \Delta\phi(\lambda) R \cos(\lambda), \tag{4.4}$$

with v_{e_i} representing the median value of the eastward velocity in the ith bin on a ring of latitude λ, and $\Delta\phi$ the MLT resolution of these bins at λ (in radians). The observed average corotation velocity is obtained by dividing Equation 4.4 by $2\pi R\cos(\lambda)$:

$$\overline{v_e} = \frac{1}{2\pi} \sum_i v_{e_i} \Delta\phi(\lambda) \tag{4.5}$$

In Paper III, we compare the theoretical and observed corotation flows using the two types of statistics derived in this section;

- The corotation flow velocity along circles of constant latitude: v_c versus $\overline{v_e}$ (Equation 4.1 vs Equation 4.5).
- The integrated flow vorticity for surfaces enclosed by circles of constant latitude: $v_c(\lambda)2\pi R\cos(\lambda)$ versus $\overline{v_e}(\lambda)2\pi R\cos(\lambda)$ (Equation 4.3 vs Equation 4.4).

The comparison is then based on the associated corotation profiles as a function of latitude. Since both types of statistics are proportional by a factor of $2\pi R\cos(\lambda)$, they provide the same information but offer different perspectives. Specifically, in evaluating the presence of an eastward component in the convection flow at different latitudes, we prefer the integrated vorticity due to its smoother observation profile. On the other hand, the velocity profiles are used to quantify the discrepancy between Earth's rotation and the observed eastward velocity in the convection flow. The "corotation lag", obtained by subtracting $\overline{v_e}$ from the theoretical v_c, is further used to estimate potential implications in the ionosphere electrodynamics (see Section 4.3.3). MLat profiles of the corotation velocity, integrated vorticity, and corotation lag are presented in Figure 1 of Paper III.

Varying rotation rate in magnetic coordinates

If the motion of the atmosphere solely determined the near-Earth plasma transport and if the atmosphere remained stationary relative to the ground, the magnetic field and the

frozen-in plasma would complete one rotation around the magnetic poles per day. However, due to the Earth's dipole magnetic field not aligning with the rotation axis, the effective rotation rate, seen in magnetic coordinates, varies with universal time and season (*Laundal and Richmond*, 2017). Given that our data has been collected at different times throughout the day and year, we anticipated that the observed average eastward velocity (previous subsection) might be impacted by deviations from the nominal rotation rate $\omega_0 = 2\pi/24$ rad/h.

The magnetic corotation rate can be calculated for every Cluster/EDI measurement as:

$$\omega(t) = \frac{\Delta \mathrm{MLT}(t)}{\Delta t}\omega_0 \tag{4.6}$$

where MLT is defined by Equation 93 in *Laundal and Richmond* (2017).

Figure 4.2 shows the evolution of $\frac{\omega(t)}{\omega_0}$ with the time of the day and the time of the year. The range of variation of the magnetic corotation rate relative to ω_0 is about 14%. $\omega(t) = \omega_0$ when the "change in MLT per hour" is 1.

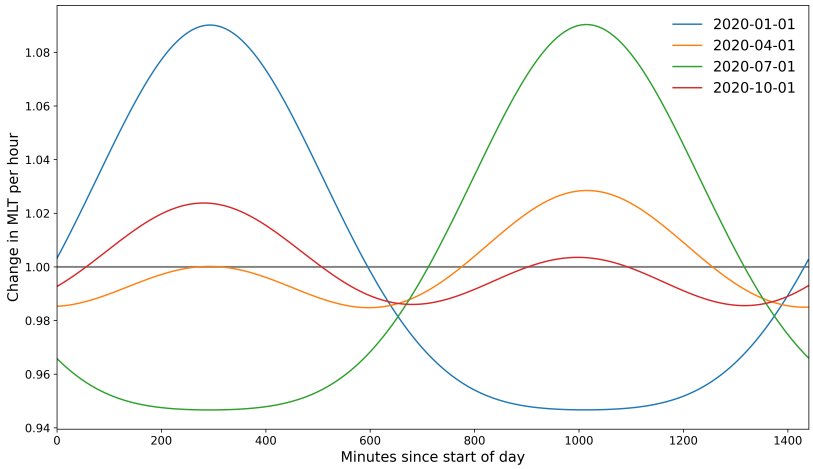

Figure 4.2: Variation in the rate of change in MLT per hour across different UTs and days of the year (seasons).

Nonetheless, upon normalising v_e to account for the varying rotation rate, it was found that this effect has minimal impact on our results and the conclusions drawn in Paper III. We therefore opted to disregard it in the rest of the study.

4.3.3 Potential implications on ionospheric electrodynamics

The MLat profiles of the theoretical and observed corotation flows reveal that plasma convection exhibits a significant eastward velocity in certain regions of the closed magnetosphere, despite a lag compared to the anticipated velocity for pure corotation. Paper III also presents the potential consequences of this lag in terms of magnetic disturbances and energy dissipation through Joule heating in the ionosphere. In this section, we describe our approach to derive these predictions and the underlying assumptions.

Using Lompe to quantify the current system and Joule heating

The Local Mapping of Polar Ionospheric Electrodynamics (Lompe) technique creates a self-consistent model of the ionospheric potential electric field by mapping various quantities (e.g., ground and space magnetic field measurements, convection measurements) using ionospheric Ohm's law given a known conductance (*Laundal et al.*, 2022b).

In Lompe, the horizontal electric field is calculated in the reference frame of the neutrals, $\mathbf{E} = (\mathbf{u} - \mathbf{v}) \times \mathbf{B}$, provided radial magnetic field lines. The neutral wind velocity $\mathbf{u}$ is determined by a height-integrated neutral wind weighted by the conductivity, meaning that the winds at $100 - 150$ km altitude dominate. A common assumption is that the neutral wind effects can be neglected, i.e., $\mathbf{u} = \mathbf{0}$ at these altitudes (e.g., *Lu*, 2017; *Laundal et al.*, 2022b; *Hatch et al.*, 2023). In our case, a "zero neutral wind" means that the atmospheric neutral particles are perfectly synchronised with Earth's rotation at $100 - 150$ km altitude.

Given the results from Paper III, assuming the neutral atmosphere fully corotates implies a differential motion relative to the sub-corotating plasma. This, in turn, induces a current through collisions, resulting in magnetic perturbations and deposition of energy through Joule heating in the ionosphere. These variations in the ionospheric electrodynamics can be predicted from the ionospheric Ohm's law, using the Lompe technique. Under the zero-neutral wind assumption, the electric field resulting from the observed corotation lag is given by $\mathbf{E} = -\mathbf{v}_{\text{lag}} \times \mathbf{B}$. This presumes that the electric field in the upper ionosphere and magnetosphere, where the corotation lag is measured, maps down to lower altitudes, where $\mathbf{u} = \mathbf{0}$. In other words, the input for Lompe is the westward velocity implied by the lag between neutrals, assumed to corotate at $100 - 150$ km, and plasma at ~ 300 km and above. Specifically, $\mathbf{v}_{\text{lag}}$ corresponds to a polynomial fit to the corotation lag computed in the Northern Hemisphere.

The horizontal sheet current density $\mathbf{J}$ associated with the corotation lag is given by the ionospheric Ohm's law (see Equation 2.2 in Section 2.3.4), where the Hall and Pedersen conductances are based on a model of solar EUV ionization and correspond to the ionization obtained for an F10.7 (solar radio flux at 10.7 cm) index of 100 solar flux units (with 1 s.f.u. defined as 10^{-22} W m^{-2} Hz^{-1}). Ionization produced by auroral precipitation is not included in our calculations.

The Joule heating is subsequently calculated as $\mathbf{J} \cdot \mathbf{E}$. Furthermore, the field-aligned current $\mathbf{J}_{\parallel}$ is calculated as the negative divergence of the horizontal current $\mathbf{J}$ and is assumed to flow radially. MLat–MLT distributions of the Joule heating and currents implied by the corotation lag are presented in Figure 2 of Paper III.

Discussion around the zero neutral wind assumption

Our findings regarding potential implications of the corotation lag on the ionosphere assume the absence of neutral wind in the ionospheric Ohm's law. While this assumption is commonly used, it may not accurately reflect real-world conditions. A more realistic scenario would involve the presence of westward neutral winds at $100-150$ km. Accounting for such winds in the ionospheric Ohm's law could significantly alter our estimates of currents and Joule heating. We emphasise that, if verified, the non-zero neutral wind hypothesis would necessitate revisiting prior studies that presume $\mathbf{u} = \mathbf{0}$

4.4 Uncertainties

Identifying and addressing uncertainties is crucial for validating methods and ensuring the consistency of analyses and results. In this section, we introduce and discuss some sources of uncertainty related to our data and methodology, along with their implications.

Data quality

DMSP/SSJ data: A significant source of uncertainty often lies in the data itself. In particular, uncertainties in the energy flux of DMSP/SSJ data points may influence the distributions of POP derived in Paper I. However, our investigations in Papers I and II reveal that variations in the chosen threshold for aurora detection generally have a minimal effect on the distributions of occurrence probability. As a result, the occurrence probability is generally insensitive to the uncertainties in the energy flux and these uncertainties can be neglected. Moreover, given our emphasis on qualitative analysis over quantitative, minor measurement uncertainties will not alter the study's conclusions. This highlights the robustness of the auroral occurrence probability method for analysing large-scale, long-term patterns of the auroral region (Papers I and II).

Cluster/EDI mapping: Swarm/VFM (Paper II) and Cluster/EDI (Paper III) measurements are highly accurate, owing to the specific design and characteristics of the satellites and instruments (see Sections 3.2 and 3.3). However, potential uncertainties may arise from the mapping of Cluster/EDI data to ionospheric altitudes, using the Tsyganenko 2001 magnetic field model (*Tsyganenko*, 2002a,b). Since the magnetosphere is highly dynamic, it is expected to often deviate from the large-scale average representation of the Tsyganenko model. This means that data points taken in the magnetosphere may be incorrectly mapped to the ionosphere, resulting in their misplacement in our MLat–MLT grid. However, since our data primarily originates from the lobes and high-latitude plasma sheet, which are relatively stable compared to regions like the central plasma sheet, any mapping errors are likely to be minor. In addition, by calculating median values in each cell of the grid, we avoid the most problematic data points and limit the effect of mislocation.

Methodology

DMSP orbits: Beyond measurement quality, the distribution of data can also introduce uncertainties, depending on the method employed. For instance, modelling auroral boundaries using Sun-synchronous satellites like DMSP (Paper I) may introduce a local time bias, as discussed in Section 4.1. Nonetheless, the auroral occurrence probability method has demonstrated its ability to address this challenge. Additionally, the extensive datasets used in Papers I and II reduce the risk of biased data distribution and yield low uncertainties associated with our probability calculations, reinforcing the overall reliability of our approach.

Statistical analysis: Eventually, statistical analyses themselves introduce uncertainties in interpreting results. Notably, they tend to smooth out small-scale variations, a tendency that can be exacerbated depending on the data filtering methods. For in-

stance, selecting data based on B_z may not fully resolve substorm variations, while choosing data by substorm epoch may not fully capture variations attributed to dayside coupling. Nonetheless, any issue related to such uncertainty can be discarded for the auroral occurrence probability patterns as Papers I and II demonstrated their consistency across various data selections. Furthermore, representations based on data collected over a broad time range offer a static picture of the system being studied and fail to capture its dynamic nature. In other words, the auroral occurrence probability maps derived in Papers I and II provide a climatological view of the auroral region rather than precisely reflecting its state at any given moment. Similarly, the corotation patterns derived in Paper III describe a general trend rather than a direct observation of the corotation in the magnetosphere.

In summary, addressing the potential uncertainties introduced in this thesis contributes to demonstrating the reliability of our statistical representations of the auroral region and magnetospheric convection, further validating the findings from Papers I-III.

5 Summary of papers

This thesis investigates the complex relationship between ionospheric and magnetospheric dynamics. Our focus is on unravelling what shapes the auroral region and exploring the connections between its morphology and the Earth's rotation.

The main part of the work has been presented in three separate scientific papers (Papers I, II and III), which are included in the last section of this thesis. Here, we summarise the goals, data and methods used, along with the major findings for each paper. The implications for all three papers are collectively discussed in the next chapter.

Paper I - Auroral Oval Morphology: Dawn-Dusk Asymmetry Partially Induced by Earth's Rotation

In Paper I, we aim to understand the shape of the auroral region in relation to large-scale magnetospheric plasma dynamics.

We develop a statistical method to characterise the auroral region morphology using approximately 20 years of electron energy flux measurements from DMSP/SSJ. Our approach consists of deriving the occurrence probability of auroral electron precipitation in the polar region instead of relying on the determination of the boundaries of the auroral oval. The analysis focuses on the total energy flux of electrons in the energy range $1-30$ keV. We use a threshold of $2 \cdot 10^9$ eV/cm^2/s/sr, similar to the one defined in *Kilcommons et al.* (2017) for the identification of candidate auroral regions. All energy flux measurements of precipitating electrons above this threshold are deemed to be aurora. We then calculate the probability of detecting auroral precipitation in each bin of an MLat–MLT grid combining both hemispheres and spanning $50^\circ - 90^\circ$ MLat and all MLT sectors covered by the DMSP satellites. The resulting auroral electron precipitation occurrence probability is referred to as AOP in Paper I (for auroral occurrence probability), and POP in the thesis and Paper II (for precipitation occurrence probability).

We derive maps of POP according to various conditions related to geomagnetic activity. We show that all POP distributions evince a clear and persistent asymmetric pattern with a wider dawn-to-noon sector ($06-12$ MLT) compared to the dusk-to-midnight sector ($18-24$ MLT). This asymmetry remains remarkably consistent regardless of variations in the auroral detection threshold and substorm epoch. While the dawn preference persists across various geomagnetic activity conditions, the asymmetry decreases during disturbed times.

We analyse these findings from a fluid perspective, where the interactions between the magnetosphere and ionosphere – specifically the auroral region – are examined through the bulk motion of plasma. In an elementary model, we represent the plasma sheet magnetic flux as a one-dimensional steady-state fluid subject to production and loss through magnetic reconnection. The modelled plasma convection is driven by both the solar wind and the planetary rotation. When compared, we find clear similarities between the modelled plasma and the MLT variation of POP in terms of dawn-dusk

asymmetries. The asymmetry in the distribution of POP is interpreted as a pile-up of plasma sheet magnetic flux in the dawn sector. We propose that the Earth's rotation is partially responsible for transporting more plasma towards dawn compared to dusk.

Paper II - Occurrence Probability of Magnetic Field Disturbances Measured With Swarm: Mapping the Dynamic Magnetosphere-Ionosphere Coupling

In Paper II, our primary objective is to investigate the relationship between magnetic disturbances observed in the auroral region and the dynamics of the magnetosphere.

We use magnetic field data from approximately $2 \cdot 10^5$ Swarm/VFM polar passes and an approach similar to the one developed in Paper I to derive the occurrence probability of magnetic field fluctuations in the polar ionosphere. Our method consists of three steps. First, we calculate the spectral power of the east-west component of the magnetic perturbations in the frequency bands $0.1 - 1$ and $2.5 - 5$ Hz. Second, we set a threshold corresponding to the 75th quantile of the ΔB_{EW} spectral power, and we determine which measurements of the magnetic field are substantially disturbed. Third, we compute the probability of detecting a disturbed magnetic field (dBOP, for disturbed magnetic field occurrence probability) on the same MLat–MLT grid as in Paper I.

We derive maps of dBOP for different geomagnetic conditions in both low- and high-frequency bands. Our findings reveal that the high-probability region of disturbed magnetic field approximately forms an oval around the magnetic pole. Additionally, the dBOP distributions are characterised by a prominent peak on the dayside, particularly evident during periods of low geomagnetic activity. We show that at low frequencies, the dBOP is largely marked by a dawn-dusk asymmetry with larger occurrence probabilities in the dawn sector. This pattern persists regardless of the sign of B_z or the substorm phase. However, during active times, the asymmetry diminishes as the dBOP experiences heightened levels, especially on the nightside. At higher frequencies, we show that the dBOP distributions are dominated by an asymmetry between dayside and nightside, with a persistent peak on the dayside.

We observe a consistent preference for dawn in both POP (Paper I) and low-frequency dBOP, along with a comparable response to variations in geomagnetic activity. Particularly noteworthy is the increased asymmetric pattern during quiet periods. Although we do not presume any direct correlation between a disturbed magnetic field and the auroral oval, we posit that the combined analysis of POP and dBOP is valuable for exploring the characteristics of the auroral region. Furthermore, we identify a high correlation between the low-frequency dBOP and the auroral oval boundaries derived from small- and medium-scale FACs (*Xiong et al.*, 2014). Our interpretation is that the low-frequency disturbed magnetic field reflects the large-scale, steady-state coupling between the ionosphere and magnetosphere. Conversely, at higher frequencies, the dBOP reflects more active regions of the magnetosphere and a more dynamic M-I coupling.

Paper III - Revealing the effect of Earth's rotation on the geospace

In Paper III, our focus is on elucidating the influence of Earth's rotation on magnetospheric convection patterns. In particular, we seek to empirically validate the hypothesis proposed in Paper I, suggesting that the Earth's rotation plays a role in the transport of magnetic flux within the plasma sheet.

We use Cluster/EDI measurements of plasma convection to quantify the corotation in the magnetosphere. The data is obtained from the high-latitude plasma sheet and lobes and subsequently mapped along magnetic field lines to ionospheric altitudes. We present MLat–MLT distributions of the convection velocity vectors and derive MLat profiles of the corotation flow. These profiles enable comparison between the average eastward velocity (observed corotation) and a theoretical corotation velocity representing a hypothetical plasma perfectly synchronised with the Earth's rotation.

Our results show clear evidence of the impact of the Earth's rotation on the convection velocities at auroral latitudes and equatorward. Similarly, the corotation profiles reveal a prevailing latitude-dependent eastward velocity in the magnetosphere, indicating subcorotation of the high-latitude plasma sheet. The lag compared to pure corotation peaks around auroral latitudes.

Assuming the neutral atmosphere is stationary with respect to the Earth (zero-neutral wind assumption), the observed lag implies a relative motion between neutral particles and magnetospheric plasma, which leads to collisional heating. Using the Lompe technique, we predict and analyse the resulting currents and energy deposition in the ionosphere. Another key aspect of the study is how magnetospheric corotation may impact the magnetic field topology. In particular, we illustrate how differential motion between the fixed central plasma sheet (*Pitkänen et al.*, 2019) and the corotating high-latitude plasma sheet can lead to the distortion of plasma sheet magnetic field lines. We propose that the deformation of the field lines generates an eastward force, resulting in a greater transport of plasma from the nightside towards dawn compared to dusk. This suggests a potential mechanism behind the dawn preference in auroral electron precipitation and auroral magnetic field disturbance patterns documented in Papers I and II, respectively.

6 Conclusions and future trajectories

The research conducted in this thesis was driven by the motivation to uncover the factors influencing the auroral region's formation and comprehend the impact of Earth's rotation on magnetospheric convection. The common aim of Papers I–III was to explore how magnetospheric fluid dynamics and ionospheric observations are connected. The papers included in this thesis collectively tackle these objectives. The key findings from each paper are summarised in this chapter, along with a brief discussion of potential directions for further research.

Concluding insights

Papers I and II address the specific question of the shape of the auroral region. Using a novel method of characterisation based on different proxies, our findings corroborate results from earlier studies:

- The large-scale, long-term morphology of the auroral region is notably described by the occurrence probability distributions of $1-30$ keV electron precipitation and $0.1-1$ Hz disturbed magnetic field.
- The auroral region exhibits a persistent dawn-dusk asymmetry, with high occurrence probabilities spread over a larger latitudinal range in the dawn sector.
- The asymmetric pattern is decreased during high geomagnetic activity, due to the auroral region expanding primarily on the nightside in such conditions.

Additionally, Papers I and II demonstrate how ionospheric observations yield a means to understand and study magnetospheric dynamics:

- The spatial distribution of $1-30$ keV electron precipitation is related to the large-scale circulation of magnetic flux in the magnetospheric plasma sheet.
- $0.1-1$ Hz magnetic field fluctuations reflect the large-scale, steady-state coupling between the ionosphere and magnetosphere.
- $2.5-5$ Hz magnetic field fluctuations are indicative of regions in the ionosphere that are directly responding to the dynamic coupling between the solar wind and the magnetosphere, typically the noon and midnight sectors.

Furthermore, Paper I elaborates on the concept of mapping between the ionosphere and magnetosphere as seen from a fluid perspective, and suggests the following hypotheses:

- The auroral region's asymmetric shape could be due to a pile-up of plasma sheet magnetic flux in the dawn sector.
- The effect of the Earth's rotation on the plasma convection pattern could be responsible for the excess magnetic flux transport towards dawn.

Finally, building upon the results from Papers I and II regarding the auroral region's dawn-dusk asymmetry and its origin, Paper III provides insight into the influence of Earth's rotation on magnetospheric dynamics and its potential implications on the ionosphere. Its key results are:

- The plasma motion in the high-latitude plasma sheet is, to some extent, synchronised with Earth's rotation, unlike the central plasma sheet and magnetospheric lobes.
- Plasma sheet magnetic field lines and the plasma attached to them are preferentially displaced towards the dawn side of the magnetosphere.
- Assuming the neutral atmosphere fully corotates with Earth, the lag between neutral particles and magnetospheric plasma results in currents and Joule heating in the ionosphere.

In conclusion, the combined findings from Papers I, II, and III illuminate essential aspects of the auroral region's morphology and its complex connection to magnetospheric dynamics. Our results demonstrate the utility of electron precipitation and magnetic perturbations in the ionosphere not only as proxies for the auroral region but also as footpoints of the large-scale circulation of plasma and magnetic flux in the magnetosphere. Through the occurrence probability of auroral electron precipitation (POP) and disturbed magnetic field (dBOP), our studies confirm and expand upon earlier research, shedding light on the persistent dawn-dusk asymmetry in the auroral region where there is a clear preference for the dawn sector. Moreover, our research offers valuable insights into the impact of the Earth's rotation on magnetospheric plasma convection and its potential implications in terms of ionospheric electrodynamics. Together, our investigations suggest that the Earth's rotation influences the large-scale plasma convection pattern in the magnetosphere, which, in turn, participates in shaping the asymmetric auroral region. In particular, the dawn preference in the auroral region could result from an excess transport of magnetic flux due to the corotation of the high-latitude plasma sheet.

The research performed in connection with this thesis ultimately contributes to a deeper understanding of the complex M-I coupling, challenging the established paradigm according to which plasma convection is solely driven by the interactions between solar wind and magnetosphere. Figure 6.1 offers a simplified overview, attempting to capture the main aspects studied in this thesis.

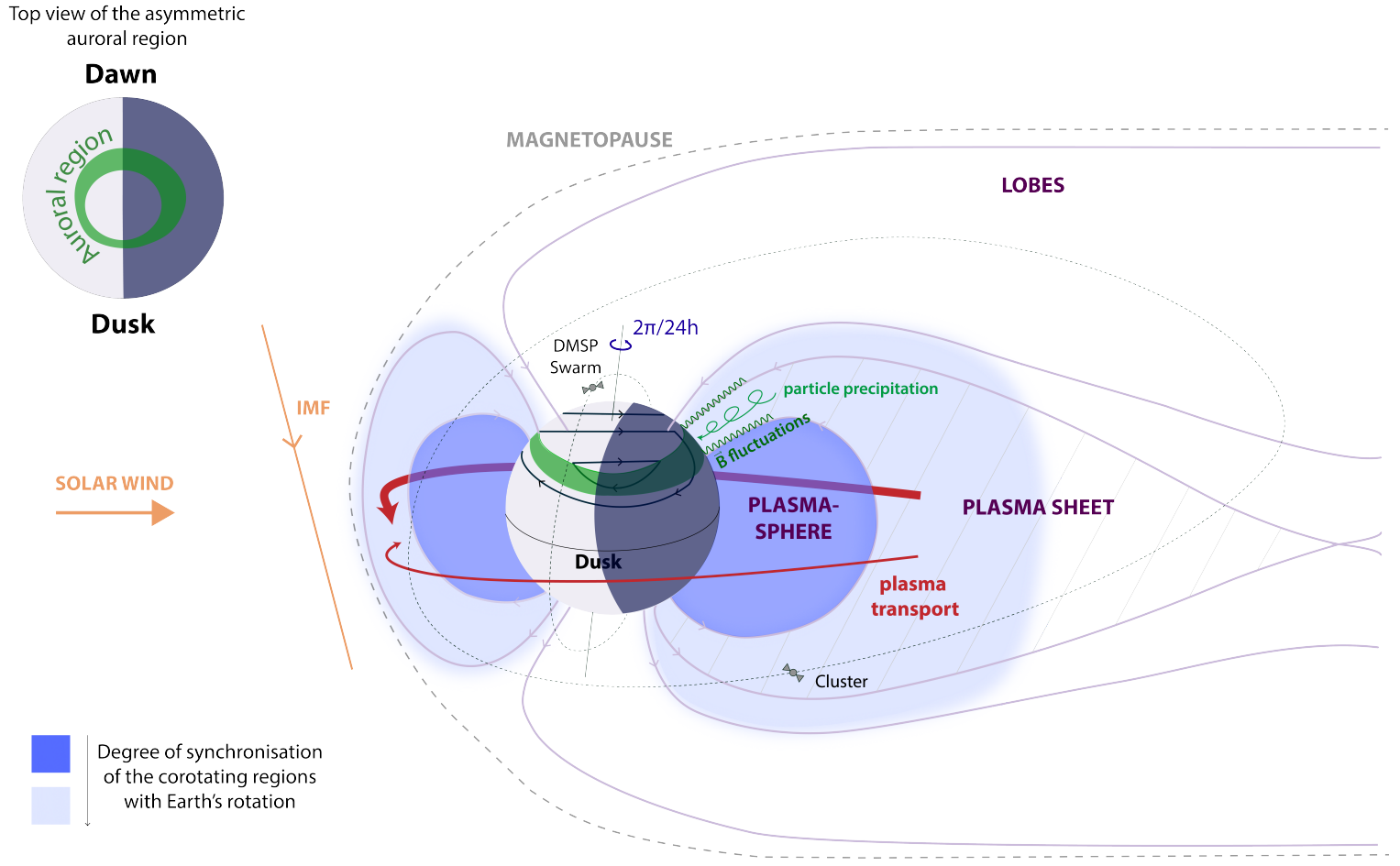

Figure 6.1: Summary illustration showcasing the topology of Earth's magnetosphere-ionosphere environment, highlighting fundamental phenomena investigated in this thesis and some major findings. *Figure adapted from Paper III.*

Future research

The research carried out in this thesis has opened new perspectives for future investigations. Moving forward, several directions merit exploration to advance our understanding of M-I coupling and beyond.

Expanding upon the insights derived from Paper III, future studies could aim to directly observe and characterise the corotation and its effects within the ionosphere. Additionally, new insights into the influence of ionospheric convection on the magnetosphere could be gained by conducting MHD simulations with and without Earth's rotation.

Future research could also explore how Earth's rotation impacts the atmosphere's dynamics. In particular, investigating the atmospheric global response to plasma-neutral interactions would shed light on the potential mechanisms driving atmospheric motion and heat distribution. Simulations of the upper atmosphere could provide an opportunity to assess the impact of Joule heating induced by the corotation lag. This further prompts questions such as whether the neutral atmosphere tends to align with plasma motion to reduce or stop the heating, or what occurs if the atmosphere is continuously exposed to heating.

Furthermore, dedicated studies centred on the magnetic field offer promising prospects for additional investigation. For instance, future work could involve confirming the presence of large-scale, low-intensity FACs in the M-I coupling region, as predicted by the Lompe technique for a given corotation lag. Despite the relatively weak and consistent nature of these currents, their accurate characterisation would improve the refinement of the Earth's main magnetic field models. This is particularly pertinent as distinguishing contributions from stable ionospheric currents and the terrestrial core remains an area of active research. Such studies, coupled with simulations of the neutral wind, could further allow for verifying the widely used assumption of zero-neutral wind in the atmosphere.

Building upon the findings and hypotheses presented in Papers I–III, follow-up studies could investigate how the plasma sheet precisely shapes the auroral region. Moreover, drawing inspiration from studies on Jupiter's unique magnetic topology and its impact on auroral emissions, there is an opportunity for analogous investigations on Earth.

In summary, future research efforts guided by the findings of this thesis hold the potential to significantly advance our understanding of M-I coupling dynamics and their broader implications for Earth's atmospheric and geospace environment.

Ultimately, any subsequent investigations would ideally corroborate the wisdom of a great man who once proclaimed: *And now, all mankind can finally rest their eyes knowing that Earth rotates. (K.M.L.)*

7 LEGO model of the magnetosphere

As a major side project of this thesis, we constructed a LEGO model of the magnetosphere. The LEGO model has been thought of as a creative and engaging pedagogical tool for illustrating the complex influence of the solar wind on the magnetosphere, in a simple and visual way. Note that this model aligns with the fluid description of the solar wind-magnetosphere-ionosphere coupling outlined in Chapter 2.

7.1 Principle

In the late 1980s, there was an active discussion about the roles of direct energy input from the solar wind and the release of stored magnetotail energy in driving substorms (*Akasofu*, 1985; *Rostoker et al.*, 1987) (see also Section 2.3.5). *Akasofu* (1989) ultimately proposed to illustrate the two-step response of the magnetosphere to changes in the solar wind by identifying the magnetosphere as a combination of a pitcher-type (directly driven component) and a tippy-bucket-type (unloading component) system, as shown in Figure 7.1.

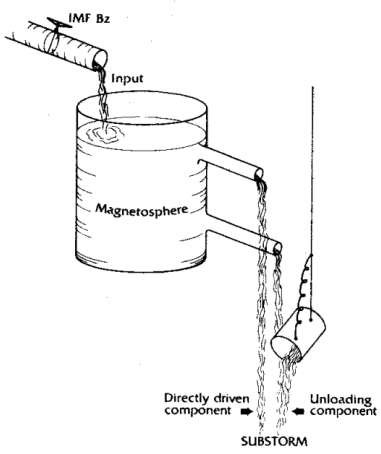

Figure 7.1: Schematic illustration showing the flow of energy from the solar wind through the magnetosphere represented by a combination of the pitcher and tippy bucket models. *Taken from Akasofu (1989).*

The idea of a LEGO machine based on Akasofu's model emerged after the publication of Laundal et al. 2020, where they quantified the time-scale dependent statistical relationship between nightside and dayside reconnection rates, as well as its effect on solar wind-based regression models of ionospheric electrodynamic parameters. This paper is based on the concept that the solar wind influence on the magnetosphere can be described as the sum of a directly driven component –dayside reconnection– and an unloading component associated with the release of magnetic energy via nightside reconnection.

Our LEGO model uses Akasofu's representation to illustrate this concept and aims to emulate the M-I system's mechanical behaviour.

7.2 Development

The model consists of two water-driven wheels simulating magnetospheric reconnection on the dayside and nightside, along with a rotating platform representing the ionospheric convection pattern, all constructed from LEGO bricks.

To implement Akasofu's model, we incorporated a water source, serving as constant input analogous to the solar wind, for the dayside wheel. Additionally, a LEGO bucket mimics the magnetospheric lobes. While the dayside wheel maintains continuous motion, the bucket stores the water that entered the system through the first wheel (dayside reconnection) and explosively releases it by tipping, thereby activating the second wheel (nightside reconnection) only momentarily.

A LEGO differential gear enables the combination of inputs from both wheels. The movement of the dayside wheel initiates the rotation of the ionospheric convection system, with rotational speed increasing when both wheels operate simultaneously. Furthermore, a set of green LEDs, along with a motion sensor attached to the bucket, produces aurora on top of a globe following the nightside reconnection event triggered by the release of water from the tippy bucket.

Our interactive model allows for adjustments to the water input (approximating reconnection rates) to demonstrate corresponding changes in ionospheric convection dynamics (rotational velocity).

Figure 7.2 shows a collection of pictures of the LEGO machine and its different elements.

7.3 Result

We presented a prototype of the LEGO model at the Fysikermøtet 2023 in Bergen, where we demonstrated to researchers and teachers in physics how the magnetosphere influences the ionosphere through both direct and unloading components. The model received significant interest, supporting our ulterior motive that this LEGO machine could be further used as a tool for space physics outreach initiatives. Furthermore, the machine was exhibited during an open day at the Science Museum Vilvite targeted at 10-12-year-old children. It served as a starting point for interesting questions and discussions on the topic of auroral and space physics.

While our model has proved its effectiveness in capturing curiosity, we believe it could be further used as a didactic tool for explaining aspects of M-I coupling to undergraduate and graduate students. The LEGO model will be showcased at more events/conferences, where we anticipate receiving valuable feedback to further refine and enhance our prototype.

Figure 7.2: LEGO machine modelling the magnetosphere-ionosphere system's mechanical behaviour. The central (middle top) picture shows how the various elements comprising our LEGO model assemble to form the final machine. Surrounding the central image are additional photos displaying the individual elements. The dayside wheel is shown in the top left photo. Below it, the photos feature the tippy bucket and nightside wheel. Moving to the top right, the two-cell rotating platform illustrates the typical ionospheric convection pattern. In the bottom right corner, our LEGO model is presented to the public at Vilvite, Bergen Science Center. The two middle bottom pictures show the globe and the aurora display over the polar region.

List of Abbreviations

AL Auroral Lower geomagnetic index

AOP Auroral Occurrence Probability

dBOP disturbed magnetic field Occurrence Probability

DMSP Defense Meteorological Satellite Program

ECPC Expanding-Contracting Polar Cap

EDI Electron Drift Instrument

eV electronvolt

FAC Field-Aligned Current

GSM Geocentric Solar Magnetospheric coordinate system

IGRF International Geomagnetic Reference Field

IMF Interplanetary Magnetic Field

IO I'm Okay

M-I Magnetosphere-Ionosphere

MHD MagnetoHydroDynamics

OCB Open-Closed Boundary

POP auroral electron Precipitation Occurrence Probability

SSJ Special Sensor J

SYM-H Symmetric Horizontal disturbance geomagnetic index

VFM Vector Field Magnetometer

Bibliography

Akasofu, S.-i. (1963), The dynamical morphology of the aurora polaris, *Journal of Geophysical Research*, *68*(6), 1667–1673, doi:10.1029/jz068i006p01667. 2

Akasofu, S. I. (1964), The development of the auroral substorm, *Planetary and Space Science*, *12*(4), 273–282, doi:10.1016/0032-0633(64)90151-5. 18

Akasofu, S. I. (1985), Energy supply processes for magnetospheric substorms and solar flares: Tippy bucket model or pitcher model?, *Astrophysics and Space Science*, *108*(1), 81–93, doi:10.1007/BF00650120/METRICS. 18, 51

Akasofu, S.-I. (1989), Substorms: Future of magnetospheric substorm—Storm research, *Eos, Transactions American Geophysical Union*, *70*(16), 529–538, doi:10.1029/89EO00121. 51

Akasofu, S. I. (2017), Auroral Substorms: Search for Processes Causing the Expansion Phase in Terms of the Electric Current Approach, *Space Science Reviews*, *212*(1-2), 341–381, doi:10.1007/s11214-017-0363-7. 18

Badman, S. V., and S. W. H. Cowley (2007), Significance of Dungey-cycle flows in Jupiter's and Saturn's magnetospheres, and their identification on closed equatorial field lines, *Annales Geophysicae*, *25*(4), 941–951, doi:10.5194/angeo-25-941-2007. 14

Baumjohann, W., and R. A. Treumann (2012), Basic space plasma physics (revised edition), *Basic Space Plasma Physics (Revised Edition)*, pp. 1–479, doi:10.1142/P850. 8, 15, 16, 20, 21, 24

Baumjohann, W., G. Paschmann, N. Sckopke, C. A. Cattell, and C. W. Carlson (1988), Average ion moments in the plasma sheet boundary layer, *Journal of Geophysical Research*, *93*(A10), 11,507, doi:10.1029/ja093ia10p11507. 19

Baumjohann, W., G. Paschmann, and C. A. Cattell (1989), Average plasma properties in the central plasma sheet, *Journal of Geophysical Research: Space Physics*, *94*(A6), 6597–6606, doi:10.1029/ja094ia06p06597. 19

Blanc, M. (1988), Magnetosphere-ionosphere coupling, *Computer Physics Communications*, *49*(1), 103–118, doi:10.1016/0010-4655(88)90219-6. 2

Blanc, M., R. Kallenbach, and N. Erkaev (2005), *Solar System Magnetospheres*, 227–298 pp., Springer, Dordrecht, doi:10.1007/1-4020-4038-5{_}15. 13

Boakes, P. D., R. Nakamura, M. Volwerk, and S. E. Milan (2014), ECLAT Cluster Spacecraft Magnetotail Plasma Region Identifications (2001–2009), *Dataset Papers in Science*, *2014*, 1–13, doi:10.1155/2014/684305. 19

Borovsky, J. E., and J. A. Valdivia (2018), The Earth's Magnetosphere: A Systems Science Overview and Assessment, *Surveys in Geophysics*, *39*(5), 817–859, doi:10.1007/S10712-018-9487-X/TABLES/7. 2

Borovsky, J. E., M. F. Thomsen, R. G. Elphic, T. E. Cayton, and D. J. McComas (1998), The transport of plasma sheet material from the distant tail to geosynchronous orbit, *Journal of Geophysical Research: Space Physics*, *103*(A9), 20,297–20,331, doi:10.1029/97ja03144. 19

Breddels, Maarten A., and Veljanoski, Jovan (2018), Vaex: big data exploration in the era of Gaia, *A&A*, *618*, A13, doi:10.1051/0004-6361/201732493. 27

Brekke, A. (2013), *The aurora*, 317–369 pp., Springer, Berlin, Heidelberg, doi:10.1007/978-3-642-27401-5{_}7. 21

Burch, J. L., J. Goldstein, and B. R. Sandel (2004), Cause of plasmasphere corotation lag, *Geophysical Research Letters*, *31*(5), doi:10.1029/2003GL019164. 13, 14

Burrell, A. G., G. Chisham, S. E. Milan, L. Kilcommons, Y. J. Chen, E. G. Thomas, and B. Anderson (2020), AMPERE polar cap boundaries, *Annales Geophysicae*, *38*(2), 481–490, doi:10.5194/angeo-38-481-2020. 16, 27

Chané, E., J. Saur, and S. Poedts (2013), Modeling Jupiter's magnetosphere: Influence of the internal sources, *Journal of Geophysical Research: Space Physics*, *118*(5), 2157–2172, doi:10.1002/JGRA.50258. 14

Chaston, C. C., C. W. Carlson, W. J. Peria, R. E. Ergun, and J. P. McFadden (1999), FAST Observations of Inertial Alfven Waves in the Dayside Aurora, *Geophysical Research Letters*, *26*(6), 647–650, doi:10.1029/1998GL900246. 23

Chaston, C. C., J. W. Bonnell, C. W. Carlson, J. P. McFadden, R. E. Ergun, and R. J. Strangeway (2003), Properties of small-scale Alfvén waves and accelerated electrons from FAST, *Journal of Geophysical Research: Space Physics*, *108*(A4), 8003, doi:10.1029/2002JA009420. 22, 23

Chisham, G., M. P. Freeman, G. A. Abel, M. M. Lam, M. Pinnock, I. J. Coleman, S. E. Milan, M. Lester, W. A. Bristow, R. A. Greenwald, G. J. Sofko, and J. P. Villain (2008), Remote sensing of the spatial and temporal structure of magnetopause and magnetotail reconnection from the ionosphere, *Reviews of Geophysics*, *46*(1), doi:10.1029/2007RG000223. 19, 25

Chisham, G., A. G. Burrell, E. G. Thomas, and Y. J. Chen (2022), Ionospheric Boundaries Derived From Auroral Images, *Journal of Geophysical Research: Space Physics*, *127*(7), 1–19, doi:10.1029/2022JA030622. 12

Cowley, S., and M. Lockwood (1992), Excitation and decay of solar-wind driven flows in the magnetosphere-ionosphere system, *Annales Geophysicae*. 1, 11

Cowley, S. W. (2000), Magnetosphere-Ionosphere Interactions: A Tutorial Review, *Geophysical Monograph Series*, *118*, 91–106, doi:10.1029/GM118P0091. 15

Cowley, S. W., and E. J. Bunce (2003), Corotation-driven magnetosphere-ionosphere coupling currents in Saturn's magnetosphere and their relation to the auroras, *Annales Geophysicae*, *21*(8), 1691–1707, doi:10.5194/ANGEO-21-1691-2003. 25

Cowley, S. W., E. J. Bunce, T. S. Stallard, and S. Miller (2003), Jupiter's polar iono-

spheric flows: Theoretical interpretation, *Geophysical Research Letters*, *30*(5), 1220, doi:10.1029/2002GL016030. 14, 25

Cowley, S. W. E. (1981), Magnetospheric asymmetries associated with the y-component of the IMF, *Planetary and Space Science*, *29*, 79–96. 10

Cowley, S. W. H., E. J. Bunce, and R. Prangé (2004), Saturn's polar ionospheric flows and their relation to the main auroral oval, *Annales Geophysicae*, *22*, 1379–1394. 14, 25

Dai, L., M. Zhu, Y. Ren, W. Gonzalez, C. Wang, D. Sibeck, A. Samsonov, P. Escoubet, B. Tang, J. Zhang, and G. Branduardi-Raymont (2024), Global-scale magnetosphere convection driven by dayside magnetic reconnection, *Nature Communications 2024 15:1*, *15*(1), 1–8, doi:10.1038/s41467-024-44992-y. 25

Dombeck, J., C. Cattell, N. Prasad, E. Meeker, E. Hanson, and J. McFadden (2018), Identification of Auroral Electron Precipitation Mechanism Combinations and Their Relationships to Net Downgoing Energy and Number Flux, *Journal of Geophysical Research: Space Physics*, *123*(12), 064–10, doi:10.1029/2018JA025749. 22, 23

Dungey, J. W. (1961), Interplanetary magnetic field and the auroral zones, *Physical Review Letters*, *6*(2), 47–48, doi:10.1103/PhysRevLett.6.47. 10, 13

Elphic, R. C., M. F. Thomson, J. E. Borovsky, and D. J. McComas (1999), Inner edge of the electron plasma sheet: Empirical models of boundary location, *Journal of Geophysical Research: Space Physics*, *104*(A10), 22,679–22,693, doi:10.1029/1999JA900213. 19

Ergun, R. E., C. W. Carlson, J. P. McFadden, F. S. Mozer, G. T. Delory, W. Peria, C. C. Chaston, M. Temerin, R. Elphic, R. Strangeway, R. Pfaff, C. A. Cattell, D. Klumpar, E. Shelley, W. Peterson, E. Moebius, and L. Kistler (1998), FAST satellite observations of electric field structures in the auroral zone, *Geophysical Research Letters*, *25*(12), 2025–2028, doi:10.1029/98GL00635. 22

Feldstein, Y. I. (1964), Auroral morphology, II. Auroral and geomagnetic disturbances, *Tellus*, *16*(2), 252–257, doi:10.3402/tellusa.v16i2.8897. 23

Feldstein, Y. I. (2016), The discovery and the first studies of the auroral oval: A review, *Geomagnetism and Aeronomy*, *56*(2), 129–142, doi:10.1134/S0016793216020043. 2, 21

Feldsten, Y. I., and G. V. Starkov (1967), Dynamics of auroral belt and polar geomagnetic disturbances, *Planetary and Space Science*, *15*(2), 209–229, doi:10.1016/0032-0633(67)90190-0. 23

Förster, M., and S. Haaland (2015), Interhemispheric differences in ionospheric convection: Cluster EDI observations revisited, *Journal of Geophysical Research: Space Physics*, *120*(7), 5805–5823, doi:10.1002/2014JA020774. 30

Förster, M., G. Paschmann, S. E. Haaland, J. M. Quinn, R. B. Torbert, H. Vaith, and C. A. Kletzing (2007), High-latitude plasma convection from Cluster EDI: variances and solar wind correlations, *Annales Geophysicae*, *25*(7), 1691–1707, doi:10.5194/ANGEO-25-1691-2007. 30

Forsyth, C., S. E. Milan, and A. P. Walsh (2010), Magnetotails throughout the solar

system, *Astronomy and Geophysics*, *51*(6), 28–6, doi:10.1111/J.1468-4004.2010.51628.X/2/51-6-6.28-FIG001.GIF. 13

Frey, H. U. (2007), Localized aurora beyond the auroral oval, *Reviews of Geophysics*, *45*(1), 1–32, doi:10.1029/2005RG000174. 20

Frey, H. U., D. Han, R. Kataoka, M. R. Lessard, S. E. Milan, Y. Nishimura, R. J. Strangeway, and Y. Zou (2019), Dayside Aurora, *Space Science Reviews 2019 215:8*, *215*(8), 1–32, doi:10.1007/S11214-019-0617-7. 8, 20

Friis-Christensen, E., H. Lühr, D. Knudsen, and R. Haagmans (2008), Swarm – An Earth Observation Mission investigating Geospace, *Advances in Space Research*, *41*(1), 210–216, doi:https://doi.org/10.1016/j.asr.2006.10.008. 28

Gjerloev, J. W. (2012), The SuperMAG data processing technique, *Journal of Geophysical Research: Space Physics*, *117*(A9), 9213, doi:10.1029/2012JA017683. 31

Gjerloev, J. W., R. A. Hoffman, J. B. Sigwarth, L. A. Frank, and J. B. Baker (2008), Typical auroral substorm: A bifurcated oval, *Journal of Geophysical Research: Space Physics*, *113*(3), 1–16, doi:10.1029/2007JA012431. 18

Goertz, C. K. (1984), Kinetic Alfvén waves on auroral field lines, *Planetary and Space Science*, *32*(11), 1387–1392, doi:10.1016/0032-0633(84)90081-3. 17, 23

Gombosi, T. I., T. P. Armstrong, C. S. Arridge, K. K. Khurana, S. M. Krimigis, N. Krupp, A. M. Persoon, and M. F. Thomsen (2009), *Saturn's magnetospheric configuration*, 203–255 pp., Springer Netherlands, doi:10.1007/978-1-4020-9217-6{_}9/FIGURES/43{_}9. 13, 14

Grard, R., K. Knott, and Pedersen (1983), 2 . Charged Particle Exchanges between a Body and Its Environment in Space, in *Space Science Reviews*, May 1982, pp. 289–304, Springer. 30

Haaland, S., G. Paschmann, M. Fărster, J. Quinn, R. Torbert, H. Vaith, P. Puhl-Quinn, and C. Kletzing (2008), Plasma convection in the magnetotail lobes: statistical results from Cluster EDI measurements, *Annales Geophysicae*, *26*(8), 2371–2382, doi:10.5194/ANGEO-26-2371-2008. 30

Haaland, S. E., G. Paschmann, M. Förster, J. M. Quinn, R. B. Torbert, C. E. McIlwain, H. Vaith, P. A. Puhl-Quinn, and C. A. Kletzing (2007), High-latitude plasma convection from Cluster EDI measurements: Method and IMF-dependence, *Annales Geophysicae*, *25*(1), 239–253, doi:10.5194/angeo-25-239-2007. 30, 37

Hardy, D. A., M. S. Gussenhoven, and E. Holeman (1985), A statistical model of auroral electron precipitation, *Journal of Geophysical Research: Space Physics*, *90*(A5), 4229–4248, doi:10.1029/JA090IA05P04229. 27, 34

Hasegawa, A., and K. Mima (1976), Exact Solitary Alfvén Wave, *Physical Review Letters*, *37*(11), 690, doi:10.1103/PhysRevLett.37.690. 17

Hatch, S. M., T. Moretto, K. A. Lynch, K. M. Laundal, J. W. Gjerloev, and E. J. Lund (2020), The Relationship Between Cusp Region Ion Outflows and East-West

Magnetic Field Fluctuations at 4,000-km Altitude, *Journal of Geophysical Research: Space Physics*, *125*(3), 1–18, doi:10.1029/2019JA027454. 29

Hatch, S. M., H. Vanhamäki, K. M. Laundal, J. P. Reistad, J. K. Burchill, L. Lomidze, D. J. Knudsen, M. Madelaire, and H. Tesfaw (2023), Does high-latitude ionospheric electrodynamics exhibit hemispheric mirror symmetry?, *Preprint egusphere*, doi:10.5194/egusphere-2023-2920. 40

Holzworth, R. H., and C.-I. Meng (1975), Mathematical representation of the auroral oval, *Geophysical Research Letters*, *2*(9), 377–380, doi:https://doi.org/10.1029/GL002i009p00377. 23

Horwitz, J. L., S. Menteer, J. Turnley, J. L. Burch, J. D. Winningham, C. R. Chappell, J. D. Craven, L. A. Frank, and D. W. Slater (1986), Plasma boundaries in the inner magnetosphere, *Journal of Geophysical Research: Space Physics*, *91*(A8), 8861–8882, doi:10.1029/JA091IA08P08861. 19

Iijima, T., and T. A. Potemra (1976a), Field-aligned currents in the dayside cusp observed by Triad, *Journal of Geophysical Research*, *81*(34), 5971–5979, doi:10.1029/ja081i034p05971. 16

Iijima, T., and T. A. Potemra (1976b), The amplitude distribution of field-aligned currents at northern high latitudes observed by Triad, *Journal of Geophysical Research*, *81*(13), 2165–2174, doi:10.1029/ja081i013p02165. 16

Iijima, T., and T. A. Potemra (1978), Large-scale characteristics of field-aligned currents associated with substorms, *Journal of Geophysical Research*, *83*(A2), 599, doi:10.1029/ja083ia02p00599. 16

Juusola, L., N. Østgaard, E. Tanskanen, N. Partamies, and K. Snekvik (2011), Earthward plasma sheet flows during substorm phases, *Journal of Geophysical Research: Space Physics*, *116*(10), 1–11, doi:10.1029/2011JA016852. 18

Kan, J. R., and L. C. Lee (1979), Energy coupling function and solar wind-magnetosphere dynamo, *Geophysical Research Letters*, *6*(7), 577–580, doi:10.1029/GL006I007P00577. 8

Karlsson, T., A. Kullen, and G. Marklund (2017), Dawn-Dusk Asymmetries in Auroral Morphology and Processes, *Dawn-Dusk Asymmetries in Planetary Plasma Environments*, pp. 295–305, doi:10.1002/9781119216346.CH23. 23

Kauristie, K., J. Weygand, T. I. Pulkkinen, J. S. Murphree, and P. T. Newell (1999), Size of the auroral oval: UV ovals and precipitation boundaries compared, *Journal of Geophysical Research: Space Physics*, *104*(A2), 2321–2331, doi:10.1029/1998JA900046. 33

Keiling, A. (2021), The Dynamics of the Alfvénic Oval, *Journal of Atmospheric and Solar-Terrestrial Physics*, *219*(xxxx), doi:10.1016/j.jastp.2021.105616. 23

Keiling, A., J. R. Wygant, C. A. Cattell, F. S. Mozer, and C. T. Russell (2003), The global morphology of wave poynting flux: Powering the aurora, *Science*, *299*(5605), 383–386, doi:10.1126/SCIENCE.1080073/ASSET/7D89E0EE-9EDD-4B7D-9B55-6F3375F29B1C/ASSETS/GRAPHIC/SE0231188003.JPEG. 34

Khazanov, G. V., and A. Glocer (2020), How Magnetically Conjugate Atmospheres and the Magnetosphere Participate in the Formation of Low-Energy Electron Precipitation in the Region of Diffuse Aurora, *Journal of Geophysical Research: Space Physics*, *125*(8), 1–15, doi:10.1029/2020JA028057. 22

Kilcommons, L. M., R. J. Redmon, and D. J. Knipp (2017), A new DMSP magnetometer and auroral boundary data set and estimates of field-aligned currents in dynamic auroral boundary coordinates, *Journal of Geophysical Research: Space Physics*, *122*(8), 9068–9079, doi:https://doi.org/10.1002/2016JA023342. 27, 33, 34, 43

King, J. H., and N. E. Papitashvili (2005), Solar wind spatial scales in and comparisons of hourly Wind and ACE plasma and magnetic field data, *Journal of Geophysical Research: Space Physics*, *110*(A2), 2104, doi:10.1029/2004JA010649. 31

Knudsen, D. J., J. H. Clemmons, and J.-E. Wahlund (1998), Correlation between core ion energization, suprathermal electron bursts, and broadband ELF plasma waves, *Journal of Geophysical Research: Space Physics*, *103*(A3), 4171–4186, doi:10.1029/97JA00696. 23

Koskinen, H. E. J., and E. K. J. Kilpua (2022), *Physics of Earth's Radiation Belts*, Astronomy and Astrophysics Library, 272 pp., Springer Nature, Cham, doi:10.1007/978-3-030-82167-8. 20

Laundal, K. M., and A. D. Richmond (2017), Magnetic Coordinate Systems, *Space Science Reviews*, *206*(1), 27–59, doi:10.1007/s11214-016-0275-y. 10, 39

Laundal, K. M., N. OØstgaard, H. U. Frey, and J. M. Weygand (2010), Seasonal and interplanetary magnetic field-dependent polar cap contraction during substorm expansion phase, *Journal of Geophysical Research: Space Physics*, *115*(11), 1–12, doi:10.1029/2010JA015910. 12, 18

Laundal, K. M., M. Madelaire, A. Ohma, J. Reistad, and S. Hatch (2022a), The relationship between interhemispheric asymmetries in polar ionospheric convection and the magnetic field line footpoint displacement field, *Frontiers in Astronomy and Space Sciences*, *9*(July), 1–12, doi:10.3389/fspas.2022.957223. 37

Laundal, K. M., J. P. Reistad, S. M. Hatch, M. Madelaire, S. Walker, A. Hovland, A. Ohma, V. G. Merkin, and K. A. Sorathia (2022b), Local Mapping of Polar Ionospheric Electrodynamics, *Journal of Geophysical Research: Space Physics*, *127*(5), e2022JA030,356, doi:10.1029/2022JA030356. 40

Liou, K., C. I. Meng, A. T. Lui, P. T. Newell, and S. Wing (2002), Magnetic dipolarization with substorm expansion onset, *Journal of Geophysical Research: Space Physics*, *107*(A7), 23–1, doi:10.1029/2001JA000179. 18

Lu, G. (2017), Large Scale High-Latitude Ionospheric Electrodynamic Fields and Currents, *Space Science Reviews*, *206*(1-4), 431–450, doi:10.1007/S11214-016-0269-9/FIGURES/9. 40

Lühr, H., G. N. Kervalishvili, C. Stolle, J. Rauberg, and I. Michaelis (2019), Average Characteristics of Low-Latitude Interhemispheric and F Region Dynamo Currents De-

duced From the Swarm Satellite Constellation, *Journal of Geophysical Research: Space Physics*, *124*(12), 10,631–10,644, doi:10.1029/2019JA027419. 29

Lysak, R. L., and Y. Song (2006), Magnetosphere–ionosphere coupling by Alfvén waves: Beyond current continuity, *Advances in Space Research*, *38*(8), 1713–1719, doi:10.1016/J.ASR.2005.08.038. 17

Masters, A., M. F. Thomsen, S. V. Badman, C. S. Arridge, D. T. Young, A. J. Coates, and M. K. Dougherty (2011), Supercorotating return flow from reconnection in Saturn's magnetotail, *Geophysical Research Letters*, *38*(3), doi:10.1029/2010GL046149. 14

Matsui, H., J. M. Quinn, R. B. Torbert, V. K. Jordanova, W. Baumjohann, P. A. Puhl-Quinn, and G. Paschmann (2003), Electric field measurements in the inner magnetosphere by Cluster EDI, *Journal of Geophysical Research: Space Physics*, *108*(A9), doi:10.1029/2003JA009913. 14

Matsui, H., V. K. Jordanova, J. M. Quinn, R. B. Torbert, and G. Paschmann (2004), Derivation of electric potential patterns in the inner magnetosphere from Cluster EDI data: Initial results, *Journal of Geophysical Research: Space Physics*, *109*(A10), doi:10.1029/2003JA010319. 30

McPherron, R. L. (1970), Growth phase of magnetospheric substorms, *Journal of Geophysical Research*, *75*(28), 5592–5599, doi:10.1029/JA075I028P05592. 18

Milan, S. E. (2015), Sun et Lumière: Solar Wind-Magnetosphere Coupling as Deduced from Ionospheric Flows and Polar Auroras, in *Magnetospheric Plasma Physics: The Impact of Jim Dungey's Research*, edited by S. W. H. Cowley FRS, D. Southwood, and S. Mitton, pp. 33–64, Springer International Publishing, Cham. 10, 11, 12

Milan, S. E., M. Lester, S. W. Cowley, K. Oksavik, M. Brittnacher, R. A. Greenwald, G. Sofko, and J. P. Villain (2003), Variations in the polar cap area during two substorm cycles, *Annales Geophysicae*, *21*(5), 1121–1140, doi:10.5194/angeo-21-1121-2003. 12

Milan, S. E., E. J. Bunce, S. W. Cowley, and C. M. Jackman (2005), Implications of rapid planetary rotation for the Dungey magnetotail of Saturn, *Journal of Geophysical Research: Space Physics*, *110*(A3), doi:10.1029/2004JA010716. 14

Milan, S. E., G. Provan, and B. Hubert (2007), Magnetic flux transport in the Dungey cycle: A survey of dayside and nightside reconnection rates, *Journal of Geophysical Research: Space Physics*, *112*(A1), 1209, doi:10.1029/2006JA011642. 18

Milan, S. E., J. S. Gosling, and B. Hubert (2012), Relationship between interplanetary parameters and the magnetopause reconnection rate quantified from observations of the expanding polar cap, *Journal of Geophysical Research: Space Physics*, *117*(A3), 3226, doi:10.1029/2011JA017082. 8

Milan, S. E., L. B. Clausen, J. C. Coxon, J. A. Carter, M. T. Walach, K. Laundal, N. Østgaard, P. Tenfjord, J. Reistad, K. Snekvik, H. Korth, and B. J. Anderson (2017), Overview of Solar Wind–Magnetosphere–Ionosphere–Atmosphere Coupling and the Generation of Magnetospheric Currents, *Space Science Reviews*, *206*(1-4), 547–573, doi:10.1007/s11214-017-0333-0. 16

Moldwin, M. B., L. Downward, H. K. Rassoul, R. Amin, and R. R. Anderson (2002), A new model of the location of the plasmapause: CRRES results, *Journal of Geophysical Research: Space Physics*, *107*(A11), 2–1, doi:10.1029/2001JA009211. 13

Moore, A. T. E., M. O. Chandler, C. R. Chappell, C. J. Pollock, J. H. Waite, G. R. Wilson, S. Quegan, and A. S. Rodger (1989), Features of Terrestrial Plasma Transport [and Discussion], *Philosophical Transactions of the Royal Society of London. Series A, Mathematical and Physical Sciences*, *328*(1598). 10

Nagatsuma, T., H. Fukunishi, H. Hayakawa, T. Mukai, and A. Matsuoka (1996), Field-aligned currents associated with Alfven waves in the poleward boundary region of the nightside auroral oval, *Journal of Geophysical Research: Space Physics*, *101*(A10), 21,715–21,729, doi:10.1029/96JA01797. 17, 23

Newell, P. T., and C. eng (1992), Mapping the dayside ionosphere to the magnetosphere according to particle precipitation characteristics, *Geophysical Research Letters*, *19*(6), 609–612, doi:10.1029/92GL00404. 20

Newell, P. T., W. J. Burke, E. R. Sánchez, C.-I. Meng, M. E. Greenspan, and C. R. Clauer (1991a), The low-latitude boundary layer and the boundary plasma sheet at low altitude: Prenoon precipitation regions and convection reversal boundaries, *Journal of Geophysical Research: Space Physics*, *96*(A12), 21,013–21,023, doi:https://doi.org/10.1029/91JA01818. 20, 22

Newell, P. T., S. Wing, C.-I. Meng, and V. Sigillito (1991b), The auroral oval position, structure, and intensity of precipitation from 1984 onward: An automated on-line data base, *Journal of Geophysical Research*, *96*(A4), 5877, doi:10.1029/90ja02450. 33

Newell, P. T., Y. I. Feldstein, Y. I. Galperin, and C.-I. Meng (1996), Morphology of nightside precipitation, *Journal of Geophysical Research: Space Physics*, *101*(A5), 10,737–10,748, doi:https://doi.org/10.1029/95JA03516. 19, 20, 27, 33

Newell, P. T., J. M. Ruohoniemi, and C. I. Meng (2004), Maps of precipitation by source region, binned by IMF, with inertial convection streamlines, *Journal of Geophysical Research: Space Physics*, *109*(A10), 1–20, doi:10.1029/2004JA010499. 12, 20

Newell, P. T., T. Sotirelis, K. Liou, C. I. Meng, and F. J. Rich (2007), A nearly universal solar wind-magnetosphere coupling function inferred from 10 magnetospheric state variables, *Journal of Geophysical Research: Space Physics*, *112*(1), 1–16, doi:10.1029/2006JA012015. 8

Newell, P. T., T. Sotirelis, and S. Wing (2009), Diffuse, monoenergetic, and broadband aurora: The global precipitation budget, *Journal of Geophysical Research: Space Physics*, *114*(9), 1–20, doi:10.1029/2009JA014326. 22, 23, 27

Newell, P. T., A. R. Lee, K. Liou, S. I. Ohtani, T. Sotirelis, and S. Wing (2010), Substorm cycle dependence of various types of aurora, *Journal of Geophysical Research: Space Physics*, *115*(9), doi:10.1029/2010JA015331. 18

Newell, P. T., K. Liou, Y. Zhang, T. Sotirelis, L. J. Paxton, and E. J. Mitchell (2014), OVATION Prime-2013: Extension of auroral precipitation model to higher disturbance levels, *Space Weather*, *12*(6), 368–379, doi:10.1002/2014SW001056. 23

Ni, B., R. M. Thorne, X. Zhang, J. Bortnik, Z. Pu, L. Xie, Z. j. Hu, D. Han, R. Shi, C. Zhou, and X. Gu (2016), *Origins of the Earth's Diffuse Auroral Precipitation*, vol. 200, 205–259 pp., Springer Science+Business Media Dordrecht, doi:10.1007/s11214-016-0234-7. 23

Niu, Y. Y., X. X. Zhang, F. He, and Y. Jiang (2015), Statistical characteristics of the equatorial boundary of the nightside auroral particle precipitation, *Science China Earth Sciences*, *58*(9), 1602–1608, doi:10.1007/S11430-015-5090-X/METRICS. 33

Ohma, A., K. M. Laundal, M. Madelaire, S. M. Hatch, S. Gasparini, J. P. Reistad, S. Walker, and M. Decotte (2023), Excitation and decay of the auroral oval, *JGR: Space Physics*, doi:10.22541/essoar.169447428.84472457/v1. 2, 12, 13

Ohtani, S., and J. W. Gjerloev (2020), Is the Substorm Current Wedge an Ensemble of Wedgelets?: Revisit to Midlatitude Positive Bays, *Journal of Geophysical Research: Space Physics*, *125*(9), e2020JA027,902, doi:https://doi.org/10.1029/2020JA027902. 31

Papitashvili, N. (2005), NASA/GSFC SPDF OMNI data, *[Dataset]. OMNIWeb Plus*, doi:http://spdf.gsfc.nasa.gov/pub/data/omni/high{_}res{_}omni/. 31

Parker, E. N. (1996), The alternative paradigm for magnetospheric physics, *Journal of Geophysical Research: Space Physics*, *101*(A5), 10,587–10,625, doi:10.1029/95JA02866. 7

Paschmann, G., J. M. Quinn, R. B. Torbert, H. Vaith, C. E. Mcilwain, G. Haerendel, O. H. Bauer, T. Bauer, W. Baumjohann, W. Fillius, M. Förster, S. Frey, E. Georgescu, S. S. Kerr, C. A. Kletzing, H. Matsui, P. Puhl-Quinn, and E. C. Whipple (2001), The Electron Drift Instrument on Cluster: overview of first results, *Annales Geophysicae*, *19*, 1273–1288. 30

Paschmann, G., J. M. Quinn, R. B. Torbert, C. E. McIlwain, H. Vaith, S. Haaland, H. Matsui, C. A. Kletzing, W. Baumjohann, and G. Haerendel (2021), Results of the Electron Drift Instrument on Cluster, *Journal of Geophysical Research: Space Physics*, *126*(6), e2021JA029,313, doi:10.1029/2021JA029313. 30

Perreault, P., and S. kasofu (1978), A study of geomagnetic storms, *Geophysical Journal of the Royal Astronomical Society*, *54*(3), 547–573, doi:10.1111/J.1365-246X.1978.TB05494.X. 8

Pitkänen, T., A. Kullen, K. M. Laundal, P. Tenfjord, Q. Q. Shi, J. S. Park, M. Hamrin, A. De Spiegeleer, G. S. Chong, and A. M. Tian (2019), IMF By Influence on Magnetospheric Convection in Earth's Magnetotail Plasma Sheet, *Geophysical Research Letters*, *46*(21), 11,698–11,708, doi:10.1029/2019GL084190. 45

Quinn, J. M., G. Paschmann, R. B. Torbert, H. Vaith, C. E. Mcilwain, G. Haerendel, O. Bauer, T. M. Bauer, W. Baumjohann, W. Fillius, M. Foerster, S. Frey, E. Georgescu, S. S. Kerr, C. A. Kletzing, H. Matsui, P. Puhl-Quinn, and E. C. Whipple (2001), Annales Geophysicae Cluster EDI convection measurements across the high-latitude plasma sheet boundary at midnight, *Annales Geophysicae*, *19*, 1669–1681. 30

Rae, J., C. Forsyth, M. Dunlop, M. Palmroth, M. Lester, R. Friedel, G. Reeves, L. Kepko, L. Turc, C. Watt, W. Hajdas, T. Sarris, Y. Saito, O. Santolik, Y. Shprits, C. Wang, A. Marchaudon, M. Berthomier, O. Marghitu, B. Hubert, M. Volwerk, E. A. Kronberg, I. Mann, K. Murphy, D. Miles, Z. Yao, A. Fazakerley, J. Sandhu, H. Allison, and Q. Shi (2022), What are the fundamental modes of energy transfer and partitioning in the coupled Magnetosphere-Ionosphere system?, *Experimental Astronomy*, *54*(2-3), 391–426, doi:10.1007/S10686-022-09861-W/TABLES/1. 15

Redmon, R. J., W. K. Peterson, L. Andersson, E. A. Kihn, W. F. Denig, M. Hairston, and R. Coley (2010), Vertical thermal O+ flows at 850 km in dynamic auroral boundary coordinates, *Journal of Geophysical Research: Space Physics*, *115*(A11), doi:https://doi.org/10.1029/2010JA015589. 33

Redmon, R. J., W. F. Denig, L. M. Kilcommons, and D. J. Knipp (2017), New DMSP database of precipitating auroral electrons and ions, *Journal of Geophysical Research: Space Physics*, *122*(8), 9056–9067, doi:https://doi.org/10.1002/2016JA023339. 27

Reistad, J. P., K. M. Laundal, N. Østgaard, A. Ohma, A. G. Burrell, S. M. Hatch, S. Haaland, and E. G. Thomas (2021), Quantifying the Lobe Reconnection Rate During Dominant IMF By Periods and Different Dipole Tilt Orientations, *Journal of Geophysical Research: Space Physics*, *126*(11), e2021JA029,742, doi:10.1029/2021JA029742. 15

Richmond, A. D. (1995), Ionospheric Electrodynamics Using Magnetic Apex Coordinates., *Journal of geomagnetism and geoelectricity*, *47*(2), 191–212, doi:10.5636/jgg.47.191. 29

Richmond, A. D. (2007), Ionosphere, *Encyclopedia of Geomagnetism and Paleomagnetism*, pp. 452–454, doi:10.1007/978-1-4020-4423-6{_}159. 16

Ritter, P., H. Lühr, and J. Rauberg (2013), Determining field-aligned currents with the Swarm constellation mission, *Earth, Planets and Space*, *65*(11), 1285–1294, doi:10.5047/eps.2013.09.006. 29

Rostoker, G., S.-I. Akasofu, W. Baumjohann, Y. Kamide, and R. L. McPherron (1987), The roles of direct input of energy from the solar wind and unloading of stored magnetotail energy in driving magnetospheric substorms, *Space Science Reviews*, *46*, 93–111. 51

Sandel, B. R., J. Goldstein, D. L. Gallagher, and M. Spasojevic (2003), Extreme Ultraviolet Imager observations of the structure and dynamics of the plasmasphere, *Space Science Reviews*, *109*(1-4), 25–46, doi:10.1023/B:SPAC.0000007511.47727.5B/METRICS. 13, 14

Schunk, R., and A. Nagy (2018), *Ionospheres: physics, plasma physics, and chemistry (cambridge atmospheric and space science series); 2nd ed*, Cambridge University Press, doi:1108462103. 8, 15

Seki, K., A. Nagy, C. M. Jackman, F. Crary, D. Fontaine, P. Zarka, P. Wurz, A. Milillo, J. A. Slavin, D. C. Delcourt, M. Wiltberger, R. Ilie, X. Jia, S. A. Ledvina, M. W. Liemohn, R. W. Schunk, and B. K. Seki (), A Review of General Physical and Chemical Processes Related to Plasma Sources and Losses for Solar System Magnetospheres, *Space Science Reviews*, doi:10.1007/s11214-015-0170-y. 17

Shue, J., P. T. Newell, K. Liou, and C. Meng (2001), Influence of interplanetary magnetic field on global auroral patterns, *Journal of Geophysical Research: Space Physics*, *106*, 5913–5926, doi:doi: 10.1029/2000JA003010. 23

Siscoe, G. L., and T. S. Huang (1985), Polar cap inflation and deflation, *Journal of Geophysical Research: Space Physics*, *90*(A1), 543–547, doi:10.1029/JA090IA01P00543. 12

Slavin, J. A., M. H. Acuna, B. J. Anderson, D. N. Baker, M. Benna, S. A. Boardsen, G. Gloeckler, R. E. Gold, G. C. Ho, H. Korth, S. M. Krimigis, R. L. McNutt, J. M. Raines, M. Sarantos, D. Schriver, S. C. Solomon, P. Trávníček, and T. H. Zurbuchen (2009), MESSENGER observations of magnetic reconnection inmercury's magnetosphere, *Science*, *324*(5927), 606–610, doi:10.1126/SCIENCE.1172011/ASSET/C4316A03-7904-4A86-BB91-F08E45368249/ASSETS/GRAPHIC/324{_}606{_}F4.JPEG. 13

Sotirelis, T., P. T. Newell, and C. I. Meng (1998), Shape of the open-closed boundary of the polar cap as determined from observations of precipitating particles by up to four DMSP satellites, *Journal of Geophysical Research: Space Physics*, *103*(A1), 399–406, doi:10.1029/97JA02437. 19

Southwood, D., S. W. Cowley FRS, and S. Mitton (2015), *Magnetospheric Plasma Physics: The Impact of Jim Dungey's Research*, 1–271 pp., Springer, doi:10.1007/978-3-319-18359-6. 13

Stasiewicz, K., P. Bellan, C. Chaston, C. Kletzing, R. Lysak, J. Maggs, O. Pokhotelov, C. Seyler, P. Shukla, L. Stenflo, A. Streltsov, and J. E. Wahlund (2000), Small scale Alfvenic structure in the aurora, *Space Science Reviews*, *92*(3-4), 423–533, doi:10.1023/A:1005207202143/METRICS. 23

Thayer, J. P., and J. Semeter (2004), The convergence of magnetospheric energy flux in the polar atmosphere, *Journal of Atmospheric and Solar-Terrestrial Physics*, *66*(10), 807–824, doi:10.1016/j.jastp.2004.01.035. 2, 15, 21

Thorne, R. M., B. Ni, X. Tao, R. B. Horne, and N. P. Meredith (2010), Scattering by chorus waves as the dominant cause of diffuse auroral precipitation, *Nature*, *467*(7318), 943–946, doi:10.1038/nature09467. 22

Tsyganenko, N. A. (2002a), A model of the near magnetosphere with a dawn-dusk asymmetry 1. Mathematical structure, *Journal of Geophysical Research: Space Physics*, *107*(A8), 12–1, doi:10.1029/2001JA000219. 30, 41

Tsyganenko, N. A. (2002b), A model of the near magnetosphere with a dawn-dusk asymmetry 2. Parameterization and fitting to observations, *Journal of Geophysical Research: Space Physics*, *107*(A8), 10–1, doi:10.1029/2001JA000220. 30, 41

Vasyli, V. M. (2010), Physics of Magnetospheric Variability, *Space Sci Rev*, doi:10.1007/s11214-010-9696-1. 7, 21

Vasyli, V. M. (2012), The physical basis of ionospheric electrodynamics, *Annales Geophysicae*, *30*, 357–369, doi:10.5194/angeo-30-357-2012. 2

Vasyliunas, V. M. (1983), Plasma distribution and flow, *Physics of the Jovian Magnetosphere*, pp. 395–453, doi:10.1017/CBO9780511564574.013. 13, 14

Vogt, M. F., J. E. Connerney, G. A. DiBraccio, R. J. Wilson, M. F. Thomsen, R. W. Ebert, G. B. Clark, C. Paranicas, W. S. Kurth, F. Allegrini, P. W. Valek, and S. J. Bolton (2020), Magnetotail Reconnection at Jupiter: A Survey of Juno Magnetic Field Observations, *Journal of Geophysical Research: Space Physics*, *125*(3), doi:10.1029/2019JA027486. 13

Wanliss, J. A., and K. M. Showalter (2006), High-resolution global storm index: Dst versus SYM-H, *Journal of Geophysical Research: Space Physics*, *111*(A2), 2202, doi:10.1029/2005JA011034. 31

Wu, J., M. S. Bryant, C. G. Ridley, Y. Shen, L. Yang, L. B. Clausen, K. A. McWilliams, K. R. Murphy, I. R. Mann, L. G. Ozeke, H. Korth, B. J. Anderson, and C. L. Waters (2017), A comparison of small-scale magnetic fluctuations in the Region 1 and 2 field-aligned current systems, *Journal of Geophysical Research: Space Physics*, *122*(3), 3277–3290, doi:10.1002/2016JA023453. 23

Wu, J., D. J. Knudsen, D. M. Gillies, and J. K. Burchill (2020), Swarm Survey of Alfvénic Fluctuations and Their Relation to Nightside Field-Aligned Current and Auroral Arc Systems, *Journal of Geophysical Research: Space Physics*, *125*(3), 1–19, doi:10.1029/2019JA027220. 23, 29

Wygant, J. R., R. B. Torbert, and F. S. Mozer (1983), Comparison of S3-3 polar cap potential drops with the interplanetary magnetic field and models of magnetopause reconnection, *Journal of Geophysical Research: Space Physics*, *88*(A7), 5727–5735, doi:10.1029/JA088IA07P05727. 8

Xiong, C., and H. Lühr (2014), An empirical model of the auroral oval derived from CHAMP field-aligned current signatures - Part 2, *Annales Geophysicae*, *32*(6), 623–631, doi:10.5194/angeo-32-623-2014. 23

Xiong, C., H. Lühr, H. Wang, and M. G. Johnsen (2014), Determining the boundaries of the auroral oval from CHAMP field-aligned current signatures – Part 1, *Annales Geophysicae*, *32*(6), 609–622, doi:10.5194/angeo-32-609-2014. 16, 23, 44

Xiong, C., C. Stolle, P. Alken, and J. Rauberg (2020), Relationship between large-scale ionospheric field-aligned currents and electron/ion precipitations: DMSP observations, *Earth, Planets and Space*, *72*(1), doi:10.1186/s40623-020-01286-z. 23

Xu, Y., R. L. Guo, Z. H. Yao, D. X. Pan, W. R. Dunn, S. Y. Ye, B. Zhang, Y. X. Sun, Y. Wei, and A. J. Coates (2021), Properties of Plasmoids Observed in Saturn's Dayside and Nightside Magnetodisc, *Geophysical Research Letters*, *48*(24), doi:10.1029/2021GL096765. 13

Zhang, B., P. A. Delamere, Z. Yao, B. Bonfond, D. Lin, K. A. Sorathia, O. J. Brambles, W. Lotko, J. S. Garretson, V. G. Merkin, D. Grodent, W. R. Dunn, and J. G. Lyon (2021), How Jupiter's unusual magnetospheric topology structures its aurora, *Science Advances*, *7*(15), 1–7, doi:10.1126/SCIADV.ABD1204. 25

Zmuda, A. (2012), The auroral oval, *Auroral Phenomenology and Magnetospheric Processes: Earth and Other Planets*, pp. 80–83. 2

Scientific results

Paper I

Auroral Oval Morphology: Dawn-Dusk Asymmetry Partially Induced by Earth's Rotation

Margot Decotte, Karl M. Laundal, Spencer M. Hatch, Jone P. Reistad
Journal of Geophysical Research: Space Physics, **128/3** (2023)
doi: 10.1029/2023JA031345

Check for updates

JGR Space Physics

RESEARCH ARTICLE
10.1029/2023JA031345

Auroral Oval Morphology: Dawn-Dusk Asymmetry Partially Induced by Earth's Rotation

Margot Decotte[1], Karl M. Laundal[1], Spencer M. Hatch[1], and Jone P. Reistad[1]

[1]Department of Physics and Technology, Birkeland Centre for Space Science, University of Bergen, Bergen, Norway

Key Points:

- The auroral occurrence probability (AOP) is derived from Defense Meteorological Satellite Program/Special Sensor J measurements for investigating the auroral oval shape and extent
- The distribution of AOP is persistently larger at dawn than at dusk, regardless of external conditions
- A simple model of plasma sheet magnetic flux indicates that Earth's rotation may contribute to the observed dawn-dusk asymmetry

Correspondence to:

M. Decotte,
margot.decotte@uib.no

Citation:

Decotte, M., Laundal, K. M., Hatch, S. M., & Reistad, J. P. (2023). Auroral oval morphology: Dawn-dusk asymmetry partially induced by Earth's rotation. *Journal of Geophysical Research: Space Physics*, *128*, e2023JA031345. https://doi.org/10.1029/2023JA031345

Received 24 JAN 2023
Accepted 26 MAY 2023

Author Contributions:

Conceptualization: Margot Decotte, Karl M. Laundal, Spencer M. Hatch, Jone P. Reistad
Formal analysis: Margot Decotte
Funding acquisition: Karl M. Laundal
Investigation: Margot Decotte
Methodology: Margot Decotte, Karl M. Laundal, Spencer M. Hatch, Jone P. Reistad
Project Administration: Karl M. Laundal
Supervision: Karl M. Laundal, Spencer M. Hatch, Jone P. Reistad
Writing – original draft: Margot Decotte
Writing – review & editing: Margot Decotte, Karl M. Laundal, Spencer M. Hatch, Jone P. Reistad

© 2023. American Geophysical Union. All Rights Reserved.

Abstract The auroral oval morphology has been investigated in previous studies presenting maps of average auroral precipitation. However, such distributions tend to emphasize auroral intensity rather than the actual extent of the auroral oval. We develop a statistical method to characterize the auroral oval morphology by using 20 years of electron energy flux measurements from the Defense Meteorological Satellite Program/Special Sensor J (DMSP/SSJ); instead of relying on auroral oval boundaries, we derive the probability of observing aurora from a threshold of 2.10^9 eV/cm^2/s/sr above which the total energy flux of electrons (in the energy range 1–30 keV) is defined as aurora. We then investigate the auroral occurrence probability (AOP) in the magnetic latitude-magnetic local time (MLat-MLT) sectors covered by DMSP for various conditions related to geomagnetic activity. Regardless of those conditions, the AOP distributions reveal a width asymmetry with a wider dawn-to-noon sector (06–12 MLT) compared to the dusk-to-midnight sector (18–24 MLT), the dawn preference getting even more pronounced as the geomagnetic activity decreases. In the context of an open magnetosphere, we investigate the relation between the observed extent asymmetry in the auroral oval and the magnetospheric plasma convection. Representing the plasma sheet magnetic flux as a one-dimensional fluid subject to production on the nightside (closing of flux via reconnection) and loss on the dayside (opening of flux), we highlight similarities with the AOP in terms of MLT asymmetries. Finally, making use of this fluid model, we demonstrate that the corotation influence on the plasma convection pattern is consistent with the dawn-dusk asymmetry observed in the AOP distributions.

Plain Language Summary As an indirect consequence of the magnetic interaction between solar wind and Earth, protons and electrons precipitate into the ionized upper atmosphere (ionosphere) at high latitudes. These charged particles can excite atmospheric atoms at approximately 100–200 km altitude, which in turn potentially emit photons in the visible light spectrum during relaxation; this is what we call aurora. However, instruments aboard satellites crossing the polar regions, where aurora take place, can measure particles that will not necessarily result in sharp, visible aurora from the ground. This diffuse aurora represents the largest part of the total auroral energy deposited into the ionosphere. We show that the probability to measure this type of aurora is close to one within an oval-shaped region (auroral oval) around each pole, at all local times (including daytime), independently of geomagnetic conditions. We find a systematic pattern in the statistical extent of the diffuse auroral oval depending on local time, with a larger oval in the dawn region, compared to dusk. We aim at understanding the auroral oval morphology in terms of large-scale magnetospheric plasma dynamics, also including the Earth's rotation influence.

1. Introduction

Since the first reported scientific observations of auroras (Tromholt, 1882), there have been many auroral studies whose observational data from all-sky cameras resulted in the establishment of the auroral oval concept by Feldstein in the 1960s (e.g., review by Y. Feldstein (2016)). Since then, the auroral oval morphology has been investigated in great detail and discussed in connection with variations in the geomagnetic activity (e.g., Y. I. Feldstein, 1964; Feldstein & Starkov, 1967; Holzworth & Meng, 1975). It is now broadly accepted that the region where auroras occur most frequently is an approximately oval-shaped Sun-fixed zone located at high latitudes around the geomagnetic pole; its exact position depending on the solar-terrestrial physics.

Dungey (1961) was the first to put forward the concept of an open magnetosphere to study the interactions between solar wind, magnetosphere, and ionosphere. It has since been extensively demonstrated that the dynamics of the magnetosphere-ionosphere system is controlled by the convection of plasma and magnetic flux (Moore et al., 1989), with the direction and magnitude of the interplanetary magnetic field (IMF) playing a dominant role

21699402, 2023, 6, Downloaded from https://agupubs.onlinelibrary.wiley.com/doi/10.1029/2023JA031345 by UNIVERSITY OF BERGEN, Wiley Online Library on [24/01/2024]. See the Terms and Conditions (https://onlinelibrary.wiley.com/terms-and-conditions) on Wiley Online Library for rules of use; OA articles are governed by the applicable Creative Commons License

(Cowley, 1981). Cowley and Lockwood (1992) later came up with the expanding-contracting polar cap (ECPC) paradigm to describe the ionospheric convection in this context. The ECPC model predicts how the size of the polar cap, which is delimited by the open-closed boundary (OCB), depends on the amount of open magnetic flux in the magnetotail lobes which is in turn controlled by the magnetic reconnection rate. Because of its crucial role in the solar wind-magnetosphere-ionosphere coupling, the OCB has been widely studied over the last decades. The OCB location dependence on season and IMF orientation (Laundal et al., 2010), the derivation of the OCB location from the region 1 to region 2 field-aligned currents boundary (Burrell et al., 2020), and OCB location variations during substorm cycle (Milan et al., 2003) are among such studies. It is now generally accepted that the poleward boundary of the auroral oval and the OCB behaviors and locations are so closely related that they describe the same physical limit (Chisham et al., 2022). This can be seen for instance in the maps of the ionospheric precipitation regions with superposed convection streamlines presented by Newell et al. (2004).

On the other hand, much less is known about how the auroral oval's equatorward boundary behaves in the context of the ECPC paradigm. That there is currently no model or standard technique for predicting where exactly the equatorward boundary lies indicates that what controls the auroral oval spatial distribution is still not fully understood. Furthermore, existing statistical models of the aurora usually concentrate on the average energy flux or brightness of auroral precipitation rather than the extent of the auroral oval (Dombeck et al., 2018; Newell et al., 2009, 2014; Shue et al., 2001). Such models are well suited to explain the statistical behavior of accelerated aurora, which is controlled by kinetic processes such as particle drifts, particle acceleration in the auroral region and wave-particle interactions (Coumans et al., 2002; Newell et al., 2009; Ni et al., 2016). However, these studies give less attention to regions of weak and/or diffuse auroral precipitation. Yet, the diffuse precipitation, caused by electrons originating in the plasma sheet, represents the largest contribution to the total auroral energy precipitating into the ionosphere (Khazanov & Glocer, 2020).

In this study, we use precipitation data from the Defense Meteorological Satellite Program (DMSP), as previously done by Kilcommons et al. (2017) who implemented an auroral boundary identification algorithm to find the auroral oval limits. Here, we instead investigate the auroral occurrence probability (AOP), which allows for including both high and low energy precipitation in our statistics, and we expand the ECPC concept to treat the auroral oval as a mapping of a magnetospheric plasma region to garner new insight of the auroral oval spatial span. As we seek to understand the dominant processes involved in shaping the aurora, we explore the resulting auroral occurrence distributions as a function of external conditions such as geomagnetic activity and substorm phase.

In Section 2, we present the databases used to achieve our study; these include precipitation data as the core data, solar wind magnetic field and plasma data, as well as substorm epochs. In Section 3 we describe our methodology for deriving the AOP from the electron energy flux. In Section 4 we compare the AOP with the average energy flux. We also show maps and magnetic local time (MLT) profiles of the AOP for separate IMF and substorm epoch conditions, as well as for different auroral detection thresholds, and we emphasize an observed recurrent pattern. In Section 5 we provide and discuss a possible interpretation for our observations given a fluid framework in which the auroral oval maps to the plasma sheet magnetic flux, which is in turn influenced by the Earth's rotation. Finally, in Section 6 we summarize the methodology we apply for modeling the auroral oval extent, as well as the main results of this study. A brief statement of future possible work is also included.

2. Data

The database we use comprises about a billion individual electron precipitation spectra together with the corresponding solar wind and geomagnetic conditions. Since this constitutes too much data to fit in memory with standard Python libraries, we use the Vaex library (Breddels & Veljanoski, 2018) to perform our analysis. This library enables fast statistical analyses of the auroral oval morphology based on various data selection criteria. The different sources of data are described in the following subsections.

2.1. DMSP Particle Data Set

Our methodology relies on energy flux measurements of auroral electrons provided by the US Defense Meteorological Satellite Program (DMSP). The DMSP fleet consists of several low Earth-orbiting satellites at altitudes of approximately 830–850 km that are in Sun-synchronous (i.e., fixed in local time, see subsection 3.1), three-axis

21699402, 2023, 6, Downloaded from https://agupubs.onlinelibrary.wiley.com/doi/10.1029/2023JA031345 by UNIVERSITY OF BERGEN, Wiley Online Library on [24/01/2024]. See the Terms and Conditions (https://onlinelibrary.wiley.com/terms-and-conditions) on Wiley Online Library for rules of use; OA articles are governed by the applicable Creative Commons License

stabilized and nearly circular polar orbits approximately in the dawn-dusk meridian plane, with a periodicity of 101 min and an orbital inclination of 98.7°–98.9°. For the purpose of our statistical analysis we use most of the CDAWeb database described in Redmon et al. (2017), that is, a total of 21 years of observations, within the 2000–2014 time period. All measurements are made by the SSJ/4 and SSJ/5 (Special Sensor J) electrostatic analyzer instruments on board nine of the DMSP satellites. By pointing within the downward atmospheric loss cone at auroral latitudes, these detectors measure precipitating particles between 30 eV and 30 keV using 20 energy channels, thus providing a fairly complete energy spectrum of the particles that cause the aurora at 1-s cadence. We provide the spacecraft location in modified Apex coordinates (Richmond, 1995).

2.2. High Resolution OMNI Database

To investigate the solar wind–auroral precipitation coupling, the DMSP precipitating particle data are combined with the multi-source OMNI data set of solar wind magnetic field and plasma parameters compiled from observations made by IMP-8, ACE, Wind, ISEE-3, and Geotail spacecrafts (Papitashvili et al., 2014). The best near-Earth estimates of solar wind properties are obtained by time-shifting upstream observations to represent the conditions at the nose of the Earth's bow shock (King & Papitashvili, 2005). Hence, there are non-negligible uncertainties in the solar wind parameters affecting the magnetosphere (Di Matteo & Sivadas, 2022). We use IMF data and geomagnetic indices provided by the 1-min resolution OMNIWeb database, between 2000 and 2014. From the OMNI database, we use the y (dawn-dusk) and z (north-south) components of the interplanetary magnetic field given in geocentric solar magnetospheric (GSM) coordinates, the ring current SYM-H index, and the auroral electrojet index AL. To temporally align this data of 1-min resolution with the 1-s resolution DMSP data set, we associate each DMSP data point with the OMNI data point from the nearest preceding minute.

2.3. Isolated Substorm Onset List

To determine how the auroral precipitation varies throughout the substorm cycle, we combine the DMSP observations with 13,000 substorm onsets identified from SuperMAG-derived auroral electrojet (SML) indices (Ohtani & Gjerloev, 2020). From the Ohtani and Gjerloev original substorm list, we exclude onsets distinct by less than 2 hr from the nearest onset, to ensure that our analysis focus on isolated substorms. This way, we aim at observing a clean response of the AOP to substorm epochs, without any ambiguity on the possible influence of already ongoing activity. Since isolated substorms tend to be weaker than "recurrent" substorms (Rodger et al., 2016), our statistics may slightly underestimate typical substorm effects. We perform a superposed epoch analysis using all the DMSP data described in Section 2.1.

3. Methodology—Auroral Occurrence Probability

In this section, we introduce the concept of AOP that our study relies on. In particular, we show how this quantity might be more appropriate, given the DMSP orbits, than using auroral boundary identification for our investigation of the extent of the auroral region. We also describe the relevance to our purposes of the choice of parameters (energy range and threshold for aurora detection) on which the AOP is based.

3.1. Local Time Orbital Bias Introduced by Sun-Synchronous Satellites

Each DMSP spacecraft is synchronised such that its orbit is always at the same fixed position relative to the Sun (Sun-synchronous orbit), that is, the spacecraft always visits approximately the same latitude at the same local time; thus the distribution of in situ measurements made by a Sun-synchronous satellite is biased toward particular local times. In this paragraph, we briefly demonstrate how such data can produce a statistically biased estimate of the auroral boundaries. While we point to the DMSP satellites and more generally to satellites in Sun-synchronous orbit, the issue described here remains true on short time periods for non-Sun-synchronous satellites, as long as such a satellite stays in the same local time plane during that time.

Figure 1 shows the simulated trajectory (gray lines in left panels) of a synthetic Sun-synchronous satellite over a period of 1 year in the Northern (top left panel) and Southern (bottom left panel) Hemispheres. The orbital plane of the satellite sweeps over a wide band in magnetic coordinates due to the offset between magnetic and geographic poles—this offset being larger in the Southern Hemisphere. We define an ideal auroral boundary

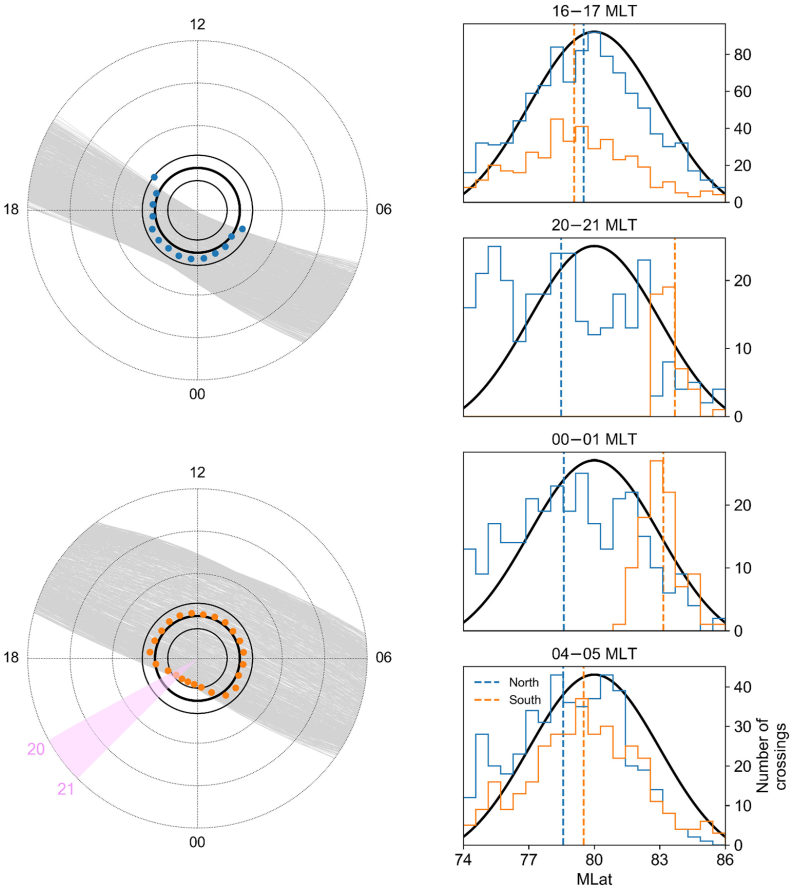

Figure 1. Left: Simulated synthetic Sun-synchronous orbits (gray) during 1 year for the Northern (top) and Southern (bottom) Hemispheres. The latitudinal range spans 50°–90° MLat. The circular black lines indicate the statistical location of the theoretical true auroral boundary, which is modeled as a Gaussian random variable having a mean of 80° MLat (thick line) and a standard deviation of 3° (thin lines at 80° ± 3° MLat). The colored dots indicate the average position of the measured boundary crossings in each covered magnetic local time (MLT) sector. Right: Gaussian and measured distributions of boundary crossings in the Northern (blue) and Southern (orange) Hemispheres for four MLT sectors spanning 1 hr. The dashed vertical line marks the average latitude of the distribution of sampled boundary crossings in each hemisphere.

represented by a Gaussian distribution centered at 80° magnetic latitude (MLat) (thick black line), with a standard deviation of 3° (thin black lines). For each simulated satellite crossing of the polar region, the MLat location of the auroral boundary is sampled from this Gaussian distribution. The resulting MLat distribution of measured boundary crossings can be derived at each MLT for the Northern (blue) and the Southern (orange) Hemispheres, as shown for four different MLT sectors spanning 1 hour at right in Figure 1, together with the correct distribution (in black). The average MLat location of the sampled boundary is shown as a colored dot at each MLT (left panels) and as a vertical colored dashed line for the four 1 hr-MLT sectors (right panels), in both hemispheres. Since the satellite does not measure the full distribution in local time sectors poorly covered by the satellite orbit, the sampled distribution is deformed compared to the correct distribution and, as a consequence, the mean position of the modeled boundary is biased and does not match with the Gaussian's peak at 80°. An obvious example of this is the 20–21 MLT sector in the Southern Hemisphere (highlighted pink region) in which the statistically identified boundary lies several degrees above the actual mean magnetic latitude of the boundary.

21699402, 2023, 6, Downloaded from https://agupubs.onlinelibrary.wiley.com/doi/10.1029/2023JA031345 by UNIVERSITY OF BERGEN, Wiley Online Library on [24/01/2024]. See the Terms and Conditions (https://onlinelibrary.wiley.com/terms-and-conditions) on Wiley Online Library for rules of use; OA articles are governed by the applicable Creative Commons License

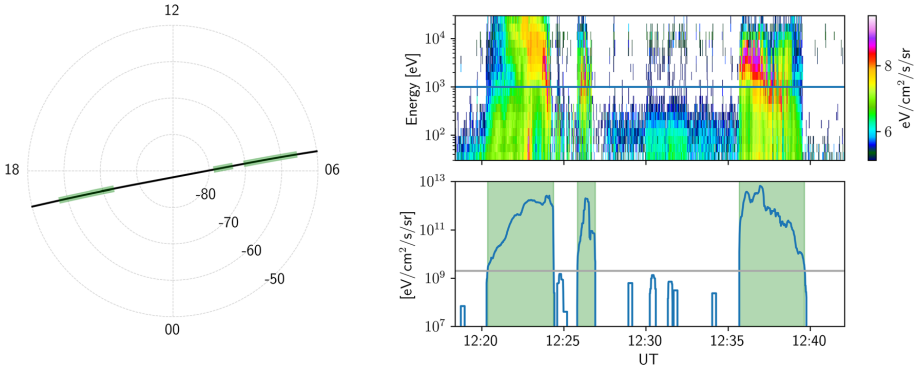

Figure 2. Example auroral identification based on electron precipitation data from one southern polar region crossing by Defense Meteorological Satellite Program (DMSP) F16 on 29 May 2010. Left: The spacecraft orbit is shown in black as Apex magnetic latitude and magnetic local time. Right, top panel: The electron energy spectrogram with the channel energy of the 19 DMSP Special Sensor J channels on the *y*-axis and time on the *x*-axis. The blue horizontal line corresponds to an energy of 1 keV. Bottom panel: The electron energy flux integrated over all of the channels with center energies of at least 1 keV is shown in blue, while the gray horizontal line shows our threshold for auroral detection ($2 \cdot 10^9$ eV/cm^2/s/sr). In this example, the auroral identification algorithm detects three auroral regions, shown shaded in green. The identified auroral regions are also highlighted in green along the satellite orbit (left).

We emphasize that although the local time bias is reduced when using multiple satellite orbits, it persists as long as the MLT coverage is not sufficient. While we combine data from several DMSP satellites in our analysis, we will show in Section 4.2 that some MLT sectors are still poorly covered (see Figure 4); we thus expect the local time bias to be significant in these regions.

Based on these results we conclude that using the Kilcommons et al. (2017) auroral boundary data set derived from the DMSP/SSJ precipitation data would lead to a mistaken analysis in our study of the extent of the auroral oval. We nevertheless base the model of auroral oval presented in this paper on the concept of AOP which relies on several aspects of the work of Kilcommons et al. (2017), as we now discuss in the succeeding subsections.

3.2. Energy Range and Threshold for Detection of Aurora

At the origin of the AOP concept is a binary time series that indicates if a particular loss cone electron energy flux spectrum measured by the DMSP/SSJ instrument constitutes an observation of auroral precipitation. Such binary information is produced by following the method of identification of candidate auroral regions presented in Kilcommons et al. (2017). An example of aurora detection is illustrated in Figure 2, using DMSP/SSJ electron precipitation data from a single satellite pass. The corresponding electron energy spectrogram is shown in the top panel at right. We adopt Kilcommons et al. (2017) choice to classify electron energy spectra as either "aurora" or "non-aurora" based on examination of electron precipitation of at least 1 keV (horizontal blue line). We use the Hardy et al. (1985) technique to integrate the differential electron energy fluxes from the nine highest energy channels of the SSJ instrument, which cover 1.392–30 keV (Redmon et al., 2017). The bottom panel at right in Figure 2 shows the resulting integrated energy flux (in blue) and the threshold of $2 \cdot 10^9$ eV/cm^2/s/sr used for aurora detection (horizontal gray line). Eventually, precipitating electron fluxes exceeding this threshold are deemed "aurora" (shown shaded in green), and "not aurora" otherwise, such that we end up with a Boolean (True/False) value for every DMSP/SSJ electron energy flux data point. Our choice of threshold is similar to the threshold used by Kilcommons et al. (2017) ($1 \cdot 10^9$ eV/cm^2/s/sr), which has been shown to be suitable for the detection of auroral regions that map to the central or boundary plasma sheet (Newell et al., 1996).

For comparison, by assuming an isotropic flux over the loss cone and a solid angle of π, our threshold is equivalently $5 \cdot 10^{-3}$ mW/m^2 which is more than two orders of magnitude below the 1 mW/m^2 auroral brightness that Keiling et al. (2003) define as visible aurora. Thus our threshold for identifying aurora should not necessarily be construed to mean "visible aurora." Additional discussion on our choice of a threshold value, as well as its influence on the auroral oval model that we present, is located in Section 4.3.

21699402, 2023, 6, Downloaded from https://agupubs.onlinelibrary.wiley.com/doi/10.1029/2023JA031345 by UNIVERSITY OF BERGEN, Wiley Online Library on [24/01/2024]. See the Terms and Conditions (https://onlinelibrary.wiley.com/terms-and-conditions) on Wiley Online Library for rules of use; OA articles are governed by the applicable Creative Commons License

21699402, 2023, 6, Downloaded from https://agupubs.onlinelibrary.wiley.com/doi/10.1029/2023JA031345 by UNIVERSITY OF BERGEN, Wiley Online Library on [24/01/2024]. See the Terms and Conditions (https://onlinelibrary.wiley.com/terms-and-conditions) on Wiley Online Library for rules of use; OA articles are governed by the applicable Creative Commons License

3.3. Auroral Occurrence Probability

Once the binary data is generated, each DMSP/SSJ data point is binned into an approximately equal area grid covering 50°–90° MLat with rings of width 1° MLat divided into a varying number of cells, with 2 cells in the most poleward circle (89°−90°) and 68 cells in the most equatorward circle. Bins with less than 200 measurements are discarded to ensure a robust statistical analysis. In each of the remaining MLat-MLT bins, we calculate the probability of observing aurora by dividing the sum of all observations identified as aurora by the total number of measurements. In order to have a suitable way to visualize the auroral oval morphology, especially when it becomes asymmetric, the resulting probabilities are processed in two ways: (a) we display the AOP and the underlying grid on a polar map, and (b) we derive the MLT variation of the AOP. Such an MLT profile is derived by interpolating the gridded probabilities to an MLT-MLat grid with 0.5° resolution in MLat and 8 min resolution in MLT and then averaging the gridded value over latitude. From now on, the resulting quantity is referred to as the 1D-AOP. We point out that, unlike the AOP, the 1D-AOP is no longer a probability, and its unit is arbitrary; nonetheless, it can still be used to study the variation of the probability as a function of MLT. We will see that the auroral occurrence oval exhibits asymmetries that are often more easily detected by way of the 1D-AOP than by looking at the AOP maps, especially when comparing distributions for different conditions.

In addition to eliminating the local time bias present in statistics of auroral boundaries identified from in situ Sun-synchronous satellite measurements (Section 3.1), the AOP allows us to use much more of the entire set of DMSP/SSJ measurements, as we do not lose polar passes for which both the poleward and equatorward boundaries cannot be identified. The AOP moreover includes observations of no or low precipitation rather than discarding the information that they provide. In other words, the AOP makes use of all observations made during every DMSP pass within the auroral zone. We believe that such a data set is ideally suited for investigating the auroral oval morphology.

4. Results

In this section, we first review the similarities and differences between the AOP and the average energy flux. Then we look exclusively at the AOP and we investigate further the maps and MLT profiles resulting from our data analysis. In particular, we explore the response of the auroral occurrence oval morphology to various parameters within our global data set.

4.1. Comparison Between the AOP and the Average Energy Flux

As stated in the introduction, large-scale, long-term studies of the auroral oval have tended to focus on parameters such as the average energy flux. The MLat-MLT distribution of such a quantity mainly reflects high-energy precipitation as it gives more weight to the MLat-MLT bins with high energy flux values over those with lower energy flux. Conversely, the distribution of AOP is based on equally weighted observations within each MLat-MLT bin and is thus better suited to characterize to what degree each bin experiences precipitation.

Figure 3 shows maps of AOP (left) and mean energy flux (right) in the Southern Hemisphere, as derived from our data set for geomagnetically quiet (B_z positive, top) and active (B_z negative, bottom) periods. The post-noon and post-midnight data gaps are the result of the incomplete coverage of these sectors due to the Sun-synchronous orbits of the DMSP spacecraft (see also Section 4.2).

It is worth mentioning that the energy flux distributions introduced here are similar to the diffuse aurora energy flux presented by Newell et al. (2009). In particular, the energy flux pattern for B_z negative is almost indistinguishable from Newell's energy flux for high solar wind driving. For B_z positive, that is, low solar wind driving, our map of energy flux and those of Newell present some differences in the location of intensity peak but are still fairly comparable. On the other hand, we do not have any reference to compare our diffuse aurora probability distributions with since Newell et al. (2009) have only derived the probabilities of observing monoenergetic and broadband aurora in their study.

The comparison between the AOP and the mean energy flux reveals that the auroral oval, as reflected in the AOP, is extended over a wider range of latitudes than the auroral oval reflected in the mean energy flux. This larger auroral oval is expected as the AOP takes into account the weak precipitation, unlike the average energy flux distribution. However, apart from the difference in width, it is apparent that the overall morphologies of the AOP

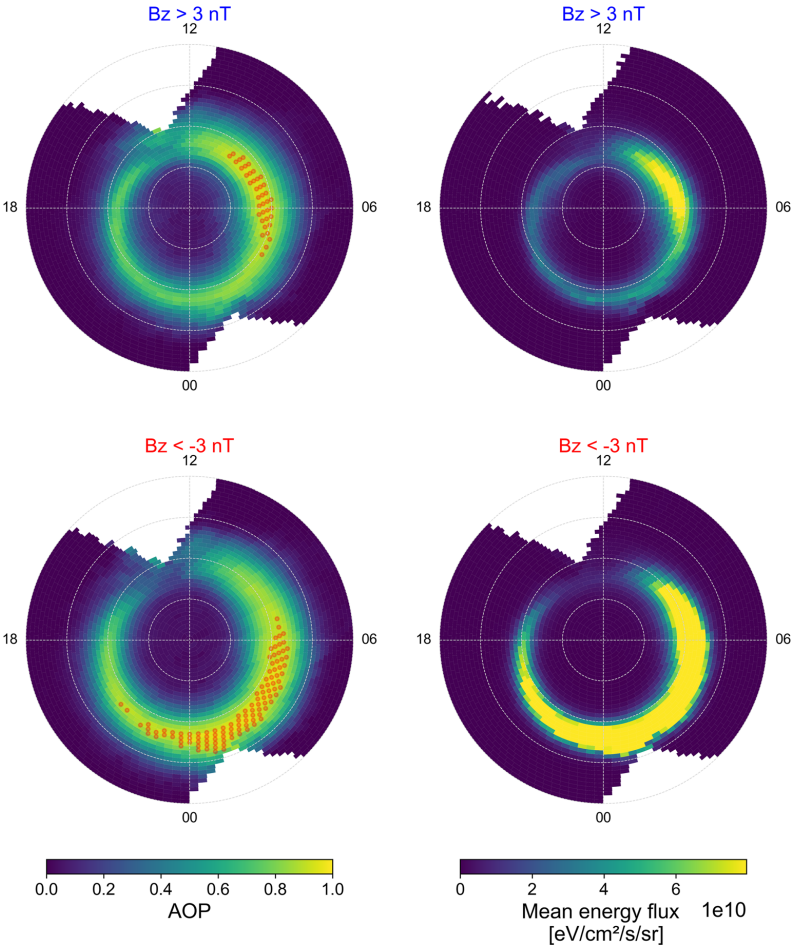

Figure 3. Distributions of auroral occurrence probability (AOP) (left) and mean energy flux (right) for B_z positive (top) and B_z negative (bottom) in the Southern Hemisphere. All distributions presented in this paper span over 50°–90° |MLat|, for all MLTs covered by the orbits of our DMSP satellite selection (see Section 2.1). The red dots on the left maps indicate bins with AOP value > 0.9 (AOP peak).

and the average energy flux are somehow equivalent. In particular, the peak of the AOP distributions (shown as red dots on the left maps), defined by AOP values exceeding 0.9, matches the regions of enhanced mean energy flux. In addition to that, both quantities exhibit a similar asymmetric pattern between dawn and dusk, more or less prominent depending on the geomagnetic conditions, but persistent anyhow. We discuss the shape and extent features of the AOP in more detail in the following section.

4.2. A Dawn-Dusk Asymmetry in the AOP

The top panel of Figure 4 shows the AOP distributions derived from the entire 20-year data set for the Northern (left) and Southern (right) Hemispheres, while the line plot in the bottom panel of Figure 4 shows the corresponding 1D-AOP as a function of MLT (gray and black for the Northern and Southern Hemispheres, respectively). The data gaps seen on the maps (and evoked in the previous section) also appear in the 1D-AOP distributions,

21699402, 2023, 6, Downloaded from https://agupubs.onlinelibrary.wiley.com/doi/10.1029/2023JA031345 by UNIVERSITY OF BERGEN, Wiley Online Library on [24/01/2024]. See the Terms and Conditions (https://onlinelibrary.wiley.com/terms-and-conditions) on Wiley Online Library for rules of use; OA articles are governed by the applicable Creative Commons License

21699402, 2023, 6, Downloaded from https://agupubs.onlinelibrary.wiley.com/doi/10.1029/2023JA031345 by UNIVERSITY OF BERGEN, Wiley Online Library on [24/01/2024]. See the Terms and Conditions (https://onlinelibrary.wiley.com/terms-and-conditions) on Wiley Online Library for rules of use; OA articles are governed by the applicable Creative Commons License

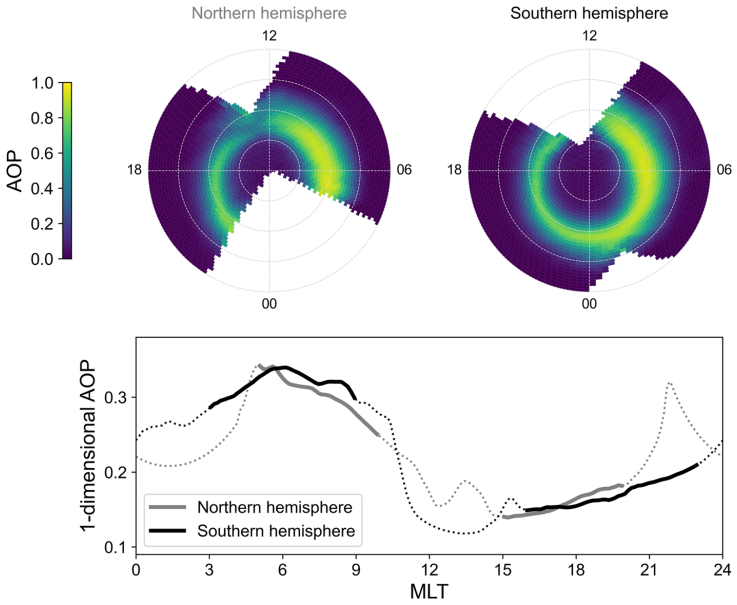

Figure 4. Top row: magnetic latitude-magnetic local time (MLat-MLT) distributions of auroral occurrence probability (AOP) for the Northern (left) and Southern (right) Hemispheres. Bottom panel: 1D-AOP as a function of MLT for the Northern (gray) and Southern (black) Hemispheres. The thick line indicates MLT regions well covered by the satellite orbits, while the thin line corresponds to MLT regions with incomplete coverage.

with dotted (thick) lines indicating MLTs where coverage is insufficient (sufficient) to derive a reliable estimate of the 1D-AOP. It can be seen that the Southern Hemisphere benefits from a better coverage than the Northern Hemisphere due to the larger offset between magnetic and geographic poles in the South. As a consequence, most of the nightside data in the following analysis comes from the Southern hemisphere with a negative tilt angle.

Beyond differences in coverage, there are no major distinctions between the distributions of AOP in the two hemispheres. This is especially clear from the MLT profiles of 1D-AOP which are likewise similar in shape, in fairly covered sectors. Furthermore, it can be seen from covered sectors that both maps exhibit a comparable variation of the AOP with MLT. In particular, the auroral occurrence oval is distinctly wider in the dawn-to-noon sector than in the dusk-to-midnight sector. This dawn-dusk asymmetry can also be seen from the 1D-AOP in both hemispheres.

From now on, considering that the AOP does not meaningfully differ between the two hemispheres, we combine measurements from both hemispheres in order to improve the spatial coverage of the auroral region. Even so, and despite an excellent coverage for most local times between 50° and 60° |MLat|, the very poorly covered postnoon and postmidnight regions below 60° |MLat| exhorts us to be careful when interpreting the upcoming results of our statistical analysis in these MLT sectors. We especially expect that the lack of coverage would affect our results when the auroral occurrence oval lies at low latitudes and/or is particularly wide. On the other hand, the regions 4–11 MLT (~dawn) and 16–23 MLT (~dusk) can be considered with confidence.

4.3. Response of the AOP to the Threshold for Aurora Detection

In Section 3.2 we have briefly introduced the choice of threshold above which integrated high-energy electron energy flux measurements made by DMSP are deemed to be aurora. Here we show how the AOP varies with the choice of threshold, and we explain our final choice in more detail.

Figure 5 shows the AOP distributions (top) and the corresponding MLT profiles of 1D-AOP (bottom), as derived from three thresholds for positive identification of aurora, within an order of magnitude around the value of

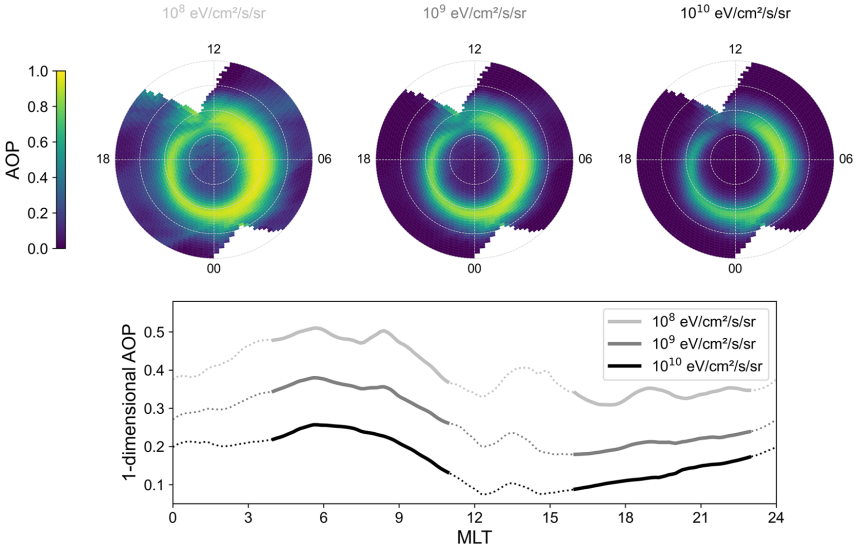

Figure 5. Auroral occurrence probability (AOP) distributions (top row) and magnetic local time profiles of 1D-AOP (bottom panel) for three different thresholds above which integrated high-energy (≥1 keV) electron energy flux is deemed to be aurora. From left to right the threshold values are respectively 10^8 eV/cm^2/s/sr (light gray), 10^9 eV/cm^2/s/sr (gray), and 10^{10} eV/cm^2/s/sr (black). The middle value is also the threshold used in the study of Kilcommons et al. (2017).

$1 \cdot 10^9$ eV/cm^2/s/sr (Kilcommons et al., 2017). The morphology of the AOP distributions is similar for all three thresholds, especially the dawn-dusk asymmetry and the overall preference for the dawn side, as already described in the previous section. However, the choice of different thresholds results in auroral occurrence ovals with varying intensities; in particular, a lower threshold for aurora detection yields a more intense auroral oval, with a higher probability of observing aurora everywhere in the auroral zone, compared to a higher threshold. In addition, a decreased threshold results in a minor poleward expansion of the auroral oval on the dusk side, together with a non-negligible widening of the auroral oval both poleward and equatorward on the dawn side, as seen from the maps. As a consequence of the heterogeneous auroral oval expansion depending on MLT sectors, the resulting asymmetry between dawn and dusk in the AOP gets larger as the threshold gets lower. The MLT profiles highlight this variation in the relative dawn-dusk asymmetry: although the overall patterns for all three thresholds are similar, the slope of the line over ∼16–23 MLT slightly increases with an increasing threshold value. We have also tested thresholds greater than $1 \cdot 10^{10}$ eV/cm^2/s/sr (not shown) and found that the dawn-dusk asymmetry in the auroral occurrence oval continues to decrease as the threshold is increased.

We conclude that the AOP spatial variation is stable with respect to the choice of integrated energy flux threshold for positive identification of aurora and that the threshold choice does not influence our study provided that it is roughly in the range of 10^8–10^{10} eV/cm^2/s/sr. However, as shown by the leftmost distribution, a threshold that is too low tends to give noisy results, even if the overall morphology of the auroral occurrence oval shape is unchanged. We therefore suggest that for a threshold to be meaningful, it likely must lie in the interval $5 \cdot 10^8$–10^{10} eV/cm^2/s/sr. We have chosen to use a threshold equal to $2 \cdot 10^9$ eV/cm^2/s/sr, as this value is very similar to the limit chosen by Kilcommons et al. (2017), and has the additional advantage to give a probability of observing aurora in the polar cap closer to zero than the $1 \cdot 10^9$ eV/cm^2/s/sr threshold.

4.4. Response of the AOP to IMF B_y

We now compare the distributions of AOP under different polarities of IMF B_y. Since we combine both hemispheres in our analysis, and since the y component of the IMF is known to affect differently the two hemispheres in terms of ionospheric electrodynamics depending on its sign (Hatch et al., 2022), here we have flipped the sign of B_y in the Southern Hemisphere such that the comparison between the two IMF polarities is valid.

21699402, 2023, 6, Downloaded from https://agupubs.onlinelibrary.wiley.com/doi/10.1029/2023JA031345 by UNIVERSITY OF BERGEN, Wiley Online Library on [24/01/2024]. See the Terms and Conditions (https://onlinelibrary.wiley.com/terms-and-conditions) on Wiley Online Library for rules of use; OA articles are governed by the applicable Creative Commons License

21699402, 2023, 6, Downloaded from https://agupubs.onlinelibrary.wiley.com/doi/10.1029/2023JA031345 by UNIVERSITY OF BERGEN, Wiley Online Library on [24/01/2024]. See the Terms and Conditions (https://onlinelibrary.wiley.com/terms-and-conditions) on Wiley Online Library for rules of use; OA articles are governed by the applicable Creative Commons License

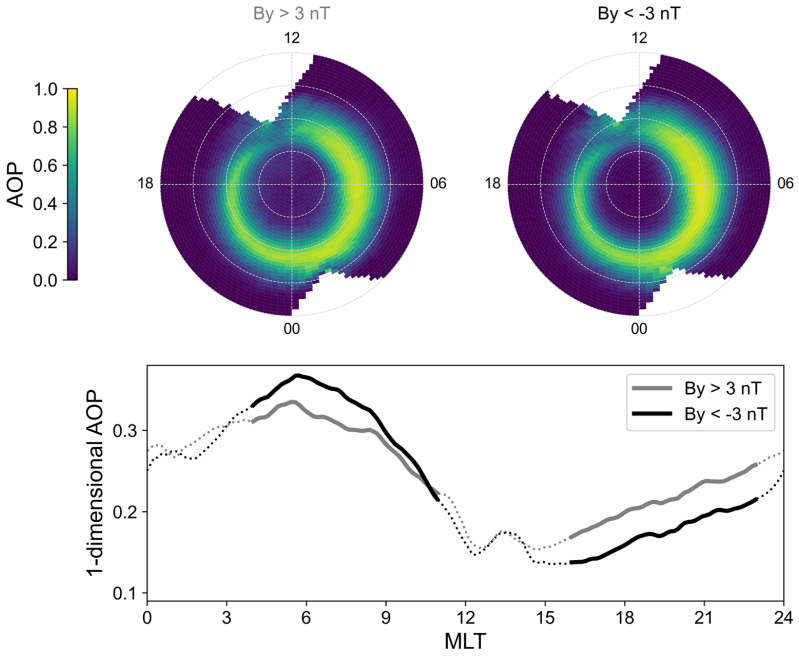

Figure 6. Auroral occurrence probability (AOP) distributions (top row) and magnetic local time profiles of 1D-AOP (bottom panel) for IMF B_y positive (left, gray) and B_y negative (right, black).

The maps in Figure 6 indicate a weak response of the AOP to the sign of B_y. In particular, both distributions vary in a similar fashion, and the usual asymmetry between the dawn and the dusk sides of the auroral oval remains prominent for both orientations of B_y. Nevertheless, the MLT variations of the 1D-AOP highlight a decrease in the dawn-dusk asymmetry for B_y positive.

4.5. Response of the AOP to Substorm Epochs

Figure 7 shows the statistical evolution of the AOP with the substorm cycle, and the corresponding MLT profiles of 1D-AOP, from 30 min before substorm onset ($t = 0$) up until 30 min after onset, separated into 15-min intervals.

We emphasize that a neat interpretation of the substorm influence is difficult when one makes use of a substorm list based on magnetometer data, as the measured geomagnetic variations most likely include the contribution of induced currents (Juusola et al., 2020). Considering solely isolated substorms, as mentioned in Section 2.3, might slightly balance this issue but also results in the exclusion of most of the intense and global events (Rodger et al., 2016). In addition to that, the AOP evolution is automatically smoothed by the choice of time periods for the superposed epoch analysis, as large time ranges mingle the substorm onset times and phases. Finally, we point out that the nightside data are mainly from the Southern Hemisphere (as mentioned in Section 4.2), while the substorms are identified in the north. For all these reasons, the substorm effect on the AOP morphology reported here could be underestimated.

In fact, the first impression from both the maps and MLT profiles is that the AOP is very stable, without any clear correlation with the substorm epoch. A closer look at the midnight region on each map allows us to spot a small widening of the auroral occurrence oval after the substorm onset ($t > 0$). As for the MLT profiles, it can be seen that the after-onset lines (red) are below the before-onset lines (blue) from 3 to 20 MLT, that is, most of the time. However, around the midnight region, which is known to be an MLT sector highly affected by substorm dynamics, the after-onset line slopes increase from 21 to 2 MLT such that the 1D-AOP reaches higher values

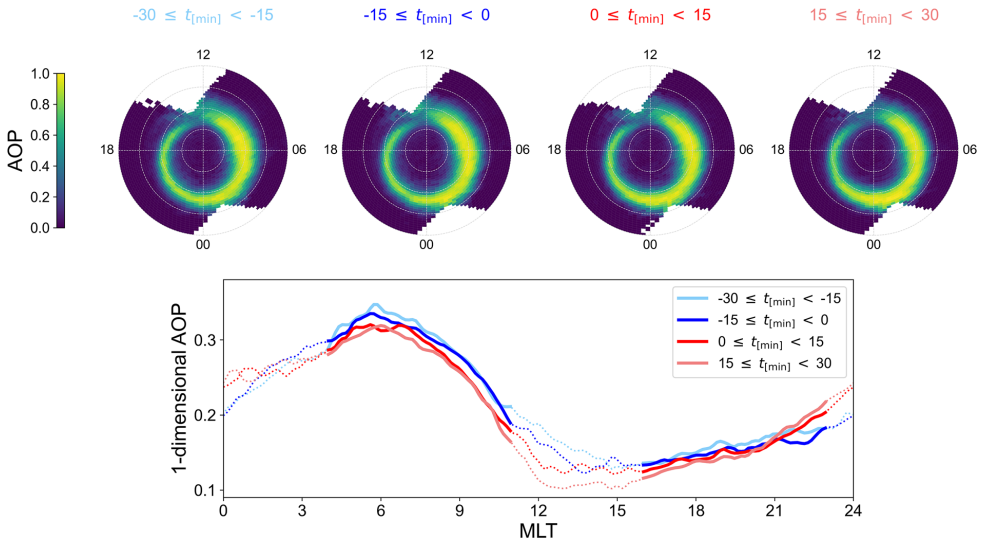

Figure 7. Auroral occurrence probability (AOP) distributions (top row) and magnetic local time profiles of 1D-AOP (bottom panel) for four different 15 min-time ranges around substorm onset. From left to right the time ranges are respectively -30 min $\leq t < -15$ min (light blue), -15 min $\leq t < 0$ min (dark blue), 0 min $\leq t < 15$ min (dark red), 15 min $\leq t < 30$ min (light red).

after substorm onset, compared to before onset. This seems to be in agreement with the increased extent of the auroral occurrence oval after onset observed on the maps. This observation is the only tangible hint that the AOP is not completely uncorrelated to substorm activity, which would be highly unexpected, but such small changes indicate nonetheless that the time scales involved in the AOP dynamics might be longer than what is captured in our substorm analysis.

4.6. Response of the AOP to the Level of Geomagnetic Activity

Here we investigate the response of the AOP to three parameters reflecting either the reconnection rate between the IMF and the magnetosphere (IMF B_z) or the intensity of geomagnetic disturbances (SYM-H and AL indices). Our aim is to make use of those parameters to emulate either a high or a low level of geomagnetic activity and study its influence on the auroral oval dawn-dusk asymmetry.

Figure 8 shows the AOP maps and MLT profiles of the 1D-AOP for the three above-mentioned parameters. For $B_z > 3$ nT, SYM-H > -10 nT and AL > -50 nT (i.e., during low geomagnetic activity, top row), the AOP distributions exhibit a clear preference for the dawn sector (5–10 MLT). The same observation can be made from the MLT profiles with the low activity line (in blue) showing a significant asymmetry between the dawn and dusk sides, with a distinct peak of the 1D-AOP in the dawn sector. On the other hand, for $B_z < -3$ nT, SYM-H < -20 nT and AL < -150 nT (i.e., during high geomagnetic activity, middle row), the AOP dawn preference remains but is less pronounced. For such conditions, the main change in the AOP is an increase in latitudinal extent on the nightside, over approximately 22–5 MLT. From the MLT profiles, the high activity line (in red) shows higher values of the 1D-AOP everywhere in the nightside sector compared to the dayside, with a minor peak in the dawn sector. This results in a less asymmetric pattern in the auroral oval for active times than for quiet times.

In summary, the behavior of the AOP and the associated MLT profiles is stable with regard to the different parameters we investigate. The AOP distributions sorted by B_z, SYM-H and AL all show: (a) an enhanced AOP on the nightside during active periods compared to periods of lower activity, (b) relatively enhanced AOP on the nightside compared to dayside during active times, and (c) a relatively enhanced AOP on the dayside compared to nightside during quiet times. These collateral changes affect the auroral oval extent asymmetry such that the dawn sector is the most prominent during quiet times, while the whole nightside region is predominant over the dayside

21699402, 2023, 6, Downloaded from https://agupubs.onlinelibrary.wiley.com/doi/10.1029/2023JA031345 by UNIVERSITY OF BERGEN, Wiley Online Library on [24/01/2024]. See the Terms and Conditions (https://onlinelibrary.wiley.com/terms-and-conditions) on Wiley Online Library for rules of use; OA articles are governed by the applicable Creative Commons License

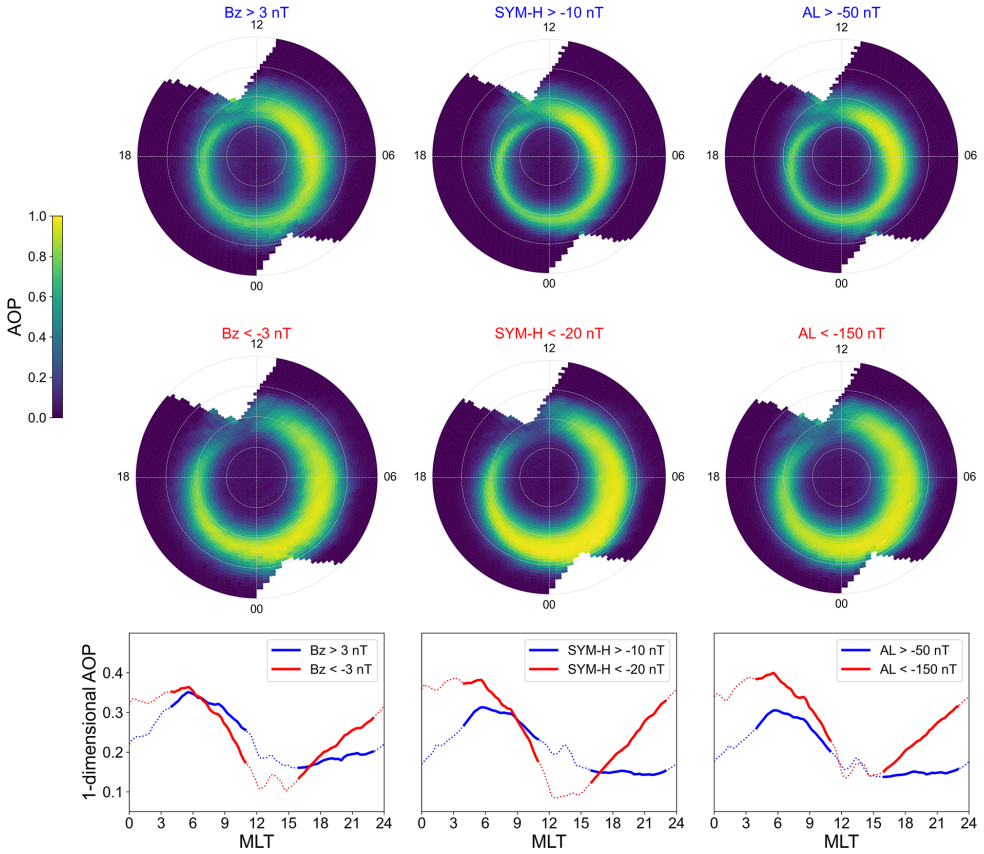

Figure 8. Auroral occurrence probability (AOP) distributions (two top rows) and magnetic local time profiles of 1D-AOP (bottom row) for low (top row, blue) and high (middle row, red) levels of geomagnetic activity, based on different geomagnetic parameters. From left to right the parameters are: IMF B_z, SYM-H index and AL index.

during active times. We conclude that the dawn preference in the auroral oval is influenced by the geomagnetic activity, with an increased dawn-dusk asymmetry as the activity decreases. We discuss this further in Section 5.

5. Discussion

We have investigated the auroral region morphology via the AOP, and have found a persistent dawn-dusk asymmetry in the auroral occurrence oval extent. Such an asymmetric pattern has been observed before in average energy flux studies (e.g., Newell et al., 2009) and explained through the scope of kinetic dynamics. In a detailed review of such studies, Ni et al. (2016) point to the formation of discrete aurora in association with electron acceleration by quasi-static electric fields and dispersive Alfvén waves on the one hand, and to the major role of various magnetospheric waves in driving the diffuse auroral precipitation on the other hand. They also stress that the predominant eastward transport of electrons, leading to a dawn-dusk asymmetry in the auroral oval morphology, is typically interpreted as a result of a combination of $\mathbf{E} \times \mathbf{B}$ and gradient drifting from the nightside plasma sheet.

However, we have shown that the AOP has some specific characteristics (in comparison with the mean energy flux) such as the substantial sensitivity to diffuse precipitation and the overall stability with respect to substorm epochs, as well as solar wind and geomagnetic conditions, suggesting a long-term, large-scale evolution of the AOP morphology. Hence, while we acknowledge the contribution and importance of the mechanisms that

21699402, 2023, 6, Downloaded from https://agupubs.onlinelibrary.wiley.com/doi/10.1029/2023JA031345 by UNIVERSITY OF BERGEN, Wiley Online Library on [24/01/2024]. See the Terms and Conditions (https://onlinelibrary.wiley.com/terms-and-conditions) on Wiley Online Library for rules of use; OA articles are governed by the applicable Creative Commons License

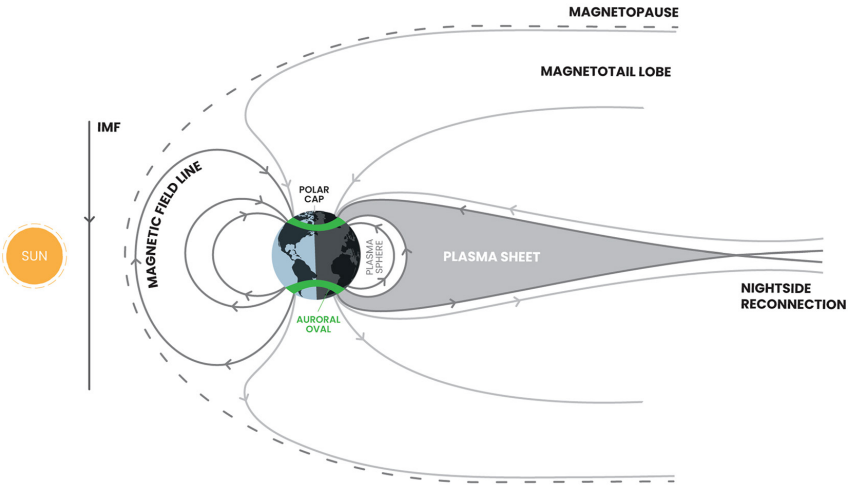

Figure 9. Schematics of the mapping between the auroral oval (in green) and the magnetospheric regions, within the global frame of the open magnetosphere produced by the Dungey cycle. Closed field lines are shown in dark gray, open field lines are in light gray. Illustration not to scale.

traditionally explain the main features of the global distribution of auroral precipitation, we suggest that the AOP is not only affected by the energetic precipitation but also reflects the magnetospheric topology. We thus propose a new interpretation of the observed asymmetry through a fluid description in which the AOP is regulated by the shape and bulk motion of the magnetospheric plasma that maps to the auroral region. This in turn is controlled by the following sequence: plasma sheet production by nightside reconnection (closing of flux), sunward transport, and then loss through dayside reconnection (opening of flux). Given our fluid description, we also suggest that the Earth's corotation, through its influence on the plasma convection pattern, may be partly responsible for the dawn-dusk asymmetry in the auroral occurrence oval. We discuss this in detail below.

5.1. Relation Between AOP and Plasma Sheet Magnetic Flux

The plasma convection pattern around Earth can be explained to first order by the Dungey cycle, which describes the magnetic flux transport in the magnetosphere (Dungey, 1961). More recently the expanding/contracting polar cap (ECPC) paradigm (Cowley & Lockwood, 1992; Milan, 2015), a modern view of the Dungey cycle, has described how convection is excited in relation to reconnection, magnetic flux transport within the magnetosphere, associated polar ionospheric flows, and changes of the polar cap size. Within the ECPC paradigm, the polar cap size, delimited by the open/closed boundary (OCB), reflects the amount of open flux in the magnetotail lobes. Expanding the ECPC concept, the ionospheric projection of the magnetotail plasma sheet (where closed flux is created during reconnection) is thus equatorward of the OCB and is topologically the preferential site of auroral precipitation (Newell et al., 2004).

The distributions shown in Figure 8 indicate that during enhanced geomagnetic activity the latitudinal extent of the AOP increases, especially on the nightside. In addition to that, the latitudinal extent of the AOP is greater on the dayside than on the nightside during geomagnetically quiet intervals. These observations suggest that the AOP evolution follows the sequence of closed magnetic flux production and loss, thus implying a mapping between plasma sheet and auroral oval. Within such a framework, we assume the amount of closed magnetic flux created by nightside reconnection, that is, in the plasma sheet, to be directly related to the probability of observing aurora.

Figure 9 illustrates the open magnetosphere produced by the Dungey cycle and the mapping between the magnetospheric plasma sheet and the auroral oval, in terms of open and closed magnetic field lines (in light and dark gray, respectively). The dayside reconnection between the Earth's and interplanetary magnetic fields comes with an opening of geomagnetic field lines, which are in turn dragged by the solar wind flow to the nightside.

21699402, 2023, 6, Downloaded from https://agupubs.onlinelibrary.wiley.com/doi/10.1029/2023JA031345 by UNIVERSITY OF BERGEN, Wiley Online Library on [24/01/2024]. See the Terms and Conditions (https://onlinelibrary.wiley.com/terms-and-conditions) on Wiley Online Library for rules of use; OA articles are governed by the applicable Creative Commons License

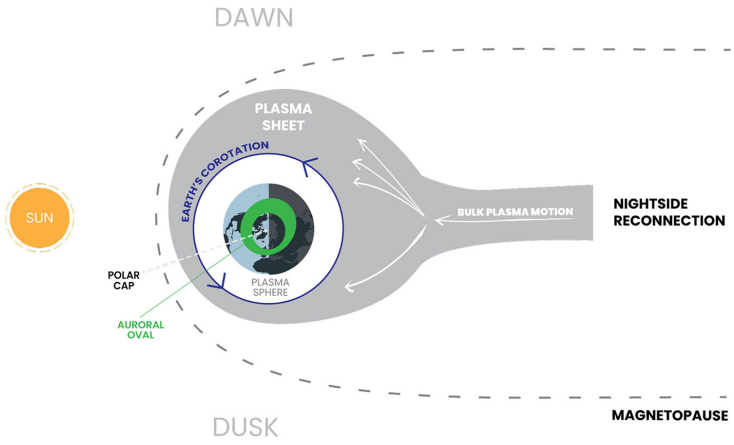

Figure 10. Schematics of the influence of Earth's rotation on the sunward transport of plasma sheet magnetic flux, as seen through a fluid description. Here, the Earth is seen from above the polar region. Illustration not to scale.

This leads to an accumulation of flux and an increase of magnetic pressure in the magnetotail lobes, where the magnetic energy is stored before being released by nightside reconnection between field lines bordering the plasma sheet. The resulting plasma sheet closed field lines are eventually moved around Earth by convection to be destroyed by dayside reconnection, completing the Dungey cycle. In this picture, the auroral oval magnetic footpoints map to the so-called plasma sheet, that is, the magnetospheric boundary between open magnetic field lines in the magnetotail lobes, which map to the polar cap, and the plasmasphere closed field lines, equatorward of the auroral oval.

5.2. Influence of Earth's Rotation on the Convection Pattern

When studying the large-scale plasma circulation in the ionosphere, a correction for the Earth's corotation is generally applied so that an object at a fixed location on Earth has zero velocity. The plasma convection in this corotating frame follows the well-known solar wind-driven two-cell convection pattern (Cowley & Lockwood, 1992), whose dusk cell has been shown to be predominant (Haaland et al., 2007). However, in reality, the high-latitude ionospheric plasma circulation not only reflects the solar wind-driven component but also the rotational motion of Earth. It has been shown that corotation impacts the return flow, making the dawn cell relatively larger than the dusk cell as Earth rotates eastward (Maynard et al., 1995). Additionally, while the solar wind-driven component of the plasma flow is highly dependent on the IMF orientation (intensifying for southward IMF and diminishing for northward IMF), the corotational component only depends on Earth's rotational speed, which is constant in time. This means that the relative importance of the corotational component also varies with the geomagnetic conditions: it tends to be negligible compared to the solar wind-driven component during high geomagnetic activity, while it becomes proportionally more important when the geomagnetic activity is low.

The distributions in Figure 8 show a persistent dawn-dusk asymmetry in the auroral occurrence oval no matter the conditions. Yet, the AOP evinces a clear response to the level of geomagnetic activity with a more distinct preference for the dawn side compared to the dusk side during periods of low activity. This dependence on the level of geomagnetic activity suggests a plausible contribution of the Earth's corotation to the observed dawn-dusk asymmetry since the asymmetric pattern is enhanced during quiet times when corotation gets relatively more significant. Underpinning this argument is the assumption that the plasma sheet maps to the auroral oval, such that the asymmetry in the AOP may be viewed as a consequence of the Earth's rotation through the direct effect of the latter on the plasma sheet magnetic flux transport.

Figure 10 illustrates the circulation of the closed magnetic flux that constitutes the plasma sheet through a fluid description (i.e., we consider only the bulk motion of the plasma). The inner boundary of the plasma sheet delimits the plasmasphere, region of cold, dense, plasma surrounding Earth equatorward of the auroral oval.

21699402, 2023, 6, Downloaded from https://agupubs.onlinelibrary.wiley.com/doi/10.1029/2023JA031345 by UNIVERSITY OF BERGEN, Wiley Online Library on [24/01/2024]. See the Terms and Conditions (https://onlinelibrary.wiley.com/terms-and-conditions) on Wiley Online Library for rules of use; OA articles are governed by the applicable Creative Commons License

21699402, 2023, 6, Downloaded from https://agupubs.onlinelibrary.wiley.com/doi/10.1029/2023JA031345 by UNIVERSITY OF BERGEN, Wiley Online Library on [24/01/2024]. See the Terms and Conditions (https://onlinelibrary.wiley.com/terms-and-conditions) on Wiley Online Library for rules of use; OA articles are governed by the applicable Creative Commons License

It can be seen that after being produced by nightside reconnection in the magnetotail, and as it is transported toward the Earth, the plasma sheet magnetic flux becomes subject to the high-latitude ionospheric convection pattern. During its sunward transport, the plasma sheet magnetic flux is thus under the influence of both the solar wind-driven convection and the Earth's corotation. As we show in what follows, the latter can apparently contribute to a "pile-up" of plasma sheet magnetic flux toward the dawn side, resulting in a wider auroral oval at dawn relative to the oval at dusk. Furthermore, during low geomagnetic activity, the dayside reconnection rate can be so low that the closed magnetic flux is only a little destroyed, resulting in a larger pile-up of flux at dawn, compared to more active periods.

Here we emphasize that the increase of the plasma sheet extent by this pile-up effect is only one interpretation of the influence of Earth's corotation through our fluid description; another possible interpretation could be that the convection of the plasma sheet around Earth goes faster toward dawn because of the corotation. In this alternative interpretation, the plasma sheet magnetic flux would reach the dawn side more often than dusk, which would in turn result in a higher probability of observing aurora at dawn relative to dusk, but not necessarily in a wider auroral oval.

5.3. Theoretical Approach—Model of the Sunward Transport of the 1D-Plasma Sheet Magnetic Flux

In order to test the corotational flow influence in creating the observed dawn-dusk asymmetry in the auroral oval, we construct a simple model of the plasma sheet magnetic flux as a function of magnetic local time. Since we seek a first-order picture of the plasma sheet (PS) fluid dynamics, we make simple assumptions in designing our model. In particular, we choose to consider a 1D, steady-state system. The core parameter is the 1D PS magnetic flux $\Psi(x)$ in units of [Wb/m], with x the length around the circle of latitude λ, starting at 0 MLT; in other words, $\Psi(x)$ can be seen as a magnetic flux per MLT, where MLT is a scaled length between 0 and $2\pi R_E \cos(\lambda)$ (0–24 MLT). We assume this PS magnetic flux to be produced at a rate $P(x)$ [V/m] via magnetic reconnection on the nightside, transported around Earth toward the dayside at a velocity $v(x)$ [m/s] and eventually destroyed via dayside reconnection, in proportion to the available flux, at a rate $\alpha(x)\Psi(x)$ [V/m]. Both $P(x)$ and $\alpha(x)$ are modeled as Gaussian distributions that respectively peak at midnight and noon. The integrated production rate $P(x)$ is chosen so that the total nightside reconnection rate is 30 kV. This corresponds to a total cross polar cap potential of 30 kV, assuming that the dayside and nightside reconnection rates exactly balance. Such value is consistent (same order of magnitude) with typical cross polar cap potential values, as seen for example, in Haaland et al. (2007). On the other hand, the loss coefficient $\alpha(x)$ has an amplitude that is sufficient to destroy all closed flux by dayside reconnection before it reaches noon. The full width at half maximum for both parameters is 1.33 MLT.

The 1D closed magnetic flux $\Psi(x)$ is then described through the time-stationary 1D continuity equation along a circle of latitude λ

$$\Psi(x)\frac{dv(x)}{dx} + v(x)\frac{d\Psi(x)}{dx} = P(x) - \alpha(x)\Psi(x), \quad (1)$$

with $v(x) = V_{SW} + V_{corotation}$ since our model takes into account both solar wind-driven convection flow and constant corotational flow in the sunward transport of the PS magnetic flux. We approximate V_{SW} as $V_0 \sin(x)$, such that it describes a return flow that maximizes at $x = 6$ and 18 MLT. According to convection studies, V_0 is usually between 200 m/s and 600 m/s, depending on the level of geomagnetic activity (Reistad et al., 2018). In our study we make V_0 vary within that range in order to reproduce the balance between corotation and return flow for various geomagnetic conditions. As for the corotation speed $V_{corotation}$, which only varies with geographic latitude, we set it to an approximate value of 158 m/s at 70° MLat (Laundal et al., 2022). By choosing a latitude typically within the auroral region, we ensure that the estimated corotation speed corresponds to its value in the magnetospheric PS.

In the end, all Equation 1 parameters are assumed to be known and only Ψ is an unknown function of x. The transport equation can then be solved by using finite differences with the periodic boundary condition that $\Psi(0) = \Psi(24)$.

5.4. Is Corotation Enough to Explain the Dawn Preference in the AOP ?

We solve Equation 1 for a slow ($V_0 = 200$ m/s) and a fast ($V_0 = 600$ m/s) return flow, and compare the resulting MLT profiles of the modeled PS magnetic flux $\Psi(x)$ for two different corotation/return flow equilibria with the MLT profiles of 1D-AOP for two different levels of geomagnetic activity.

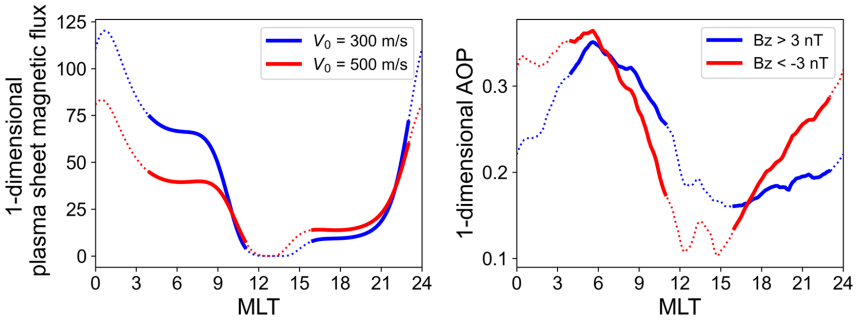

Figure 11. Left panel: Modeled 1D-plasma sheet magnetic flux as a function of magnetic local time (MLT) $\Psi(x)$ for low (blue) and high (red) convection speed. Right panel: 1D-AOP as a function of MLT for B_z positive (blue) and B_z negative (red) (same as the bottom left plot in Figure 8).

The left panel of Figure 11 shows the MLT profiles of the PS magnetic flux derived from our model. As expected from closed flux, and independently of V_0, most of the PS magnetic flux is located on the nightside, with a post-midnight peak, while very little flux is left around noon. Besides that, we can immediately spot the asymmetric distribution of magnetic flux between the dawn and dusk sides. From our investigation of the AOP response to IMF B_z (Section 4.6), we have shown that the MLT profiles of 1D-AOP evince similar features, regardless of B_z sign (right panel of Figure 11). Additionally, Figure 11 highlights how the level of geomagnetic activity influences the dawn-dusk asymmetric pattern for both the 1D-AOP and 1D-PS magnetic flux. Favorable magnetic conditions for reconnection (negative B_z) and increased return flow velocity (V_0 = 600 m/s) both express geomagnetically active times, while more quiet times generally come with a northward IMF (positive B_z) and a slower return flow (V_0 = 200 m/s). We find that the two quantities show the same specific response, that is an increased asymmetry for lower geomagnetic activity (blue lines) and a reduced, but persistent, asymmetry for higher activity (red lines), with a lingering dawn preference.

The simple model that we have constructed ignores the complexities of several relevant physical processes, including particular mechanisms for particle precipitation and the effects of different solar wind parameters. We nevertheless suggest that the correlation between the 1D-AOP and our model of 1D-PS magnetic flux can be extrapolated such that the asymmetric distributions of PS magnetic flux and AOP are related. In this picture, the role of Earth's corotation in producing a dawn-dusk asymmetry in the auroral occurrence oval thus reflects the driving of more PS magnetic flux toward the dawn side during its sunward transport. The relative importance of the dawn cell compared to the dusk cell is drastically increased during low geomagnetic activity due to the combined action of convection being controlled by corotation and an overall lower rate of removal of accumulated PS flux by dayside reconnection. Conversely, during higher geomagnetic activity the solar wind influence dominates the convection system over corotation, leading to a more homogeneous distribution of PS magnetic flux and a less pronounced dawn preference. Independently of geomagnetic conditions and how intense the corotation effect is, we have argued that this could result in either a magnetic flux pile-up at dawn (wider auroral oval) or simply an increased probability of aurora at dawn, regardless of width.

In conclusion, our fluid description of the evolution of the auroral oval morphology indicates that the Earth's rotation may contribute to the dawn-dusk asymmetry observed in our AOP distributions. Nonetheless, the supposed predominance of the corotation influence on the formation of asymmetric patterns in the auroral oval does not necessarily remain true when going beyond our fluid model and its related bulk plasma motion. When considering the whole complex picture, particle precipitation mechanisms have a central role in producing the observed dawn-dusk asymmetry, and their relative importance compared to the bulk plasma motion associated effects should be thoroughly analyzed. According to (Eq. 3.21 Baumjohann & Treumann, 1997), the magnetic drift speed is proportional to particle energy, such that energetic electrons will drift eastward (and ions westward) faster than the Earth's rotational speed. However, for 1 keV particles, the lower energy limit used for our AOP maps, corotation is faster than magnetic drift by a factor of ≈6.7, assuming a dipole field at 67° latitude. This supports our suggestion that corotation influences the dawn-dusk asymmetry observed in this paper, although it is likely negligible for higher energy particles.

21699402, 2023, 6, Downloaded from https://agupubs.onlinelibrary.wiley.com/doi/10.1029/2023JA031345 by UNIVERSITY OF BERGEN, Wiley Online Library on [24/01/2024]. See the Terms and Conditions (https://onlinelibrary.wiley.com/terms-and-conditions) on Wiley Online Library for rules of use; OA articles are governed by the applicable Creative Commons License

21699402, 2023, 6, Downloaded from https://agupubs.onlinelibrary.wiley.com/doi/10.1029/2023JA031345 by UNIVERSITY OF BERGEN, Wiley Online Library on [24/01/2024]. See the Terms and Conditions (https://onlinelibrary.wiley.com/terms-and-conditions) on Wiley Online Library for rules of use; OA articles are governed by the applicable Creative Commons License

6. Conclusion

In this study, we have presented a method for investigating the auroral oval morphology. Using a threshold for aurora detection of $2 \cdot 10^9$ eV/cm^2/s/sr, we have derived the AOP from 20 years of DMSP/SSJ electron energy flux measurements in the energy range 1–30 keV, and have used it to assess the probabilistic extent of the auroral oval as a function of magnetic local time. We have shown that the AOP evinces a typical asymmetric pattern with a clear and persistent enhancement at dawn that is independent of the data selection. In particular, this pattern is very well conserved with respect to variation of the auroral detection threshold as well as substorm epoch. On the other hand, the dawn-dusk asymmetry varies with the level of geomagnetic activity, being more pronounced during geomagnetically quiet periods and less prominent during periods of enhanced geomagnetic activity. While this dawn-dusk asymmetry in the auroral oval has been described before in average auroral precipitation studies, here we have pointed out the differences between the AOP and the average energy flux, and the prominence of diffuse precipitation in our data analysis.

These aspects, taken together, prompt consideration of possible alternatives to the usual explanation of the auroral oval dynamics through kinetic effects. In specific, we have posited that it may be possible to describe the governing physical processes involved in shaping the asymmetric auroral oval in terms of convection by assuming a mapping between the magnetospheric plasma sheet and the auroral oval. We have therefore constructed a simple 1-D model of the plasma sheet magnetic flux, subject to production and loss of closed flux by magnetic reconnection as well as Earth's corotation, to compare its MLT dependence with that of the AOP. Our model suggests that the features of the auroral occurrence oval may depend on the amount of plasma sheet magnetic flux being convected from the nightside to the dayside. Moreover, the persistent dawn preference can apparently be described in part as a consequence of the Earth's rotation, which drives more magnetic flux toward the east. The tendency of the dawn-dusk asymmetry to be more prominent during low geomagnetic activity supports the idea that corotation plays a role in shaping the distribution of the occurrence of aurora.

For future research, it will be of interest to extend the database that we use in this study by including precipitation measurements made by other low Earth-orbiting satellites, such as the NOAA POES satellites, or possibly combining precipitation measurements with, for example, global auroral images from the upcoming SMILE mission. One could also make use of magnetohydrodynamics simulations to produce model AOP distributions.

Data Availability Statement

The data used in this paper (see Section 2) come from publicly available databases through the following links. The DMSP/SSJ data were obtained from NASA/GSFC CDAWeb at https://cdaweb.gsfc.nasa.gov/pub/data/dmsp/. The OMNI data, including the solar wind data and geomagnetic activity indices, are available on the NASA/GSFC SPDF interface at http://spdf.gsfc.nasa.gov/pub/data/omni/high_res_omni/. The substorm data are accessible at the JHU/APL SuperMAG website at https://supermag.jhuapl.edu/substorms/?tab=download.

Acknowledgments
This study was funded by the Trond Mohn Foundation, and by the Research Council of Norway through contracts 223252/F50 and 300844/F50. We thank R.J. Redmon and L.M. Kilcommons for providing the DMSP/SSJ data, and J.H. King and N.E. Papitashvili for the multi-sources OMNI data. We acknowledge the use of NASA/GSFC SPDF service to obtain these data. We also acknowledge the substorm timing list identified by the Ohtani and Gjerloev technique (Ohtani & Gjerloev, 2020), the SMU and SML indices (Newell & Gjerloev, 2011); and the SuperMAG collaboration (Gjerloev, 2012). Finally, we thank A. Decotte for nicely illustrating the conceptual ideas behind this paper (Figures 9 and 10).

References

Baumjohann, W., & Treumann, R. (1997). *Basic space plasma physics*. Imperial College Press.
Breddels, M. A., & Veljanoski, J. (2018). Vaex: Big data exploration in the era of gaia. *A&A*, *618*, A13. https://doi.org/10.1051/0004-6361/201732493
Burrell, A. G., Chisham, G., Milan, S. E., Kilcommons, L., Chen, Y.-J., Thomas, E. G., & Anderson, B. (2020). Ampere polar cap boundaries. *Annales Geophysicae*, *38*(2), 481–490. https://doi.org/10.5194/angeo-38-481-2020
Chisham, G., Burrell, A. G., Thomas, E. G., & Chen, Y.-J. (2022). Ionospheric boundaries derived from auroral images. *Journal of Geophysical Research: Space Physics*, *127*(7). e2022JA030622. https://doi.org/10.1029/2022JA030622
Coumans, V., Gérard, J.-C., Hubert, B., & Evans, D. S. (2002). Electron and proton excitation of the FUV aurora: Simultaneous image and NOAA observations. *Journal of Geophysical Research*, *107*(A11), 1347. https://doi.org/10.1029/2001JA009233
Cowley, S. (1981). Magnetospheric asymmetries associated with the y-component of the IMF. *Planetary and Space Science*, *29*(1), 79–96. https://doi.org/10.1016/0032-0633(81)90141-0
Cowley, S., & Lockwood, M. (1992). Excitation and decay of solar-wind driven flows in the magnetosphere-ionosphere system. *Annales Geophysicae*, *10*, 103–115.
Di Matteo, S., & Sivadas, N. (2022). Solar-wind/magnetosphere coupling: Understand uncertainties in upstream conditions. *Frontiers in Astronomy and Space Sciences*, *9*. https://doi.org/10.3389/fspas.2022.1060072
Dombeck, J., Cattell, C., Prasad, N., Meeker, E., Hanson, E., & McFadden, J. (2018). Identification of auroral electron precipitation mechanism combinations and their relationships to net downgoing energy and number flux. *Journal of Geophysical Research: Space Physics*, *123*(12). 2018JA025749. https://doi.org/10.1029/2018JA025749
Dungey, J. W. (1961). Interplanetary magnetic field and the auroral zones. *Physical Review Letters*, *6*(2), 47–48. https://doi.org/10.1103/PhysRevLett.6.47

Feldstein, Y. (2016). The discovery and the first studies of the auroral oval: A review. *Geomagnetism and Aeronomy*, *56*(2), 129–142. https://doi.org/10.1134/S0016793216020043

Feldstein, Y. I. (1964). Auroral morphology, II. Auroral and geomagnetic disturbances. *Tellus*, *16*(2), 258–267. https://doi.org/10.1111/j.2153-3490.1964.tb00164.x

Feldstein, Y. I., & Starkov, G. V. (1967). Dynamics of auroral belt and polar geomagnetic disturbances. *Planetary and Space Science*, *15*(2), 209–229. https://doi.org/10.1016/0032-0633(67)90190-0

Gjerloev, J. W. (2012). The SuperMAG data processing technique. *Journal of Geophysical Research: Space Physics*, *117*(A9). https://doi.org/10.1029/2012JA0176

Haaland, S., Paschmann, G., Foerster, M., Quinn, J., Torbert, R., Mcilwain, C., et al. (2007). High-latitude plasma convection from cluster EDI measurements: Method and IMF-dependence. *Annales Geophysicae*, *25*(1), 239–253. https://doi.org/10.5194/angeo-25-239-2007

Hardy, D. A., Gussenhoven, M. S., & Holeman, E. (1985). A statistical model of auroral electron precipitation. *Journal of Geophysical Research*, *90*(A5), 4229–4248. https://doi.org/10.1029/JA090iA05p04229

Hatch, S. M., Laundal, K. M., & Reistad, J. P. (2022). Testing the mirror symmetry of birkeland and ionospheric currents with respect to magnetic latitude, dipole tilt angle, and imf by. *Frontiers in Astronomy and Space Sciences*, *9*. https://doi.org/10.3389/fspas.2022.958977

Holzworth, R. H., & Meng, C.-I. (1975). Mathematical representation of the auroral oval. *Geophysical Research Letters*, *2*(9), 377–380. https://doi.org/10.1029/GL002i009p00377

Juusola, L., Vanhamäki, H., Viljanen, A., & Smirnov, M. (2020). Induced currents due to 3d ground conductivity play a major role in the interpretation of geomagnetic variations. *Annales Geophysicae*, *38*(5), 983–998. https://doi.org/10.5194/angeo-38-983-2020

Keiling, A., Wygant, J. R., Cattell, C. A., Mozer, F. S., & Russell, C. T. (2003). The global morphology of wave Poynting flux: Powering the aurora. *Science*, *299*(5605), 383–386. https://doi.org/10.1126/science.1080073

Khazanov, G. V., & Glocer, A. (2020). How magnetically conjugate atmospheres and the magnetosphere participate in the formation of low-energy electron precipitation in the region of diffuse aurora. *Journal of Geophysical Research: Space Physics*, *125*(8). https://doi.org/10.1029/2020JA028057

Kilcommons, L. M., Redmon, R. J., & Knipp, D. J. (2017). A new DMSP magnetometer and auroral boundary data set and estimates of field-aligned currents in dynamic auroral boundary coordinates. *Journal of Geophysical Research: Space Physics*, *122*(8), 9068–9079. https://doi.org/10.1002/2016JA023342

King, J. H., & Papitashvili, N. E. (2005). Solar wind spatial scales in and comparisons of hourly wind and ace plasma and magnetic field data. *Journal of Geophysical Research*, *110*(A2), A02104. https://doi.org/10.1029/2004JA010649

Laundal, K. M., Madelaire, M., Ohma, A., Reistad, J., & Hatch, S. (2022). The relationship between interhemispheric asymmetries in polar ionospheric convection and the magnetic field line footpoint displacement field. *Frontiers in Astronomy and Space Sciences*, *9*. https://doi.org/10.3389/fspas.2022.957223

Laundal, K. M., Østgaard, N., Frey, H. U., & Weygand, J. M. (2010). Seasonal and interplanetary magnetic field–dependent polar cap contraction during substorm expansion phase. *Journal of Geophysical Research*, *115*(A11). https://doi.org/10.1029/2010JA015910

Maynard, N. C., Denig, W. F., & Burke, W. J. (1995). Mapping ionospheric convection patterns to the magnetosphere. *Journal of Geophysical Research*, *100*(A2), 1713–1721. https://doi.org/10.1029/94JA02626

Milan, S. E. (2015). Sun et lumière: Solar wind-magnetosphere coupling as deduced from ionospheric flows and polar auroras. In S. W. H. Cowley FRS, D. Southwood, & S. Mitton (Eds.), *Magnetospheric plasma physics: The impact of jim dungey's research* (pp. 33–64). Springer International Publishing.

Milan, S. E., Lester, M., Cowley, S. W. H., Oksavik, K., Brittnacher, M., Greenwald, R. A., et al. (2003). Variations in the polar cap area during two substorm cycles. *Annales Geophysicae*, *21*(5), 1121–1140. https://doi.org/10.5194/angeo-21-1121-2003

Moore, T. E., Chandler, M. O., Chappell, C. R., Pollock, C. J., Waite, J. H., Horwitz, J. L., et al. (1989). Features of terrestrial plasma transport [and discussion]. *Philosophical Transactions of the Royal Society of London - Series A: Mathematical and Physical Sciences*, *328*(1598), 235–254.

Newell, P. T., Feldstein, Y. I., Galperin, Y. I., & Meng, C.-I. (1996). Morphology of nightside precipitation. *Journal of Geophysical Research*, *101*(A5), 10737–10748. https://doi.org/10.1029/95JA03516

Newell, P. T., & Gjerloev, J. W. (2011). Evaluation of SuperMAG auroral electrojet indices as indicators of substorms and auroral power. *Journal of Geophysical Research: Space Physics*, *116*(A12). https://doi.org/10.1029/2011JA016779

Newell, P. T., Liou, K., Zhang, Y., Sotirelis, T., Paxton, L. J., & Mitchell, E. J. (2014). Ovation prime-2013: Extension of auroral precipitation model to higher disturbance levels. *Space Weather*, *12*(6), 368–379. https://doi.org/10.1002/2014SW001056

Newell, P. T., Ruohoniemi, J. M., & Meng, C.-I. (2004). Maps of precipitation by source region, binned by imf, with inertial convection streamlines. *Journal of Geophysical Research*, *109*(A10), A10206. https://doi.org/10.1029/2004JA010499

Newell, P. T., Sotirelis, T., & Wing, S. (2009). Diffuse, monoenergetic, and broadband aurora: The global precipitation budget. *Journal of Geophysical Research*, *114*(A9). https://doi.org/10.1029/2009JA014326

Ni, B., Thorne, R., Zhang, X.-J., Bortnik, J., Pu, Z., Xie, L., et al. (2016). Origins of the earth's diffuse auroral precipitation. *Space Science Reviews*, *200*(1–4), 205–259. https://doi.org/10.1007/s11214-016-0234-7

Ohtani, S., & Gjerloev, J. W. (2020). Is the substorm current wedge an ensemble of wedgelets?: Revisit to midlatitude positive bays. *Journal of Geophysical Research: Space Physics*, *125*(9). https://doi.org/10.1029/2020JA027902

Papitashvili, N., Bilitza, D., & King, J. (2014). OMNI: A description of near-earth solar wind environment. *40th cospar scientific assembly*, (Vol. 40, p. C0.1-12-14).

Redmon, R. J., Denig, W. F., Kilcommons, L. M., & Knipp, D. J. (2017). New DMSP database of precipitating auroral electrons and ions. *Journal of Geophysical Research: Space Physics*, *122*(8), 9056–9067. https://doi.org/10.1002/2016JA023339

Reistad, J. P., Østgaard, N., Laundal, K. M., Ohma, A., Snekvik, K., Tenfjord, P., et al. (2018). Observations of asymmetries in ionospheric return flow during different levels of geomagnetic activity. *Journal of Geophysical Research: Space Physics*, *123*(6), 4638–4651. https://doi.org/10.1029/2017JA025051

Richmond, A. D. (1995). Ionospheric electrodynamics using magnetic apex coordinates. *Journal of Geomagnetism and Geoelectricity*, *47*(2), 191–212. https://doi.org/10.5636/jgg.47.191

Rodger, C. J., Cresswell-Moorcock, K., & Clilverd, M. A. (2016). Nature's grand experiment: Linkage between magnetospheric convection and the radiation belts. *Journal of Geophysical Research: Space Physics*, *121*(1), 171–189. https://doi.org/10.1002/2015JA021537

Shue, J.-H., Newell, P. T., Liou, K., & Meng, C.-I. (2001). Influence of interplanetary magnetic field on global auroral patterns. *Journal of Geophysical Research*, *106*(A4), 5913–5926. https://doi.org/10.1029/2000JA003010

Tromholt, S. (1882). *Om nordlysets perioder/sur les périodes de l'aurore boréale, l'annuaire 1880*. Inst. Météorol. Danois.

21699402, 2023, 6, Downloaded from https://agupubs.onlinelibrary.wiley.com/doi/10.1029/2023JA031345 by UNIVERSITY OF BERGEN, Wiley Online Library on [24/01/2024]. See the Terms and Conditions (https://onlinelibrary.wiley.com/terms-and-conditions) on Wiley Online Library for rules of use; OA articles are governed by the applicable Creative Commons License

Paper II

Occurrence Probability of Magnetic Field Disturbances Measured With Swarm: Mapping the Dynamic Magnetosphere-Ionosphere Coupling

Margot Decotte, Karl M. Laundal, Spencer M. Hatch, Jone P. Reistad
Journal of Geophysical Research: Space Physics, **129**/**2** (2024)
doi: 10.1029/2023JA032191

Check for updates

JGR Space Physics

RESEARCH ARTICLE
10.1029/2023JA032191

Occurrence Probability of Magnetic Field Disturbances Measured With Swarm: Mapping the Dynamic Magnetosphere-Ionosphere Coupling

Margot Decotte[1], Karl M. Laundal[1], Spencer M. Hatch[1], and Jone P. Reistad[1]

[1]Department of Physics and Technology, University of Bergen, Bergen, Norway

Key Points:

- The disturbed magnetic field occurrence probability is derived from Swarm measurements in the polar regions and investigated statistically
- Low-frequency distributions evince a persistent dawn-dusk asymmetry, peaking at dawn, similar to auroral electron precipitation
- The disturbed magnetic field occurrence probability could, like auroral precipitation observations, be used to infer magnetospheric dynamics

Correspondence to:

M. Decotte,
margot.decotte@uib.no

Citation:

Decotte, M., Laundal, K. M., Hatch, S. M., & Reistad, J. P. (2024). Occurrence probability of magnetic field disturbances measured with Swarm: Mapping the dynamic magnetosphere-ionosphere coupling. *Journal of Geophysical Research: Space Physics*, *129*, e2023JA032191. https://doi.org/10.1029/2023JA032191

Received 16 OCT 2023
Accepted 24 JAN 2024

Author Contributions:

Conceptualization: Margot Decotte, Karl M. Laundal
Formal analysis: Margot Decotte
Funding acquisition: Karl M. Laundal
Investigation: Margot Decotte, Karl M. Laundal
Methodology: Margot Decotte, Spencer M. Hatch
Project administration: Karl M. Laundal
Supervision: Karl M. Laundal, Spencer M. Hatch, Jone P. Reistad
Writing – original draft: Margot Decotte
Writing – review & editing: Margot Decotte, Karl M. Laundal, Spencer M. Hatch, Jone P. Reistad

©2024. The Authors.
This is an open access article under the terms of the Creative Commons Attribution License, which permits use, distribution and reproduction in any medium, provided the original work is properly cited.

Abstract The exchange of kinetic and electromagnetic energy by precipitation and/or outflow and through field-aligned currents are two aspects of the ionosphere-magnetosphere coupling. A thorough investigation of these processes is required to better understand magnetospheric dynamics. Building on our previous study using the Defense Meteorological Satellite Program spectrometer data, here we use Swarm vector field magnetometer data to describe the auroral zone morphology in terms of east-west magnetic field perturbations. We define a threshold for detecting magnetic fluctuations based on the power spectral density of ΔB_{EW}, and derive the disturbed magnetic field occurrence probability (dBOP) at low [0.1–1 Hz] and high [2.5–5 Hz] frequencies. High-frequency distributions of dBOP reveal a dayside-nightside asymmetry, whereas low-frequency dBOP exhibits a persistent morphological asymmetry between the dawn-to-noon and the dusk-to-midnight sectors, peaking at dawn. Notably, weak solar wind conditions are associated with an increase in the dBOP asymmetric patterns. At low frequency in particular, while the dBOP seems to be primarily constant at dawn, the dusk dBOP decreases during quiet times, inducing a relatively larger dawn-dusk asymmetry in such conditions. Furthermore, based on a comparison analysis between low-frequency dBOP and auroral electron precipitation occurrence probability, we suggest that both types of distribution offer a more comprehensive understanding of the large-scale auroral zone when considered concurrently. Our interpretation is that the dBOP at low frequencies reflects a quasi-steady state circulation of energy, while the high-frequency dBOP reflects the regions of rapid changes in the magnetosphere. The dBOP is therefore a crucial source of information regarding the magnetosphere-ionosphere coupling.

Plain Language Summary The Earth's magnetic environment (magnetosphere) and the ionized upper atmosphere (ionosphere) are electrodynamically coupled. Within the magnetosphere-ionosphere (MI) system, energy and momentum are exchanged through both charged and neutral particles. The polar ionosphere, particularly in the auroral zone, constitutes a convergence region for magnetospheric energy. While it is commonly thought of as a visual spectacular event, the definition of aurora is broad and all types of aurora are not necessarily visible from the ground. Aurora can also be inferred from satellite data, such as precipitating electron energy flux and magnetic field perturbations. In this study, we derive the occurrence probability of magnetic field perturbations based on crossings of the polar region by the Swarm satellites. In terms of spatial distribution, magnetic fluctuations exhibit an asymmetric pattern that is also observed in the occurrence probability of auroral precipitation. These two quantities reflect different aspects of the auroral zone, such that their joined examination offers significant perspectives in the quest for a better understanding of the complex and dynamic MI coupling.

1. Introduction

Magnetic reconnection at Earth's dayside magnetosphere results in the exchange of plasma populations between the solar wind and the magnetosphere (Dungey, 1961). Following Dungey's cycle, the motion of plasma and the associated convection of magnetic flux within the magnetosphere leads to reconnection in the magnetotail, which in turn excites a flow of accelerated electrons and ions toward the Earth. Solar wind energy and momentum are ultimately transferred from the magnetosphere to the high-latitude ionosphere via the field-aligned currents (FACs), which themselves arise as a response to the stresses applied to the magnetosphere-ionosphere (MI) system (Strangeway et al., 2000) and are carried by charged particles flowing along magnetic field lines. FACs have been broadly studied based on observations from low-orbiting satellites, as well as inferred from radars and ground-based magnetometer network observations (e.g., Christiansen et al., 2002; Iijima & Potemra, 1976;

21699402, 2024, 2, Downloaded from https://agupubs.onlinelibrary.wiley.com/doi/10.1029/2023JA032191 by UNIVERSITY OF BERGEN, Wiley Online Library on [07/02/2024]. See the Terms and Conditions (https://onlinelibrary.wiley.com/terms-and-conditions) on Wiley Online Library for rules of use; OA articles are governed by the applicable Creative Commons License

Kamide et al., 1981; Kustov et al., 2000). These and many additional studies have established that FACs play a fundamental role in the solar wind-magnetosphere-ionosphere coupling and, more specifically, auroral physics (Milan et al., 2017).

The auroral oval is commonly described as the high-latitude region where energetic electrons, originally accelerated in the magnetospheric plasma sheet, precipitate (Khazanov & Glocer, 2020; Newell et al., 2004, 2009). A myriad of studies have focused on auroral particle measurements in the specific context of defining a proxy of the auroral oval. Dombeck et al. (2018), Zhang and Paxton (2008) and Newell et al. (2004, 2014), for example, derived statistical models of the aurora based on the average precipitating energy flux. In particular, the OVATION Prime model aims at predicting the auroral power deposited in the ionosphere, depending on the solar wind driving. Newell et al. (2009) also contributed to developing auroral precipitation forecasting as they categorized the aurora into diffuse, monoenergetic, broadband, and ion.

Extended knowledge of auroral precipitation has benefited the investigation of the auroral region morphology and dynamics. In their studies, Newell et al. (1996); Redmon et al. (2010); Kilcommons et al. (2017a) derived the auroral oval boundaries based on precipitation data. Recently, Decotte et al. (2023) obtained maps of auroral occurrence probability from precipitating electron energy flux measurements. Furthermore, the expanding-contracting polar cap model predicts the size of the polar cap, depending on the opening and closure of magnetic flux through dayside and nightside reconnection (Cowley & Lockwood, 1992). This, in turn, controls the open-closed boundary (OCB) location, which varies with the amount of open magnetic flux in the magnetotail lobes. Chisham et al. (2022), among others (e.g., Carbary et al., 2003; Kauristie et al., 1999; Laundal et al., 2010; Newell et al., 2004) have demonstrated that the OCB essentially constitutes the poleward precipitation auroral oval boundary.

In the past decades, it has been extensively shown that a relationship exists between magnetic field perturbations/FACs and particle precipitation. Sato et al. (2004) investigated magnetic field variations and concluded that they were in phase with the high-energy electron flux seen by the Fast Auroral SnapshoT Explorer satellite. Similarly, Hatch, Moretto, et al. (2020) demonstrated the statistical relationship between east-west magnetic field fluctuations and energetic outflows in the MI transition region. It has also been shown that electron and ion energy flux increase with FACs magnitude in both upward and downward current regions (Robinson et al., 2018). Although they pointed out systematic differences in the location of particle energy fluxes and FACs intensity peak, Xiong et al. (2020) showed that electron and ion energy flux behave in a similar way as FACs, with, in particular, a similar response to enhanced southward B_z.

It has additionally been established in many different studies that magnetic fluctuations and auroral structures were related. Nagatsuma et al. (1995) have found a latitudinally narrow FAC system on the poleward boundary of the nightside auroral oval. They found that this boundary current system is associated with suprathermal electrons with pitch angles predominately in the field-aligned direction. Nagatsuma et al. (1996) further demonstrated that the FAC fluctuations in this boundary current system are due to the superposition of incident and reflected Alfvén waves. Fujii et al. (1985) established that the magnetic fluctuations related well to the fluctuations in auroral luminosities estimated at 100 km altitude. Moreover, Gillies et al. (2015) used Swarm magnetometers to demonstrate the existence of a region of fluctuating FACs associated with persistent patchy pulsating aurora structures.

Hence, while precipitation studies are crucial in the quest for a better understanding of the auroral region, FACs appear to be a reasonable proxy for the auroral oval. Xiong et al. (2014) have derived auroral oval boundaries from small- and medium-scale FACs and have validated the position of these boundaries against the British Antarctic Survey auroral model derived from IMAGE optical observations. Iijima and Potemra (1978) suggested that FACs sheets are generally aligned with the poleward boundary of the auroral oval, which has been proven true by Burrell et al. (2020), as they derived the OCB location from the region 1 to region 2 FACs boundary.

The auroral oval is the region of the ionosphere-thermosphere system where the magnetospheric energy converges (Thayer & Semeter, 2004). This convergence of energy results in, among other things, photon emission, Joule heating and satellite drag in the upper atmosphere, and electric currents as well as associated ground magnetic field disturbances (Juusola et al., 2020). A better understanding of the auroral oval dynamics would therefore benefit the MI coupling research and more generally contribute to a better understanding of how the space environment impacts Earth. However, it is challenging to monitor the dynamics of the auroral oval, as this region is highly variable both in space and time (Ohma et al., 2023). All available sensing methods should then be

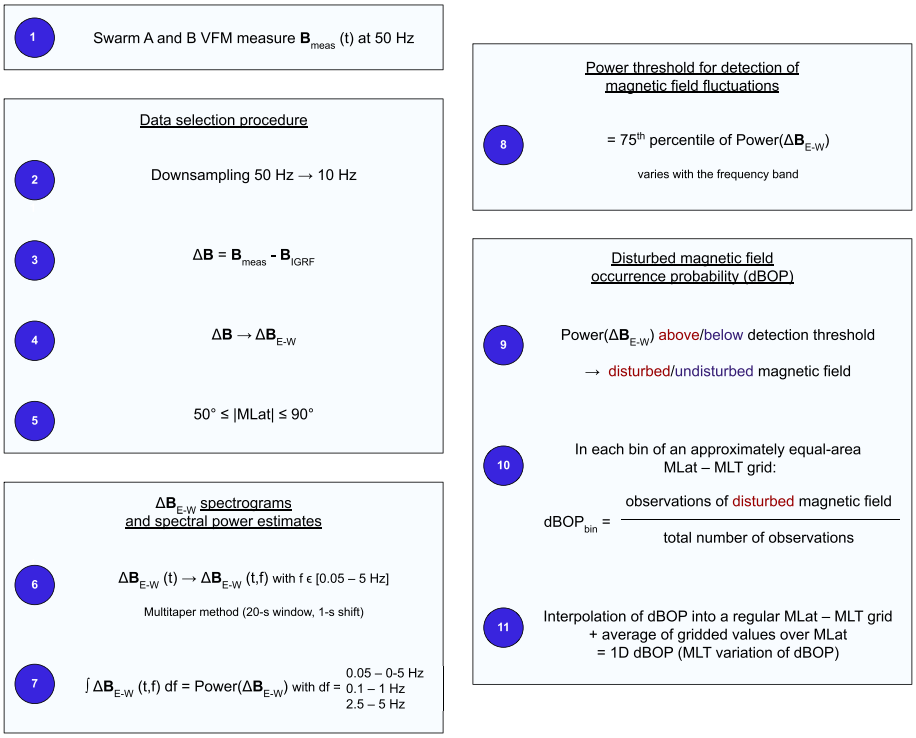

Figure 1. Diagram summarizing the analysis procedure leading to the derivation of the disturbed magnetic field occurrence probability. Each step is described in more detail throughout Section 2.

considered when investigating the auroral oval. This study follows a previous investigation of the auroral occurrence probability, using electron precipitation data from the Defense Meteorological Satellite Program (DMSP) (Decotte et al., 2023). Here we use the Swarm magnetometer data and derive the disturbed magnetic field occurrence probability (dBOP) in the auroral region. This is an alternative to deriving the auroral boundaries directly, which can be ambiguous as it has been shown that the relation between optical observations, ground and space magnetic field measurements, FACs, etc. is complex (Walker et al., 2023). Further, when derived from Sun-synchronous satellite observations, modeled boundaries are subject to a local time bias that is bypassed when looking at occurrence probability instead (Decotte et al., 2023). We aim to investigate if the dBOP could be a reliable proxy of the auroral oval.

In Section 2 we introduce the data sets used in this study, which comprise magnetic field and interplanetary magnetic field (IMF) data. We then describe the methodology for deriving the dBOP from magnetic field perturbations. We present the resulting occurrence distributions (maps and magnetic local time (MLT) profiles) as a function of external conditions such as solar wind driving and substorm activity in Section 3. In Section 4 we summarize the results in terms of morphological features of the auroral oval, and we discuss our findings in relation to the auroral electron precipitation occurrence probability (POP) derived in our previous study (Decotte et al., 2023).

2. Data and Methodology

In this section, we present the data used in our study. We also give a detail of the data pre-processing before we introduce the concept of disturbed magnetic field occurrence probability. A summary of the analysis steps is presented as a diagram in Figure 1.

21699402, 2024, 2, Downloaded from https://agupubs.onlinelibrary.wiley.com/doi/10.1029/2023JA032191 by UNIVERSITY OF BERGEN, Wiley Online Library on [07/02/2024]. See the Terms and Conditions (https://onlinelibrary.wiley.com/terms-and-conditions) on Wiley Online Library for rules of use; OA articles are governed by the applicable Creative Commons License

21699402, 2024, 2, Downloaded from https://agupubs.onlinelibrary.wiley.com/doi/10.1029/2023JA032191 by UNIVERSITY OF BERGEN, Wiley Online Library on [07/02/2024]. See the Terms and Conditions (https://onlinelibrary.wiley.com/terms-and-conditions) on Wiley Online Library for rules of use; OA articles are governed by the applicable Creative Commons License

2.1. Swarm Magnetic Field Data Set

Our study relies on the measurement of magnetic field perturbations provided by the Vector Field Magnetometer (VFM) carried aboard the Swarm satellites as they cross the polar auroral region. The Swarm constellation mission consists of three identical satellites (A, B, and C) in near-polar, circular orbits. Swarm A and C form a pair as they are flying side-by-side (separated by 1.4° in longitude) at approximately 460 km altitude, while Swarm B orbits at a higher altitude of approximately 510 km. All three satellites have an inclination angle of about 87°–88°. Such a multi-satellite configuration is well suited to study the current systems of the polar ionosphere (Ritter et al., 2013). We use the virtual research platform—VirES for Swarm—(Smith & Pačes, 2022) to access and collect the high-resolution (50 Hz) magnetic field vector data, which are provided in a local NEC (North-East-Centre) geocentric reference frame. After converting from geocentric to geodetic coordinates, we downsample the Swarm 50 Hz magnetic field vector measurements to 10 Hz by selecting every fifth data point, and we eventually gather all available data from Swarm A and B between 2014 and 2021. We omit Swarm C in our analysis as Swarm A and C are expected to give similar results due to their proximity and the similarity of their orbital configurations.

As we aim to investigate how the disturbed magnetic field behaves under various geomagnetic conditions, we combine our Swarm data set with the solar wind magnetic field and plasma parameters from the OMNI database. We point out that these data represent near-Earth estimates of solar wind properties as the original upstream observations have been time-shifted to the Earth's bow shock nose (King & Papitashvili, 2005).

2.2. Data Selection Procedure

We use the International Geomagnetic Reference Field model to infer the Earth's main magnetic field component for each Swarm data point. We then subtract it from the measured magnetic field, such that only the magnetic field perturbations remain: $\mathbf{B}_{\text{meas}} - \mathbf{B}_{\text{IGRF}} = \Delta\mathbf{B}$. After converting the residual perturbation vector to Apex coordinates (Richmond, 1995), we extract the magnetic field perturbation in the magnetic East-West direction $\Delta\mathbf{B}_{\text{EW}}$. The selected data should then mostly reflect FAC sheets that run primarily in that direction. The rest of the analysis applies to the portions of the $\Delta\mathbf{B}_{\text{EW}}$ time series falling within $50° \leq |\text{MLat}| \leq 90°$, with the magnetic latitude (MLat) in Modified Apex coordinates (Laundal & Richmond, 2017).

2.3. $\Delta\mathbf{B}_{\text{EW}}$ Spectrograms and Spectral Power Estimates

We use the multitaper method (e.g., Hatch, Haaland, et al., 2020) to derive spectrograms (power spectral density vs. frequency and time) from $\Delta\mathbf{B}_{\text{EW}}$ time series. Each power spectrum is calculated from a 20-s window (201 measurements at 10 Hz), and consecutive power spectra are calculated using a 1-s shift. Consequently, given the frequency lower limit (0.05 Hz) and the spacecraft velocity (7.5 km/s), only currents with spatial scales smaller than 150 km are represented. Note that by cutting the 0 Hz frequency we eliminate fluctuations that would otherwise contribute to a similar analysis as done on FACs.

Figure 2 shows an example $\Delta\mathbf{B}_{\text{EW}}$ time series (panel b) and the corresponding spectrogram (panel c) during a Swarm crossing of the polar region (panel a and polar map). Note that the spectrogram's *y*-axis ranges from 0.05 to 5 Hz. The upper limit corresponds to the maximum frequency intended to avoid aliasing in the sub-sampled data (10 Hz). $\Delta\mathbf{B}_{\text{EW}}(t)$ shows that magnetic field perturbations occur in the vicinity of the auroral region (approximately 68°–80° MLat) (panels a and b). Power intensification in the $\Delta\mathbf{B}_{\text{EW}}$ power spectral density (panel c) expresses the presence of fluctuations in $\Delta\mathbf{B}_{\text{EW}}(t)$, especially at low frequencies (<0.5 Hz). The dominance of such low frequencies reveals that the power spectral density of $\Delta\mathbf{B}_{\text{EW}}$ mostly features relatively large spatial scale structures (15–150 km).

We eventually calculate the $\Delta\mathbf{B}_{\text{EW}}$ spectral power by integrating the power spectral density over three different frequency ranges in the spacecraft frame of reference: 0.05–0.5 Hz, 0.1–1 Hz, and 2.5–5 Hz. Panel d of Figure 2 shows the three corresponding power time series in cyan, orange and green, respectively. Note that if all observed magnetic fluctuations varied only in space, these frequency bands would respectively correspond to spatial scales of approximately 15–150 km, 7.5–75 km, and 1.5–3 km (see Section 4 for further discussion on this matter). Nevertheless, this conversion from frequency to spatial scale assumes periodic structures. If localized small-scale fluctuations are present in the magnetic field, a simple Fourier analysis might result in a broadband frequency spectrum, making it challenging to associate specific frequencies with particular spatial scales. Hence, when

21699402, 2024, 2, Downloaded from https://agupubs.onlinelibrary.wiley.com/doi/10.1029/2023JA032191 by UNIVERSITY OF BERGEN, Wiley Online Library on [07/02/2024]. See the Terms and Conditions (https://onlinelibrary.wiley.com/terms-and-conditions) on Wiley Online Library for rules of use; OA articles are governed by the applicable Creative Commons License

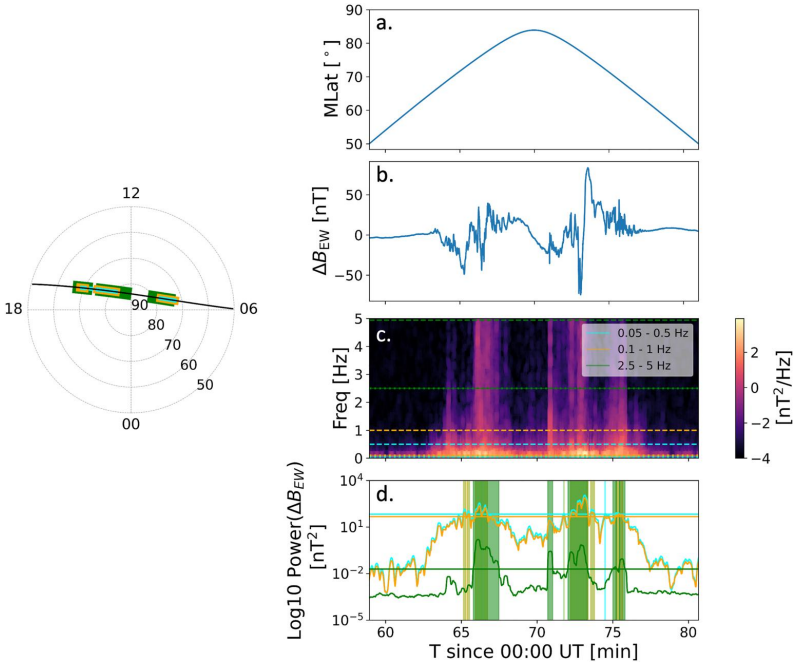

Figure 2. Example disturbed magnetic field identification based on $\Delta\mathbf{B}_{EW}$ time series from one northern polar region crossing by Swarm A on the 25th of September 2014, between 00:58:55 and 01:21:00 UT. Left: The spacecraft orbit is shown in black on an Apex magnetic latitude (MLat)—local time grid. Right: (a) MLat of the satellite orbit during this pass. (b) Associated $\Delta\mathbf{B}_{EW}$ time series. (c) $\Delta\mathbf{B}_{EW}$ spectrogram with the frequency on the *y*-axis and time on the *x*-axis. The horizontal lines correspond to the lower (dotted) and upper (dashed) limits of different frequency ranges: 0.05–0.5, 0.1–1, and 2.5–5 Hz in cyan, orange and green respectively. (d) $\Delta\mathbf{B}_{EW}$ integrated over each of the previously mentioned frequency bands. The horizontal lines show the threshold for the detection of disturbed magnetic field, within each frequency band. The different regions of detected disturbed magnetic field are shown shaded in cyan, orange or green, depending on the frequency band. The identified regions of disturbed magnetic field are also highlighted in the same color along the satellite orbit (left). This figure can be compared with Figure 2 in Decotte et al. (2023) and Kilcommons et al. (2017).

focusing on the spatial scale of magnetic field structures, a wavelet analysis would be a more suitable approach, especially in the presence of significant localized fluctuations in the signal. In the present study, however, the spatial scales are given for information purposes only and are not the main focus.

Performing this procedure for the ≈195,000 polar passes identified between 2014 and 2021 for Swarm A and B (in both hemispheres) results in about 10^8 measurements that are saved into a database together with their corresponding time and location, to be used in our subsequent statistical analysis.

2.4. Power Threshold for Detection of Magnetic Field Fluctuations

We then derive a binary data set that indicates whether portions of $\Delta\mathbf{B}_{EW}$ spectral power estimate, within each of the above-mentioned frequency bands, may be deemed to be associated with magnetic field perturbations or not. To generate such a data set we must define the threshold above which the power estimates are deemed "disturbed magnetic field", and "undisturbed magnetic field" otherwise. This is conceptually similar to the procedure described by Decotte et al. (2023) for producing a binary "aurora/no aurora" time series from DMSP/SSJ electron precipitation measurements. We will discuss how both data sets compare in Section 4.

We choose the magnetic field disturbances detection threshold to correspond to the 75th percentile of the $\Delta\mathbf{B}_{EW}$ spectral power estimate in each frequency band. This yields power thresholds of 69 nT^2, 48 nT^2, and 0.02 nT^2 for

21699402, 2024, 2, Downloaded from https://agupubs.onlinelibrary.wiley.com/doi/10.1029/2023JA032191 by UNIVERSITY OF BERGEN, Wiley Online Library on [07/02/2024]. See the Terms and Conditions (https://onlinelibrary.wiley.com/terms-and-conditions) on Wiley Online Library for rules of use; OA articles are governed by the applicable Creative Commons License

the 0.05–0.5 Hz, 0.1–1 Hz, and 2.5–5 Hz frequency bands, respectively. More details about the selection of power limits are given in Section 3.1. We will also show that the choice of threshold in a given frequency band has only a minor influence on the conclusions we draw in this study.

Figure 2d shows the integrated power spectral density in the 0.05–0.5 Hz, 0.1–1 Hz, and 2.5–5 Hz frequency bands in cyan, orange, and green, respectively. The threshold used in each frequency band is represented by the horizontal line of the same color, such that the spectral power of $\mathbf{\Delta B}_{\mathrm{EW}}$ constitutes magnetic field perturbations when above that limit. The polar plot at left of Figure 2 shows the latitudinal extent of the portions of $\mathbf{\Delta B}_{\mathrm{EW}}$ spectral power exceeding the detection threshold, depending on the frequency band. It can be seen that the high-frequency magnetic field fluctuations (in green) tend to extend to higher latitudes than the lower-frequency structures (in cyan and orange).

2.5. Disturbed Magnetic Field Occurrence Probability (dBOP)—Probability of Detecting Magnetic Fluctuations in the Auroral Region

Still following Decotte et al. (2023), data points from the "disturbed/not disturbed" magnetic field data set defined in Section 2.4 are binned to an approximately equal-area MLat-MLT grid covering the entire polar regions (>60° | MLat|). The grid cells are organized in rings of width 1° MLat, with 2 cells in the 89°–90° ring and 68 cells in the 50°–51° one. We calculate the probability of detecting disturbed magnetic field in each bin (providing that it contains >200 measurements), by dividing the sum of all observations identified as magnetic field fluctuations by the total number of measurements. In Section 3, we investigate the MLat-MLT distributions of the resulting disturbed magnetic field occurrence probability (dBOP) and its MLT variation under varying external conditions. The MLT profile of dBOP (1D dBOP) is derived by interpolating the probabilities to a regular MLat-MLT grid (0.5° MLat and 8 min MLT resolution) and averaging the gridded values over latitude. We will see that the 1D dBOP gives a better sight of potential spatial asymmetries in the disturbed magnetic field than the complete MLat-MLT distribution of dBOP. Note that both hemispheres are combined in all the dBOP distributions presented in the following study, except for the B_y analysis.

3. Results

In this section, we explore the response of the dBOP to intrinsic parameters such as the frequency band and the threshold for magnetic fluctuation detection. We also investigate how the dBOP behaves with respect to various conditions related to IMF orientation and substorm epochs.

3.1. Variation With Frequency Band and Threshold

Figure 3 shows how the dBOP distribution varies depending on the frequency band and threshold for disturbed magnetic field detection. We emphasize that high (green to yellow) values of dBOP correspond to a high probability of detecting a disturbed magnetic field. We also point out that, in all distributions presented in this paper, the seven most poleward bins have been neglected since the East-West component of the magnetic field perturbation is unstable near the pole.

Figure 3A shows the dBOP distributions obtained within three different frequency bands, with each column corresponding to a given threshold. Figure 3B shows the MLT profiles (1D dBOP) obtained for all three thresholds, within a given frequency range. The power thresholds are given by the 65th (in black), 75th (dark gray) and 85th (light gray) percentiles (from left to right in panel A) of the $\mathbf{\Delta B}_{\mathrm{EW}}$ spectral power estimate in each frequency band. Eventually, Figure 3C shows how the MLT profiles compare between the different frequency bands, using the threshold values corresponding to the 75th percentile. Within a given frequency band, we observe that only the dBOP intensity is affected by the choice of threshold, while the overall distribution morphology is stable. On the other hand, the choice of frequency range can cause major variations in the dBOP distributions, as seen from the maps and the MLT profiles. See Section 4 for a detailed discussion on this topic.

The dBOP distributions obtained from the two lowest frequency bands 0.05–0.5 Hz and 0.1–1 Hz are highly similar in shape and intensity (top two rows in Figure 3A). They both exhibit an oval shape around the magnetic pole. Regarding the latitudinal range, the low-frequency dBOP essentially spreads between 68° and 80° MLat. The 1D dBOP profiles at these frequencies (Figures 3B(a) and 3B(b)) show two peaks in the dawn

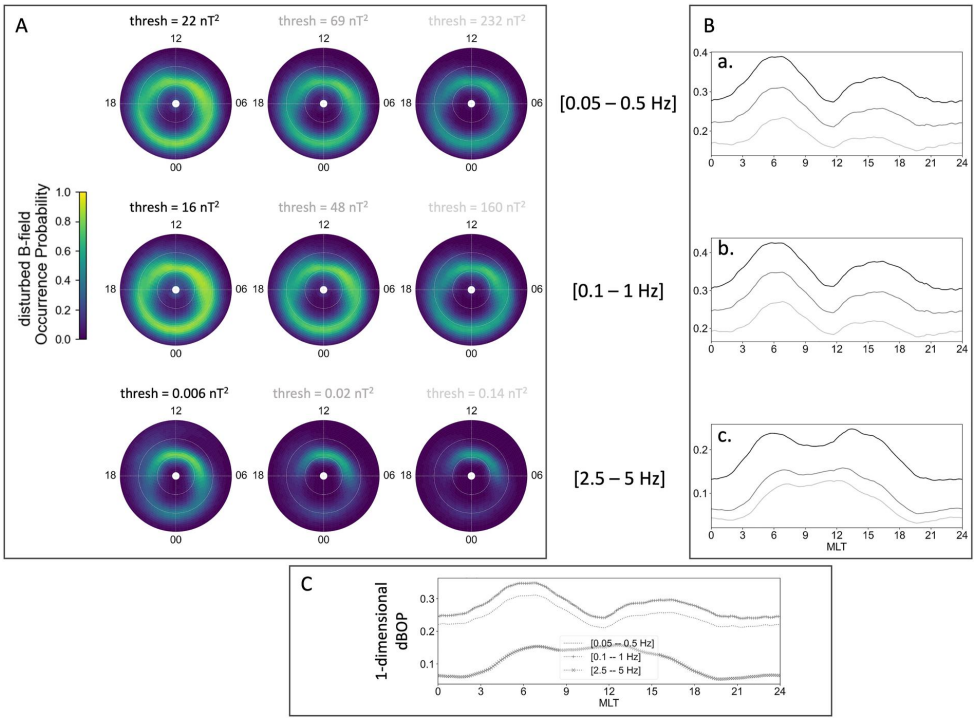

Figure 3. MLat-MLT distributions of distributed magnetic field occurrence probability (dBOP) for various frequency bands and thresholds. Panel (A) the rows correspond to different frequency bands, while the columns illustrate different choices of threshold. From left to right, the thresholds correspond to the 65th (in black), 75th (dark gray) and 85th (light gray) quantiles of the $\Delta\mathbf{B}_{EW}$ spectral power estimate in each frequency band. From top to bottom, the frequency bands are as follows: 0.05–0.5 Hz, 0.1–1 Hz and 2.5–5 Hz. Panel (B) the line plots (a) correspond to the 1D dBOP derived for all three thresholds (in black, dark and light gray), in the frequency band 0.05–0.5 Hz. Each of the three frequency bands. Same for (b) and (c) which correspond to 0.1–1 Hz and 2.5–5 Hz, respectively. Panel (C) 1D dBOP derived for the medium-value threshold (second column in panel A, dark gray) in all three frequency bands. The top two similar profiles correspond to the low-frequency bands and the bottom profile to the high-frequency band. All distributions presented in this paper span over 60–90°|MLat| , and result from a combination of Swarm A and B observations from both hemispheres (except for the B_y analysis).

(5–8 MT) and dusk (14–18 MLT) sectors, with an asymmetry between these two regions such that the disturbed magnetic field is more often detected at dawn. In contrast, the dBOP distribution obtained from the highest frequency band 2.5–5 Hz (bottom row in Figures 3A and 3B(c)) exhibits a smaller oval, in particular narrower than the low-frequency dBOP distributions along the dawn-dusk axis. The high-frequency dBOP also has a different asymmetric pattern, with an overall dayside prominence, and a much fainter presence on the nightside. While the dayside peak can be decomposed into two spikes of approximately the same magnitude (at 6 and 15 MLT) in the lower threshold distribution (black profile in Figure 3B(c)), it tends to flatten for higher thresholds (in dark and light gray). At such frequencies, and independent of its exact shape, the peak on the dayside probably indicates the importance of directly driven processes as part of the dynamic MI coupling. We discuss this further in Section 4.

Due to the similarity between the two low-frequency bands 0.05–0.5 Hz and 0.1–1 Hz, we pursue our study by restraining the analysis to the 0.1–1 Hz and 2.5–5 Hz intervals. We hereafter refer to these frequency bands respectively as the low- and high-frequency bands. Furthermore, since the choice of threshold for the detection of disturbed magnetic field seems to have no significant influence on the dBOP distribution shape, we will use the intermediate (75th percentile) threshold values 48 and 0.02 nT^2 for the 0.1–1 Hz and 2.5–5 Hz frequency bands, respectively.

21699402, 2024, 2, Downloaded from https://agupubs.onlinelibrary.wiley.com/doi/10.1029/2023JA032191 by UNIVERSITY OF BERGEN, Wiley Online Library on [07/02/2024]. See the Terms and Conditions (https://onlinelibrary.wiley.com/terms-and-conditions) on Wiley Online Library for rules of use; OA articles are governed by the applicable Creative Commons License

21699402, 2024, 2, Downloaded from https://agupubs.onlinelibrary.wiley.com/doi/10.1029/2023JA032191 by UNIVERSITY OF BERGEN, Wiley Online Library on [07/02/2024]. See the Terms and Conditions (https://onlinelibrary.wiley.com/terms-and-conditions) on Wiley Online Library for rules of use; OA articles are governed by the applicable Creative Commons License

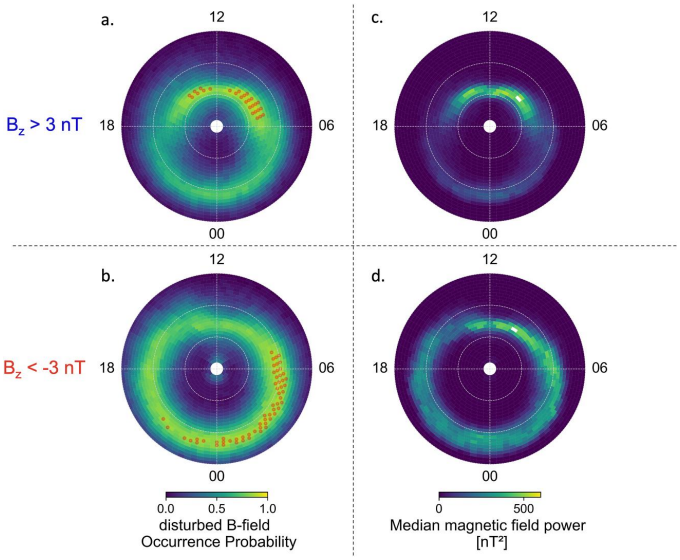

Figure 4. Distributions of low-frequency [0.1–1 Hz] magnetic field fluctuation occurrence probability (left, maps (a) and (b) and median magnetic field power (right, maps (c) and (d) for positive (top, maps (a) and (c) and negative (bottom, maps (b) and (d) interplanetary magnetic field B_z. The red dots on the left maps indicate bins with distributed magnetic field occurrence probability (dBOP) value > 0.85 (low-frequency dBOP peak).

3.2. Comparison With Average Power

Figure 4 (low-frequency) and Figure 5 (high-frequency) show the dBOP (left, panels a and b) and the median power distributions (right, panels c and d) for northward (top) and southward (bottom) IMF. The peak in dBOP is defined as dBOP values exceeding 0.85 (low-frequency) or 0.5 (high-frequency) and is shown as red dots on the left maps. The comparison between both types of distributions for given geomagnetic conditions reveals that the dBOP behaves distinctly from the average power.

Figure 4 shows that, at low frequencies, the dBOP exhibits a dayside peak (7–15 MLT) in the low geomagnetic activity (B_z positive) distribution (panel a). The low-frequency average power (panel c) also displays a clear peak on the dayside but the rest of the oval is much fainter than the dBOP everywhere else. Still at low frequency, increased geomagnetic activity (B_z negative) leads both types of distributions to expand to lower latitudes on the nightside. In terms of intensity, the dBOP (panel b) peaks all the way from pre-midnight to the dawn sector (22–8 MLT) during such disturbed times. The increase in the average power (panel d) is significant in all MLT sectors from 17 to 7, but the dawn-to-noon region remains the most intense. Thus, the peak sector in dBOP overlaps with the average power peak only in a narrow region around 6–7 MLT.

Distinct observations can be made from Figure 5 at high frequencies. Here, the dBOP and average power distributions vary in the same fashion. In particular, they are globally very faint in all MLT sectors except on the dayside, for both quiet (panels a and c) and active times (panels b and d). The effect of enhanced geomagnetic activity is scarcely visible, resulting in broader but still very spread dBOP and average power distributions, with narrower regions of peak intensity compared to lower geomagnetic activity. As opposed to the low-frequency distributions, the peak regions in the dBOP at high frequencies and in the average power are coincident and located in the 8–13 MLT region.

The correlation between high-frequency dBOP and average power might be another indication that the dBOP, at such frequencies, is an image of the strong/dynamic coupling between the magnetosphere and ionosphere. With this assumption, the dayside peak in the dBOP would then reflect a region in the ionosphere that is directly coupled to the solar wind. On average, changes in the IMF and the subsequent reconnection at the magnetopause

21699402, 2024, 2, Downloaded from https://agupubs.onlinelibrary.wiley.com/doi/10.1029/2023JA032191 by UNIVERSITY OF BERGEN, Wiley Online Library on [07/02/2024]. See the Terms and Conditions (https://onlinelibrary.wiley.com/terms-and-conditions) on Wiley Online Library for rules of use; OA articles are governed by the applicable Creative Commons License

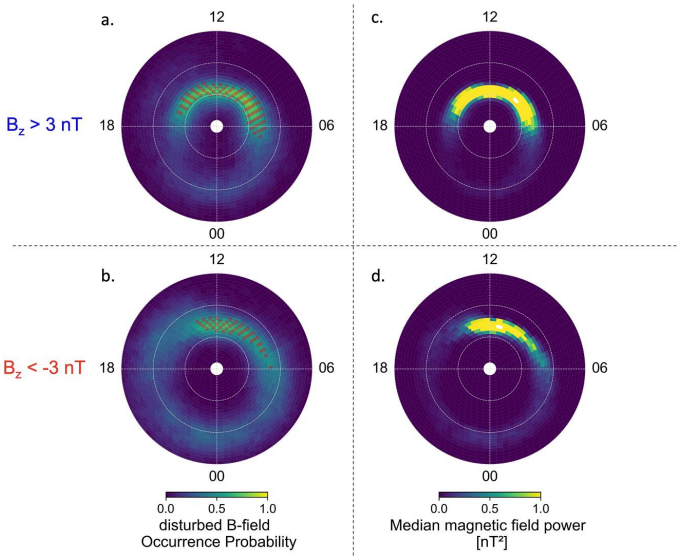

Figure 5. Similar as Figure 4, but for high frequencies [2.5–5 Hz]. The red dots on the left maps indicate bins with distributed magnetic field occurrence probability (dBOP) value > 0.5 (high-frequency dBOP peak).

trigger magnetic field activity in a definite region on the dayside, thus resulting in a peak in both the dBOP at high frequencies and the average magnetic field power. During increased geomagnetic activity ($B_z < 0$), the forcing at the magnetosphere is stronger but the region of coupling on the dayside becomes more variable and results in a larger but more diffuse region of disturbed magnetic field, as seen in both types of distributions. The same phenomenon applies to the nightside, where, on average, reconnection occurs over a much larger region in space —compared to the dayside—thus resulting in a faint distribution in both the high-frequency dBOP and the average magnetic field power.

Note that the difference between dayside and nightside in the dBOP could also be attributed to a variation in solar illumination and associated conductivity. Neubert and Christiansen (2003), for example, have shown that current densities are enhanced in the sunlit ionosphere due to higher electrical conductivity.

3.3. Variation With IMF Bz

Figure 6 (low-frequency) and Figure 7 (high-frequency) show the variation of dBOP with solar wind driving. Both MLat-MLT distributions (maps) and MLT profiles (line plot) of the dBOP are shown. The maps are a repetition of the distributions presented in Figures 4 and 5, hence we mostly focus on the analysis of the 1D dBOP in this paragraph.

Figure 6 highlights the asymmetric pattern in the low-frequency dBOP distributions. During quiet times (left map, blue profile), there is an overall dayside prominence with two peaks at around 6 and 16 MLT. The distribution peaks in the dawn sector (4–7 MLT) and reaches a minimum in the dusk-to-midnight region (21–00 MLT). An increase in solar wind driving (right map, red profile) leads to a broadening of the dBOP oval as well as its expansion to lower latitudes. Such change in the dBOP is particularly visible in the nightside (18–6 MLT). As a consequence, the relative asymmetry between dawn and dusk is dramatically reduced for negative B_z, although the dawn sector still dominates the distribution. Figure 7, on the other hand, does not exhibit any specific asymmetric pattern between the dawn and dusk sectors. It shows that the dBOP distributions at high frequencies are dominated by the dayside sector (particularly the cusp region), independent of the sign of B_z. Enhanced solar wind driving results in an overall larger but more diffuse distribution, as well as a shift to lower latitudes for the prenoon-cusp sector. Additionally, an increase in the geomagnetic activity leads to a slight increase of the dBOP

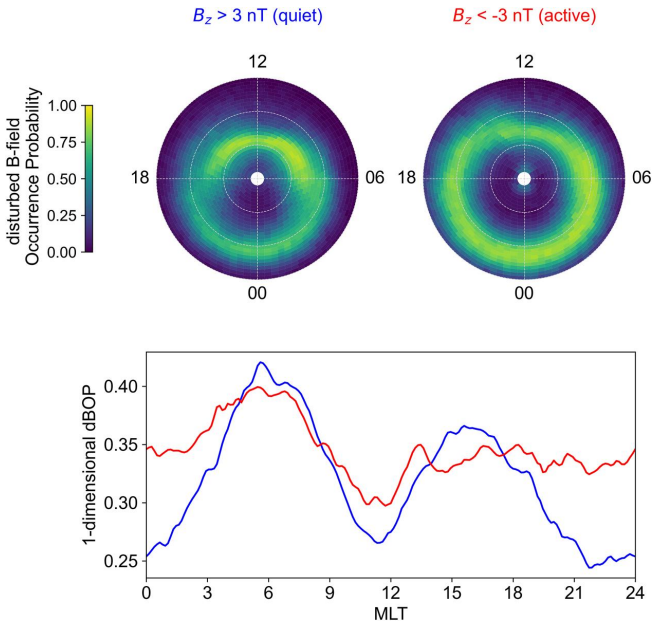

Figure 6. MLat-MLT distributions of low-frequency [0.1–1 Hz] distributed magnetic field occurrence probability (dBOP) (top row) and magnetic local time profiles of 1D dBOP (bottom panel) for interplanetary magnetic field B_z positive (left, blue) and B_z negative (right, red).

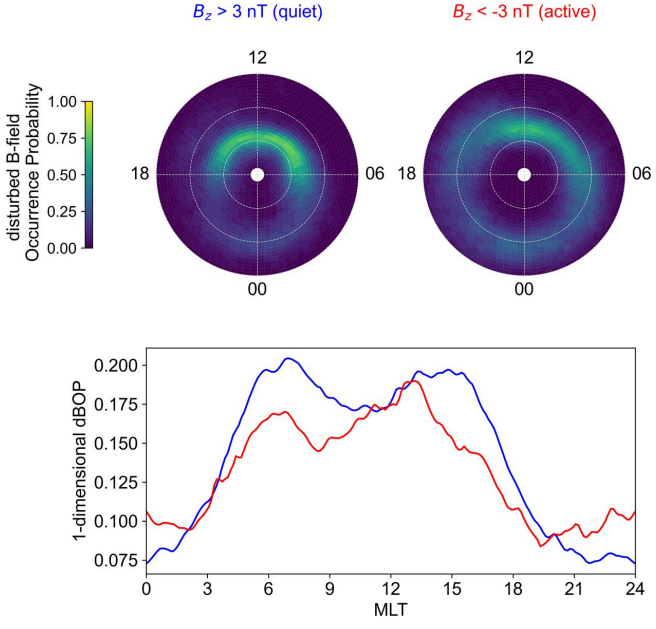

Figure 7. Similar as Figure 6, but for high frequencies [2.5–5 Hz].

21699402, 2024, 2, Downloaded from https://agupubs.onlinelibrary.wiley.com/doi/10.1029/2023JA032191 by UNIVERSITY OF BERGEN, Wiley Online Library on [07/02/2024]. See the Terms and Conditions (https://onlinelibrary.wiley.com/terms-and-conditions) on Wiley Online Library for rules of use; OA articles are governed by the applicable Creative Commons License

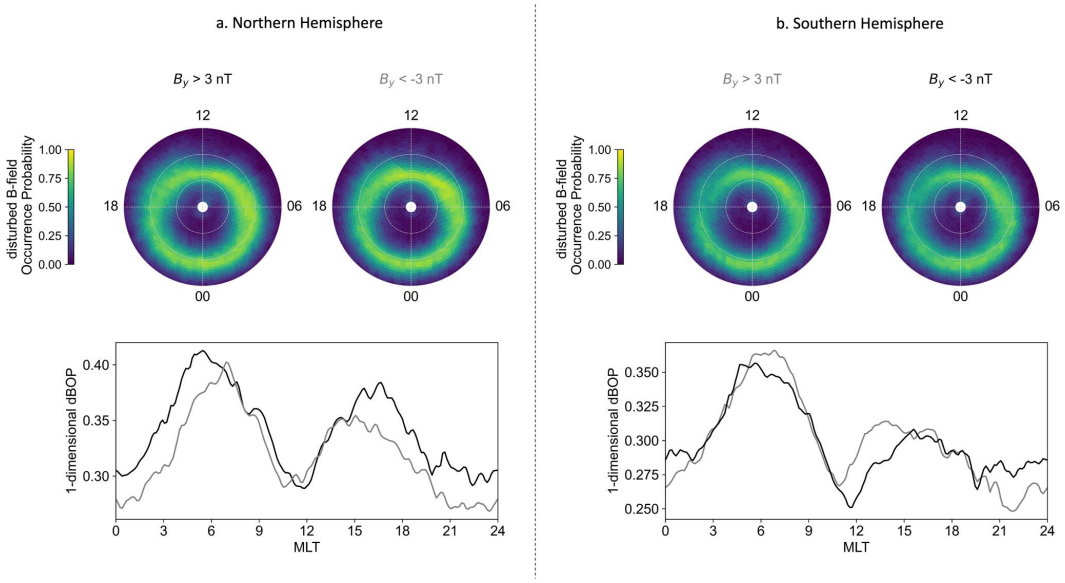

Figure 8. MLat-MLT distributions of low-frequency [0.1–1 Hz] distributed magnetic field occurrence probability (dBOP) and magnetic local time profiles of 1D dBOP for different interplanetary magnetic field B_y orientations, for (a) Northern and (b) Southern Hemispheres. For inter-hemispheric comparison, B_y positive (negative) in the Northern Hemisphere is often assumed to correspond to B_y negative (positive) in the Southern Hemisphere (Hatch et al., 2022).

distribution on the nightside and simultaneously a small decrease on the dayside, which tends to reduce the dayside-nightside asymmetry during such active times ($B_z < 0$). A common feature between low and high frequencies is thus a decrease of the asymmetry in the dBOP distribution during active geomagnetic times, although the asymmetric patterns are different.

3.4. Variation With IMF by

We compare the dBOP distributions (maps and MLT profiles) for different orientations of IMF B_y. Figures 8a and 8b show the low-frequency dBOP variation with B_y for each hemisphere. Figures 9a and 9b present the same analysis but for high frequencies.

The MLT profiles of dBOP in Figure 8 (low-frequency) reveal inter-hemispheric asymmetries: the dBOP distribution for B_y positive in the Northern Hemisphere varies differently than the dBOP for B_y negative in the Southern Hemisphere (black lines), relatively to the dBOP distribution for the opposite B_y (gray lines) in each hemisphere. The difference between North and South mainly lies in the post-midnight (3–5 MLT) and in the postnoon-to-dusk (12–19 MLT) sectors. In the Northern Hemisphere, positive B_y (black line) gives higher values of 1D dBOP compared to B_y negative (gray line) at all MLTs except in the post-noon sector where both distributions are equivalent. In the Southern Hemisphere, negative B_y (black line) gives higher values of 1D dBOP than B_y positive (gray line) only on the nightside (20–3 MLT). In other MLT sectors, distributions of dBOP for both B_y signs are either equal (in the dawn, prenoon and dusk sectors) or the distribution for $B_y > 0$ is greater than the distribution for $B_y < 0$ (6–9 and 11–15 MLT sectors). In terms of intensity, the Southern Hemisphere displays lower values of 1D dBOP than the Northern Hemisphere for both B_y orientations in all MLT sectors, which might have to do with strength differences in the main magnetic field itself. Despite these divergences, the dawn-dusk asymmetry is present in the low-frequency dBOP for both hemispheres and both B_y orientations. However, while it seems to be independent of the B_y sign in the Northern Hemisphere, the asymmetric pattern is slightly reduced for B_y negative (in black), compared to B_y positive (in gray), in the Southern Hemisphere.

21699402, 2024, 2, Downloaded from https://agupubs.onlinelibrary.wiley.com/doi/10.1029/2023JA032191 by UNIVERSITY OF BERGEN, Wiley Online Library on [07/02/2024]. See the Terms and Conditions (https://onlinelibrary.wiley.com/terms-and-conditions) on Wiley Online Library for rules of use; OA articles are governed by the applicable Creative Commons License

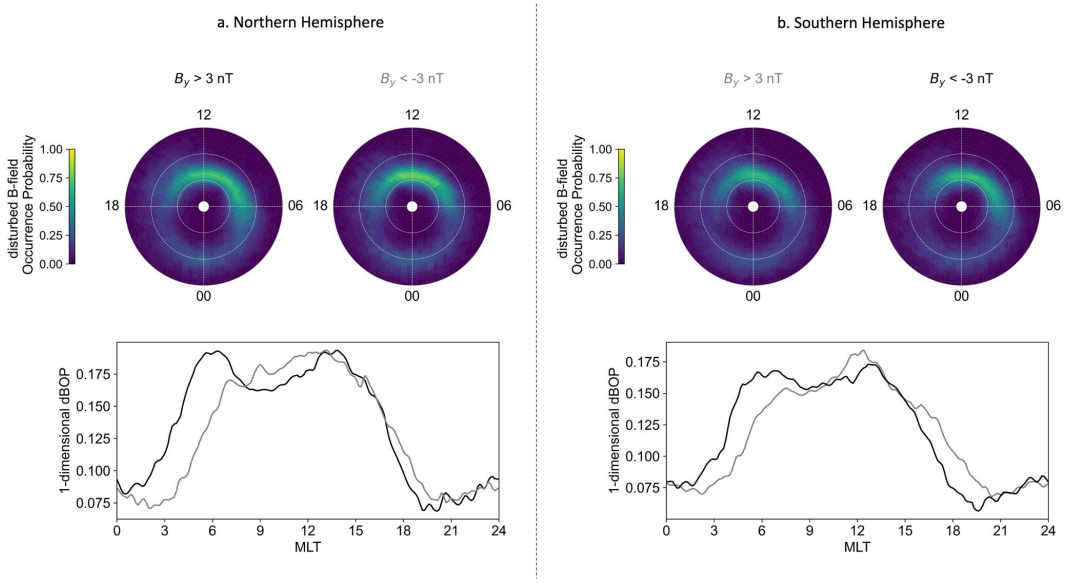

Figure 9. Similar as Figure 8, but for high frequencies [2.5–5 Hz].

Figure 9 shows that the dBOP behavior with B_y orientation at higher frequencies is different from the behavior observed at low frequencies. Here, the 1D distributions obtained for B_y positive and negative in the Northern Hemisphere (Figure 9a) essentially match the distributions for B_y negative and positive in the Southern Hemisphere (Figure 9b). In particular, the MLT profiles of dBOP for both B_y signs are almost identical on the nightside, in both hemispheres. In the Northern Hemisphere, the values of 1D dBOP for positive B_y (in black) exceeds the 1D dBOP obtained for the opposite B_y orientation (in gray) at dawn, and this trend is reversed around the noon region and at dusk. The same applies in the Southern Hemisphere, where the dBOP distribution for negative B_y (in black) also exceeds the distribution obtained for the opposite B_y orientation (in gray) at dawn, with a reversed trend around the noon region and at dusk.

Figures 8 and 9 show that independent of hemisphere or the sign of B_y, the dBOP distributions presented here are relatively similar to the distributions previously described in this study (see Sections 3.1 and 3.3). As opposed to its strong influence on FACs, the effect of B_y orientation on dBOP is thus overall weak as the global shape of dBOP is conserved. In particular, the asymmetric pattern (between dawn and dusk at low frequencies and between dayside and nightside at higher frequencies) remains the main morphological characteristic in the dBOP distributions. We therefore assume the inter-hemispheric differences reported here to have no major consequence on the conclusions we draw in this study (as they mostly have to do with the persistent asymmetric pattern in dBOP), such that both hemispheres can be safely combined in the rest of the analysis.

3.5. Variation With Substorm Epochs

In this section, we aim to determine how the disturbed magnetic field occurrence probability varies throughout the substorm cycle. We use the Ohtani and Gjerloev list of substorm onsets identified from the SuperMAG Maximum westward auroral electrojets strength (SML) index (Ohtani & Gjerloev, 2020).

Figures 10 (low frequencies) and 11 (high frequencies) show the statistical evolution of the dBOP MLat-MLT distribution with the substorm cycle, and the corresponding MLT profiles of 1D dBOP, from 30 min before substorm onset ($t = 0$) up until 30 min after onset (in blue and red, respectively), separated into 15-min intervals.

The dBOP global morphology remains unchanged and similar to the dBOP distributions previously described in this study. In particular, the MLT profiles in Figures 10 and 11 exhibit the usual dawn-dusk asymmetry in the low-

21699402, 2024, 2, Downloaded from https://agupubs.onlinelibrary.wiley.com/doi/10.1029/2023JA032191 by UNIVERSITY OF BERGEN, Wiley Online Library on [07/02/2024]. See the Terms and Conditions (https://onlinelibrary.wiley.com/terms-and-conditions) on Wiley Online Library for rules of use; OA articles are governed by the applicable Creative Commons License

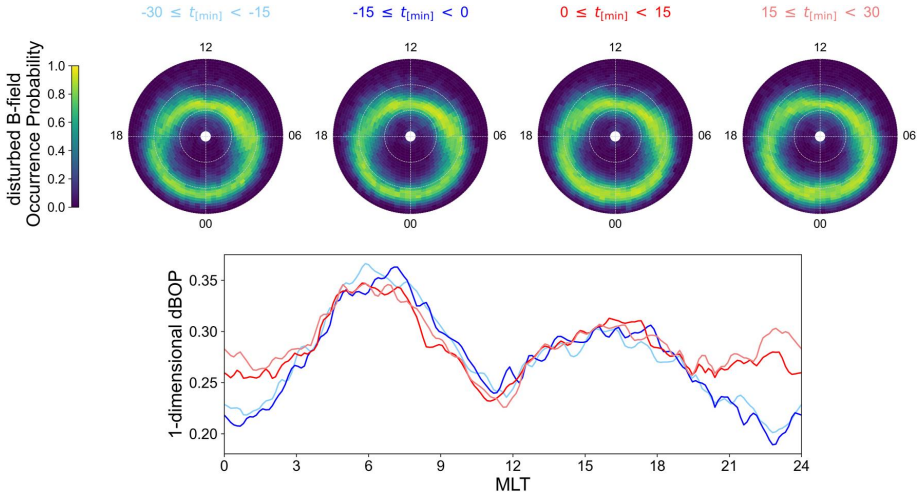

Figure 10. Low-frequency [0.1–1 Hz] distributed magnetic field occurrence probability (dBOP) distributions and magnetic local time profiles of 1D dBOP for four different 15 min-time ranges around substorm onset. From left to right the time ranges are respectively -30 min $\leq t < -15$ min (light blue), -15 min $\leq t < 0$ min (dark blue), 0 min $\leq t < 15$ min (dark red), 15 min $\leq t < 30$ min (light red).

frequency dBOP, and the asymmetry between dayside and nightside in the high-frequency dBOP. In both frequency bands, the influence of substorm phases on these distributions is mainly visible on the nightside. In the pre-midnight sector (21–23 MT), the 1D dBOP distributions indicate a sharp increase in the probability of detecting disturbed magnetic field after substorm onset. This can also be observed in the MLat-MLT distributions (maps) as a small expansion/intensification of the dBOP oval around midnight. The after-onset dBOP then stays higher than before onset from about 21 to 3 MLT, as primarily seen from the MLT profiles. In all other MLT sectors, the dBOP remains unchanged for $t < 0$ and $t > 0$. Despite the significant increase in dBOP on the nightside, the four low-frequency dBOP distributions still peak at dawn and the high-frequency dBOP still

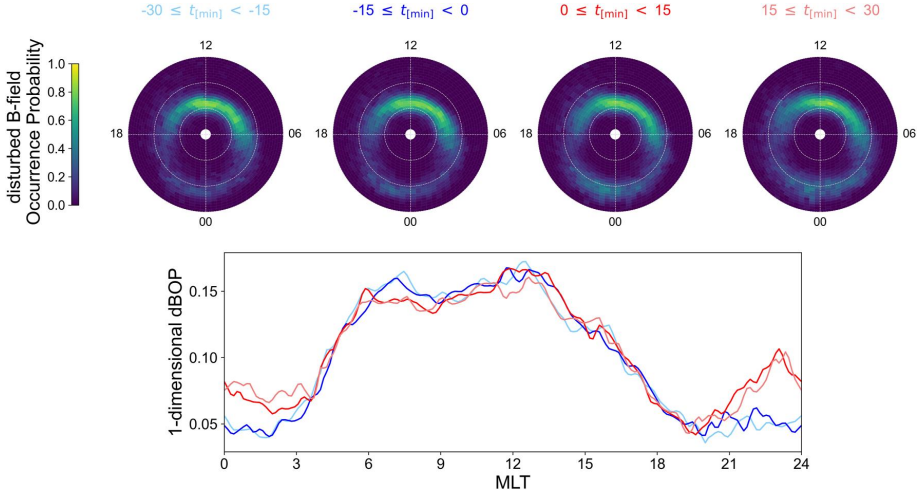

Figure 11. Similar as Figure 10, but for high frequencies [2.5–5 Hz].

21699402, 2024, 2, Downloaded from https://agupubs.onlinelibrary.wiley.com/doi/10.1029/2023JA032191 by UNIVERSITY OF BERGEN, Wiley Online Library on [07/02/2024]. See the Terms and Conditions (https://onlinelibrary.wiley.com/terms-and-conditions) on Wiley Online Library for rules of use; OA articles are governed by the applicable Creative Commons License

21699402, 2024, 2, Downloaded from https://agupubs.onlinelibrary.wiley.com/doi/10.1029/2023JA032191 by UNIVERSITY OF BERGEN, Wiley Online Library on [07/02/2024]. See the Terms and Conditions (https://onlinelibrary.wiley.com/terms-and-conditions) on Wiley Online Library for rules of use; OA articles are governed by the applicable Creative Commons License

presents a broad peak from 6 to 13 MLT, independent of the substorm epoch. Hence substorm onsets tend to reduce the asymmetric pattern in the dBOP distributions, in a similar way as the rise in geomagnetic activity associated with southward IMF B_z for example (see Section 3.3).

4. Discussion

We used Swarm $\Delta\mathbf{B}_{\mathrm{EW}}$ measurements to derive MLat-MLT maps of the disturbed magnetic field occurrence probability for different conditions. In this section, we discuss methodology limitations resulting from the ambiguity between spatial and temporal variations as it is complex to determine whether the spacecraft is moving through quasi-static structures or if the structures themselves are dynamic. We also compare the dBOP with auroral boundaries derived from FAC signatures and finally discuss the connection between the dBOP and the auroral oval as derived from precipitating electrons.

4.1. Interpretation of Magnetic Field Variations in the Satellites' Moving Frame of Reference

We found important discrepancies between the low- and high-frequency dBOP distributions. At high frequencies, the dBOP distributions essentially highlight the dayside and, to a lesser extent, the midnight sector. As they directly map to active regions in the magnetosphere (regions of reconnection on the dayside and depolarization on the nightside), such sectors are subject to strong forcing when there is a stress imbalance between the ionosphere and the magnetosphere. Thereby, high-frequency magnetic field perturbations are commonly associated with dynamic FACs (typically Alfvén waves), which are generated in response to the tension on the magnetic field lines. On the other hand, the low-frequency dBOP is generally more spread over all MLTs. Indeed, low-frequency magnetic field perturbations indicate a more balanced stress between the ionosphere and magnetosphere, associated with quasi-steady-state FACs. Such perturbations are expected to reflect the average ionospheric current patterns, such as those described by the Average Magnetic Field and Polar Current System (AMPS) model (Laundal et al., 2018).

Consequently, the low-frequency dBOP is likely to relate to large-scale spatial variations in magnetic field structures. However, we emphasize that the magnetic field disturbances measured by Swarm cannot be unambiguously identified as either spatial or temporal variations. This is due to the discrepancy between the Doppler-shifted frequency of the wave observed in the satellite reference frame and the wave frequency in the plasma reference frame (Chaston et al., 2004; Stasiewicz et al., 2000). Furthermore, even in an ideal quasi-static scenario, it is challenging to assert whether the detected variations are purely spatial or not. The reason for that is that we have no information about the orientation of the current sheet the spacecraft is flying through. For example, for satellite orbits that do not cross circles of latitude perpendicularly, a structure oriented east-west in magnetic coordinates will take longer to traverse and appear as lower frequencies (larger in space) than the same structure if crossed perpendicularly. This bias toward low frequencies might occur more often in the Southern Hemisphere than in the Northern Hemisphere due to the wider orbital plane in magnetic coordinates caused by the offset between magnetic and geographic poles—this offset being larger in the South.

4.2. Comparison With Existing Studies

In an interesting study Neubert and Christiansen (2003) derived small-scale FACs in the polar ionosphere from space-based vector magnetic field observations. The current structures they explore are predominantly located in the cusp, with spatial scales as small as 600 m, surpassing the smallest scales resolved in our study (1.5 km). We nonetheless emphasize that the high-frequency dBOP distributions presented in the present study show the same dependence on IMF B_z (see Section 3.3) as the small-scale FACs determined in Neubert and Christiansen (2003), both in terms of peak location and intensity.

Regarding alternative approaches to a dBOP-like analysis, Wu et al. (2017) also statistically calculated distributions of magnetic power as a function of MLT from Swarm measurements. One notable aspect of their work is the organization of their results according to coincidence with Region 1 (high-) and Region 2 (low-latitude) FACs. In contrast, our 1D dBOP does not allow for differentiation between high and low latitudes. This prevents an accurate comparison with their study. We nevertheless point out that their distributions of "high-frequency" (spacecraft-frame frequencies in the range 0.0163–0.5 Hz) magnetic perturbations co-located with R1 currents peak at dawn and dusk in a similar fashion as our "low-frequency" (0.1–1 Hz) dBOP (e.g., Figure 7b in Wu et al., 2017).

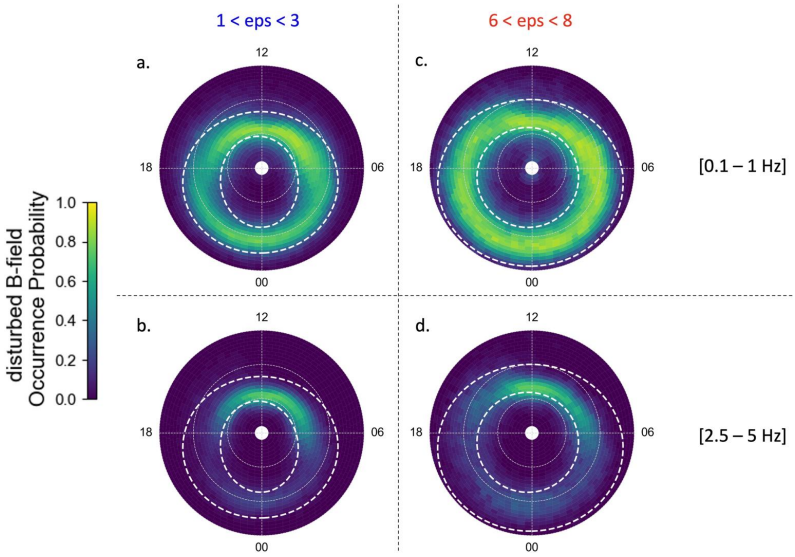

Figure 12. Low- [0.1–1 Hz] (top, maps (a) and (c) and high-frequency [2.5–5 Hz] (bottom, maps (b) and (d) distributed magnetic field occurrence probability distributions for low (left, maps (a) and (b) and high (right, maps (c) and (d) solar wind driving based on two different ranges of the Newell coupling function; namely [1–3] and [6–8]. Auroral oval boundaries—as derived from the Xiong et al. (2014) model—are shown as the white dashed line on top of each distribution and correspond to an epsilon value of 2.5 (low solar wind driving, left) and 5.45 (high solar wind driving, right) respectively.

Another intriguing study is that of Wu et al. (2020), who have derived a statistical distribution of ionospheric Alfvén waves based on Swarm observations, establishing connections with nightside FACs and auroral arc systems. Their approach significantly differs from ours, making a comprehensive comparison between both studies challenging. Notably, they primarily focus on the nightside, and the frequency band used in their methodology encompasses both our low- and high-frequency dBOP. Eventually, their emphasis is on standing Alfvén waves. However, they interestingly suggest that Alfvénic fluctuations—what we think corresponds to our high-frequency dBOP—are typically found in the higher-latitude portion of the auroral region.

We now compare our dBOP distributions with the Xiong and Lühr auroral oval boundaries (Xiong & Lühr, 2014) which are derived from small and medium-scale CHAMP FAC signatures. The Xiong and Lühr (2014) model is such that the position of the poleward and equatorward boundaries are fitted by ellipses that are parameterized by the Newell coupling function (merging electric field), which quantifies the solar wind input into the magnetosphere (Newell et al., 2007). Figure 12 shows the low- (panels a and c) and high-frequency (panels b and d) dBOP distributions for low (panels a and b) and high (panels c and d) solar wind driving conditions, with the modeled boundaries plotted on top (white dashed). Note that Xiong and Lühr (2014) used a time-integrated version of the merging electric field (Equation 2 in their paper), while our dBOP distributions are simply derived from the original Newell coupling function (Equation 1 in the same paper). As a first approximation, these figures indicate a good agreement between dBOP and Xiong et al. (2014) auroral boundaries, as the regions of intense dBOP (>0.6) are plainly enclosed by the boundaries. At low frequencies, in particular, the correspondence is excellent (Figures 12a and 12c). At high frequencies, the boundaries tend to delimit a much larger oval than the dBOP, but still give an approximate idea of the location of the high-frequency dBOP oval (Figures 12b and 12d). Moreover, the modeled boundaries exhibit a modest dawn-dusk asymmetry. This is marginally visible along the 6–18 MLT meridian, and more evident when looking along the ∼9–21 MLT meridian. Although less pronounced than the asymmetry in the corresponding dBOP distributions, this is another indication that the auroral oval boundaries derived by Xiong et al. (2014) and the dBOP display similar features.

21699402, 2024, 2, Downloaded from https://agupubs.onlinelibrary.wiley.com/doi/10.1029/2023JA032191 by UNIVERSITY OF BERGEN, Wiley Online Library on [07/02/2024]. See the Terms and Conditions (https://onlinelibrary.wiley.com/terms-and-conditions) on Wiley Online Library for rules of use; OA articles are governed by the applicable Creative Commons License

21699402, 2024, 2, Downloaded from https://agupubs.onlinelibrary.wiley.com/doi/10.1029/2023JA032191 by UNIVERSITY OF BERGEN, Wiley Online Library on [07/02/2024]. See the Terms and Conditions (https://onlinelibrary.wiley.com/terms-and-conditions) on Wiley Online Library for rules of use; OA articles are governed by the applicable Creative Commons License

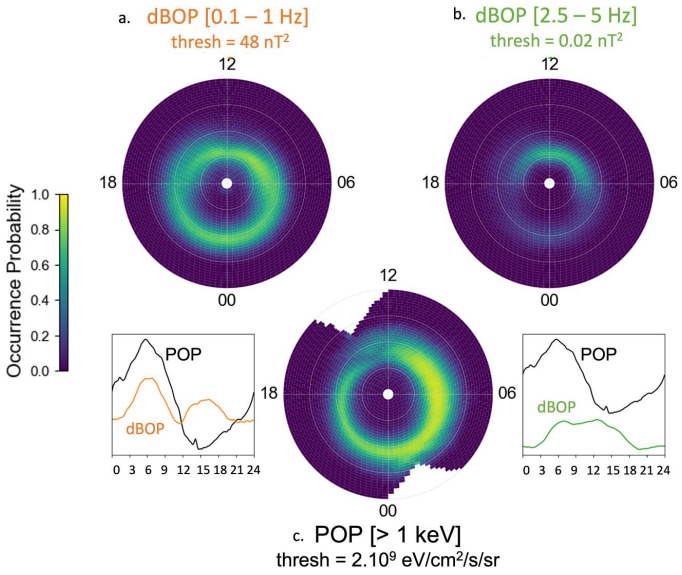

Figure 13. Comparison between distributed magnetic field occurrence probability (top maps) at low (left, map a, orange profile) and high (right, map b, green profile) frequency, and precipitation occurrence probability (bottom, map c, black profile). Both types of distributions are presented over the same latitudinal range $50° \leq |\text{MLat}| \leq 90°$.

Through this non-exhaustive comparative analysis with some relevant studies, we have established the significance of our study, despite its limitations. Notably, we demonstrated a relatively good match between dBOP distributions and the modeled boundaries derived by Xiong et al. (2014). In particular, the low-frequency dBOP adequately captures where the auroral zone FACs are located. The rest of the discussion focuses on the relation between dBOP and precipitation auroral oval.

4.3. Relation With the Auroral Oval—Magnetic Field Version of the Precipitation Occurrence Probability

In a previous study, we derived the electron POP from precipitating electron energy flux measurements at high latitudes (DMSP/SSJ) (Decotte et al., 2023). We established a direct connection between the electron precipitation and the probability of observing aurora by setting an energy flux threshold above which the electron energy flux (in the energy range 1–30 keV) is assumed to result in auroral features (Kilcommons et al., 2017). One of the main findings from the POP study was the asymmetric pattern of the auroral occurrence oval, with a persistent preference for the dawn side compared to dusk. In the present study, we follow a similar method to derive the dBOP, which quantifies the probability of detecting magnetic field fluctuations in space above the polar region. As described in Section 2, the magnetic field spectral power is classified as either "disturbed" or "undisturbed" based on the examination of magnetic field perturbations in different frequency bands. As a first-order approximation, we showed that the dBOP exhibits an oval shape around the magnetic poles, revealing asymmetries between MLT sectors. These similarities motivate the investigation of a possible relationship between dBOP and POP. Therefore, while we performed the analysis without any assumption related to the precipitation auroral oval (see Section 3), this section is an attempt to explain our dBOP distributions in the context of auroral precipitation.

Figure 13 shows how the dBOP MLat-MLT distributions at low (map a) and high (map b) frequencies compare to the POP (map c), using our entire data sets (no specific selection regarding geomagnetic conditions). The corresponding MLT profiles are also shown, with the 1D low- and high-frequency dBOP in orange and green on the bottom panels at left and right, respectively. The 1D POP is plotted on top of each panel as the black line. We emphasize that the local time coverage is one major difference between POP and dBOP distributions. While

21699402, 2024, 2, Downloaded from https://agupubs.onlinelibrary.wiley.com/doi/10.1029/2023JA032191 by UNIVERSITY OF BERGEN, Wiley Online Library on [07/02/2024]. See the Terms and Conditions (https://onlinelibrary.wiley.com/terms-and-conditions) on Wiley Online Library for rules of use; OA articles are governed by the applicable Creative Commons License

DMSP (POP) does not cover the postnoon and postmidnight sectors, Swarm data (dBOP) have the benefit of relatively even coverage of all local times during all seasons (Lühr et al., 2019).

On the one hand, the ovals revealed by the low-frequency dBOP (Figure 13a) and the POP (Figure 13c) exhibit similarities in shape and location - especially at the poleward boundary—such that the preferential MLat-MLT region for magnetic fluctuations and the preferred region for auroral electron precipitation seem to be, at first order, related. Although comparable, both ovals have different latitudinal extents, with overall smaller 1D dBOP amplitudes (MLT profiles) compared to the POP. This feature is well identified by the comparison plot between the dBOP and POP MLT profiles (bottom left panel of Figure 13), which also highlights the weaker dawn-dusk asymmetry in the dBOP (in orange) compared to the POP (in black). On the other hand, dBOP (Figure 13b) and POP (Figure 13c) significantly differ at higher frequencies. There is no longer dawn-dusk asymmetry in the dBOP oval at such frequencies, only a broad peak on the dayside (6–16 MLT), with very faint probabilities everywhere else. As a consequence, the dominant morphological patterns in dBOP and POP are highly contrasting in these conditions, as indicated by the associated MLT profiles (bottom right panel of Figure 13, dBOP in green and POP in black).

We also looked at the response of the dBOP distributions to the level of geomagnetic activity (orientation of IMF B_z and time relative to substorm epoch, see Sections 3.3 and 3.5) and found that, independent of the frequency band, the MLT asymmetry is decreased during active times, due to a considerable enhancement in the dBOP in the nightside sector. This tendency is also observed with the dawn-dusk asymmetry in the POP distributions in Decotte et al. (2023). We emphasize that although the variation of geomagnetic activity impacts the degree of asymmetry in the dBOP and POP distributions in a similar fashion (the more active, the less asymmetric), the asymmetry in the dBOP is reduced to a larger extent than the POP during disturbed geomagnetic times. A quick comparison between the POP and dBOP responses to a southward turning of the IMF or to substorm onset shows that there is a relative lack of response of the POP, while the dBOP distributions are more impacted by such increased activity (greater nightside activation). This partly explains the larger asymmetric pattern in the POP, compared to the dBOP.

In Decotte et al. (2023), we proposed a theory to explain the dawn-dusk asymmetry observed in the POP. The argument relies on a fluid description in which we assume a topological mapping between the auroral oval and the magnetospheric plasma sheet, such that variations in the amount of closed magnetic flux induce similar variations in the auroral region. We showed that the Earth's corotation influence on the plasma convection pattern could be partly responsible for the auroral oval asymmetric shape. Since the low-frequency dBOP and the POP appear to be analogous, this approach could still be valid and partially explain why the dBOP morphology is dominated by an asymmetric pattern between the dawn and dusk sides of the auroral region. In particular, connecting the dBOP to this perspective fits the idea that the auroral oval's shape is not only regulated by energetic precipitation but also depends on the magnetic coupling between the magnetosphere and ionosphere. Moreover, in this picture, it is expected that low- and high-frequency dBOP behave in a different manner. We showed that at high frequencies the dBOP mainly reflects ionospheric regions that are related to dynamic changes in the magnetosphere. These regions are not influenced by the Earth's rotation, unlike the large-scale plasma convection associated with the more steady MI coupling. This could consequently explain the lack of dawn-dusk asymmetry in the high-frequency dBOP.

Kilcommons et al. (2017) have produced maps of the large-scale FACs derived from DMSP magnetometer (SSM) data and compared where the R1 and R2 current systems lie relative to the electron precipitation boundaries, as derived from DMSP SSJ data. They found a dawn-dusk asymmetry in the FAC location, with higher latitude FACs in the dawn region compared to dusk. This latitudinal feature compares well with our low-frequency dBOP distributions derived for different levels of geomagnetic activity (see Sections 3.3 and 3.5). However, the asymmetric pattern they point out doesn't necessarily translate into a wider or more intense dBOP region at dawn. But interestingly enough, they interpret it as related to the extent of the region of strong precipitating electron flux and point to the constantly wider dawn side auroral region. Thereby, this asymmetry in the auroral region is a recurrent pattern in the electron precipitation auroral oval, the FACs and the disturbed magnetic field at low frequency.

Given our understanding of ionospheric electrodynamics, the relationship between low-frequency dBOP (indicative of quasi-steady FACs) and POP (which essentially reflect the large-scale long-term pattern of the auroral oval) aligns coherently. In fact, steady-state FACs are well described by the ionospheric Ohm's law and depend on conductance, which is partly controlled by particle precipitation. Moreover, it is commonly known that auroral precipitation increases the ionospheric conductance in the same region as where the R1/R2 FACs are

21699402, 2024, 2, Downloaded from https://agupubs.onlinelibrary.wiley.com/doi/10.1029/2023JA032191 by UNIVERSITY OF BERGEN, Wiley Online Library on [07/02/2024]. See the Terms and Conditions (https://onlinelibrary.wiley.com/terms-and-conditions) on Wiley Online Library for rules of use; OA articles are governed by the applicable Creative Commons License

located (Milan et al., 2017). It then appears plausible that the low-frequency dBOP may be part of the signature of the diffuse auroral precipitation presented in Decotte et al. (2023). On the other hand, the high-frequency dBOP apparently relates more to wave activity and discrete precipitation. On both dayside and nightside, there is a notable resemblance between the range of MLTs over which the high-frequency dBOP is enhanced and the range of MLTs over which statistical distributions of Alfvén wave Poynting flux and broadband electron precipitation are enhanced (Figures 2–4 in Hatch et al., 2017, ; see also Figures 3 and 4 in Newell et al., 2009). Additionally, for both positive and negative B_y orientations there is a noteworthy resemblance between the high-frequency dBOP and distributions of Alfvén wave Poynting flux and broadband precipitation on the dayside. More generally, it is apparent that the high-frequency dBOP is more similar to distributions of discrete precipitation (either monoenergetic or broadband) than to distributions of diffuse aurora (Newell et al., 2009). It therefore seems relevant to compare the maps from Figure 12 in Newell et al. (2009), showing the occurrence probability of broadband acceleration of precipitating particles, with the dBOP distributions from Figure 7 (B_z analysis). This comparison indicates a good match between the peak regions. During low solar wind driving, the probability of observing broadband acceleration is restrained to two hot spots, the main one being in the dawn sector and the other one in the post-noon MLT region. This compares with the high-frequency dBOP during quiet times ($B_z > 0$), which also peaks in the dawn-to-noon sector, with, however, a high-probability region covering the entire dayside. In particular, an important difference with Newell's electron precipitation maps is the persistence of a dBOP spot around noon. During increased solar wind driving, the same two spots are conserved in Newell's map, with an additional region of increased broadband electron precipitation between 23 and 1 MLT. Additionally, the peak at dawn sees its intensity decreasing while it expands over a larger MLT region, now covering the noon region. The corresponding ($B_z < 0$) high-frequency dBOP shows a diffuse enhancement in all MLT sectors and is globally fainter compared to more quiet times. In these conditions, the highest dBOP probabilities are located in the dawn-to-noon region and in the midnight sector, similar to the broadband aurora. A similar comparison of the high-frequency dBOP maps with the Newell et al. (2009) maps for monoenergetic acceleration occurrence probability (their Figure 11) shows poor correlation.

From this comparison analysis, it is clear that dBOP and POP distributions show significant differences, suggesting that not all features captured in the POP are necessarily captured in the dBOP (and vice versa), highlighting inherent differences between electron precipitation and magnetic field fluctuations. Since both quantities reflect different aspects of the auroral region, it is not expected that they exhibit identical morphologies. Nonetheless, we have shown that the POP and the dBOP, especially at low frequencies, present outstanding similarities such as the morphological asymmetric pattern with the dawn preference, and the response to the geomagnetic conditions. Therefore, the combination of POP and low-frequency dBOP appears promising for gaining valuable insights into the intricate dynamics of the auroral zone.

5. Conclusion

We have presented a method for investigating the auroral region morphology using magnetic field perturbation data from Swarm/VFM. We implemented the dBOP at low 0.1–1 Hz and high 2.5–5 Hz frequencies and used it to assess the probability of observing disturbances in the magnetic field at auroral latitudes, as a function of MLat and MLT. We found the dBOP global morphology to be strongly dependent on the investigated frequency range. At low frequencies, we have pointed out an asymmetric pattern between the dawn and dusk sectors, with a clear tendency for the dBOP to be more pronounced toward dawn (approx 5–8 MLT). At higher frequencies, the asymmetry in the dBOP is strongest near the noon-midnight meridian, with a large predominance of the dayside, especially the post-noon region. We also highlighted the reduced asymmetric pattern during geomagnetically disturbed conditions.

We discussed these results in the context of a previous study (Decotte et al., 2023) about the auroral electron POP and found that the low-frequency dBOP evinces spatial/morphological similarities with the POP. In particular, we observed an asymmetric pattern in both the POP and the low-frequency dBOP, with an unequivocal preference for the dawn-to-noon MLT sector. We also showed that the dBOP morphology is stable with varying detection thresholds and that the dawn-dusk asymmetry appears in all low-frequency distributions independent of IMF orientation and substorm phase, just as in the POP. This suggests that examining the POP, in the energy range 1–30 keV, together with the dBOP, below 1 Hz, could offer valuable insights into the complex dynamics of the auroral zone. More generally, this study indicates that the dBOP can be used as a footprint of the large-scale circulation of plasma and magnetic flux in the magnetosphere.

21699402, 2024, 2, Downloaded from https://agupubs.onlinelibrary.wiley.com/doi/10.1029/2023JA032191 by UNIVERSITY OF BERGEN, Wiley Online Library on [07/02/2024]. See the Terms and Conditions (https://onlinelibrary.wiley.com/terms-and-conditions) on Wiley Online Library for rules of use; OA articles are governed by the applicable Creative Commons License

Data Availability Statement

The Level 1B magnetic Swarm products are directly accessible through the Virtual environments for Earth Scientists (VirES) platform, either via the Swarm web user interface or via the VirES server API using an alternative client such as the Python client (Smith et al., 2023). The OMNI data, including the solar wind data and geomagnetic activity indices, are available on the NASA/GSFC SPDF interface (Papitashvili, 2005).

Acknowledgments
This study was funded by the Trond Mohn Foundation, and by the Research Council of Norway through contracts 223,252/F50 and 300,844/F50. We acknowledge the use of the Python tool VirES for Swarm to access the core data of this study, and we thank J.H. King and N.E. Papitashvili for the multi-sources OMNI data. We acknowledge the use of NASA/GSFC SPDF service to obtain these data. We also acknowledge the substorm timing list identified by the Ohtani and Gjerloev technique (Ohtani & Gjerloev, 2020), the SMU and SML indices (Newell & Gjerloev, 2011); and the SuperMAG collaboration (Gjerloev, 2012).

References

Burrell, A. G., Chisham, G., Milan, S. E., Kilcommons, L., Chen, Y. J., Thomas, E. G., & Anderson, B. (2020). AMPERE polar cap boundaries. *Annales Geophysicae*, *38*(2), 481–490. https://doi.org/10.5194/angeo-38-481-2020

Carbary, J. F., Sotirelis, T., Newell, P. T., & Meng, C. I. (2003). Auroral boundary correlations between UVI and DMSP. *Journal of Geophysical Research*, *108*(A1). https://doi.org/10.1029/2002JA009378

Chaston, C. C., Bonnell, J. W., Carlson, C. W., McFadden, J. P., Ergun, R. E., Strangeway, R. J., & Lund, E. J. (2004). Auroral ion acceleration in dispersive Alfvén waves. *Journal of Geophysical Research*, *109*(A4), 1–13. https://doi.org/10.1029/2003JA010053

Chisham, G., Burrell, A. G., Thomas, E. G., & Chen, Y. J. (2022). Ionospheric boundaries derived from auroral images. *Journal of Geophysical Research: Space Physics*, *127*(7), 1–19. https://doi.org/10.1029/2022JA030622

Christiansen, F., Papitashvili, V. O., & Neubert, T. (2002). Seasonal variations of high-latitude field-aligned currents inferred from Ørsted and Magsat observations. *Journal of Geophysical Research*, *107*(A2). https://doi.org/10.1029/2001JA900104

Cowley, S., & Lockwood, M. (1992). *Excitation and decay of solar-wind driven flows in the magnetosphere-ionosphere system*. Annales Geophysicae.

Decotte, M., Laundal, K. M., Hatch, S. M., & Reistad, J. P. (2023). Auroral oval morphology: Dawn-dusk asymmetry partially induced by Earth's rotation. *Journal of Geophysical Research: Space Physics*, *128*(6), e2023JA031345. https://doi.org/10.1029/2023JA031345

Dombeck, J., Cattell, C., Prasad, N., Meeker, E., Hanson, E., & McFadden, J. (2018). Identification of auroral electron precipitation mechanism combinations and their relationships to net downgoing energy and number flux. *Journal of Geophysical Research: Space Physics*, *123*(12), 10,064–10,089. https://doi.org/10.1029/2018JA025749

Dungey, J. W. (1961). Interplanetary magnetic field and the auroral zones. *Physical Review Letters*, *6*(2), 47–48. https://doi.org/10.1103/PhysRevLett.6.47

Fujii, R., Oguti, T., & Yamamoto, T. (1985). *Relationships between pulsating auroras and field-aligned electric currents* (Vol. 36). National Institute Polar Research Memoirs.

Gillies, D. M., Knudsen, D., Spanswick, E., Donovan, E., Burchill, J., & Patrick, M. (2015). Swarm observations of field-aligned currents associated with pulsating auroral patches. *Journal of Geophysical Research: Space Physics*, *120*(11), 9484–9499. https://doi.org/10.1002/2015JA021416

Gjerloev, J. W. (2012). The SuperMAG data processing technique. *Journal of Geophysical Research: Space Physics*, *117*(A9), A09213. https://doi.org/10.1029/2012ja017683

Hatch, S. M., Haaland, S., Laundal, K. M., Moretto, T., Yau, A. W., Bjoland, L., et al. (2020). Seasonal and hemispheric asymmetries of F region polar cap plasma density: Swarm and CHAMP observations. *Journal of Geophysical Research: Space Physics*, *125*(11). https://doi.org/10.1029/2020JA028084

Hatch, S. M., LaBelle, J., Lotko, W., Chaston, C. C., & Zhang, B. (2017). IMF control of Alfvénic energy transport and deposition at high latitudes. *Journal of Geophysical Research: Space Physics*, *122*(12), 12189–12211. https://doi.org/10.1002/2017JA024175

Hatch, S. M., Laundal, K. M., & Reistad, J. P. (2022). Testing the mirror symmetry of Birkeland and ionospheric currents with respect to magnetic latitude, dipole tilt angle, and IMF B_y. *Frontiers in Astronomy and Space Sciences*, *9*, 958977. https://doi.org/10.3389/FSPAS.2022.958977/BIBTEX

Hatch, S. M., Moretto, T., Lynch, K. A., Laundal, K. M., Gjerloev, J. W., & Lund, E. J. (2020). The relationship between cusp region ion outflows and east-west magnetic field fluctuations at 4,000-km altitude. *Journal of Geophysical Research: Space Physics*, *125*(3), 1–18. https://doi.org/10.1029/2019JA027454

Iijima, T., & Potemra, T. A. (1976). The amplitude distribution of field-aligned currents at northern high latitudes observed by Triad. *Journal of Geophysical Research*, *81*(13), 2165–2174. https://doi.org/10.1029/ja081i013p02165

Iijima, T., & Potemra, T. A. (1978). Large-scale characteristics of field-aligned currents associated with substorms. *Journal of Geophysical Research*, *83*(A2), 599. https://doi.org/10.1029/ja083ia02p00599

Juusola, L., Vanhamäki, H., Viljanen, A., & Smirnov, M. (2020). Induced currents due to 3D ground conductivity play a major role in the interpretation of geomagnetic variations. *Annales Geophysicae*, *38*(5), 983–998. https://doi.org/10.5194/ANGEO-38-983-2020

Kamide, Y., Richmond, A. D., & Matsushita, S. (1981). Estimation of ionospheric electric fields, ionospheric currents, and field-aligned currents from ground magnetic records. *Journal of Geophysical Research*, *86*(A2), 801. https://doi.org/10.1029/ja086ia02p00801

Kauristie, K., Weygand, J., Pulkkinen, T. I., Murphree, J. S., & Newell, P. T. (1999). Size of the auroral oval: UV ovals and precipitation boundaries compared. *Journal of Geophysical Research*, *104*(A2), 2321–2331. https://doi.org/10.1029/1998JA900046

Khazanov, G. V., & Glocer, A. (2020). How magnetically conjugate atmospheres and the magnetosphere participate in the formation of low-energy electron precipitation in the region of diffuse aurora. *Journal of Geophysical Research: Space Physics*, *125*(8), 1–15. https://doi.org/10.1029/2020JA028057

Kilcommons, L. M., Redmon, R. J., & Knipp, D. J. (2017). A new DMSP magnetometer and auroral boundary data set and estimates of field-aligned currents in dynamic auroral boundary coordinates. *Journal of Geophysical Research: Space Physics*, *122*(8), 9068–9079. https://doi.org/10.1002/2016JA023342

King, J. H., & Papitashvili, N. E. (2005). Solar wind spatial scales in and comparisons of hourly Wind and ACE plasma and magnetic field data. *Journal of Geophysical Research*, *110*(A2), 2104. https://doi.org/10.1029/2004JA010649

Kustov, A. V., Lyatsky, W. B., Sofko, G. J., & Xu, L. (2000). Field-aligned currents in the polar cap at small IMF B_z and B_y inferred from SuperDARN radar observations. *Journal of Geophysical Research*, *105*(A1), 205–214. https://doi.org/10.1029/1999ja900428

Laundal, K. M., Finlay, C. C., Olsen, N., & Reistad, J. P. (2018). Solar wind and seasonal influence on ionospheric currents from Swarm and CHAMP measurements. *Journal of Geophysical Research: Space Physics*, *123*(5), 4402–4429. https://doi.org/10.1029/2018JA025387

Laundal, K. M., Østgaard, N., Frey, H. U., & Weygand, J. M. (2010). Seasonal and interplanetary magnetic field-dependent polar cap contraction during substorm expansion phase. *Journal of Geophysical Research*, *115*(11), 1–12. https://doi.org/10.1029/2010JA015910

Laundal, K. M., & Richmond, A. D. (2017). Magnetic coordinate systems. *Space Science Reviews*, *206*(1), 27–59. https://doi.org/10.1007/s11214-016-0275-y

Lühr, H., Kervalishvili, G. N., Stolle, C., Rauberg, J., & Michaelis, I. (2019). Average characteristics of low-latitude interhemispheric and F region dynamo currents deduced from the Swarm satellite constellation. *Journal of Geophysical Research: Space Physics*, *124*(12), 10631–10644. https://doi.org/10.1029/2019JA027419

Milan, S. E., Clausen, L. B., Coxon, J. C., Carter, J. A., Walach, M. T., Laundal, K., et al. (2017). Overview of solar wind–magnetosphere–ionosphere–atmosphere coupling and the generation of magnetospheric currents. *Space Science Reviews*, *206*(1–4), 547–573. https://doi.org/10.1007/s11214-017-0333-0

Nagatsuma, T., Fukunishi, H., Hayakawa, H., Mukai, T., & Matsuoka, A. (1996). Field-aligned currents associated with Alfven waves in the poleward boundary region of the nightside auroral oval. *Journal of Geophysical Research*, *101*(A10), 21715–21729. https://doi.org/10.1029/96JA01797

Nagatsuma, T., Fukunishi, H., & Mukai, T. (1995). Spatial relationships between field-aligned currents and suprathermal electron beams observed at the poleward boundary of the nightside auroral oval. *Journal of Geophysical Research*, *100*(A2), 1625–1637. https://doi.org/10.1029/94JA02440

Neubert, T., & Christiansen, F. (2003). Small-scale, field-aligned currents at the top-side ionosphere. *Geophysical Research Letters*, *30*(19). https://doi.org/10.1029/2003GL017808

Newell, P. T., Feldstein, Y. I., Galperin, Y. I., & Meng, C.-I. (1996). Morphology of nightside precipitation. *Journal of Geophysical Research*, *101*(A5), 10737–10748. https://doi.org/10.1029/95ja03516

Newell, P. T., & Gjerloev, J. W. (2011). Evaluation of SuperMAG auroral electrojet indices as indicators of substorms and auroral power. *Journal of Geophysical Research: Space Physics*, *116*(A12), A12211. https://doi.org/10.1029/2011ja016779

Newell, P. T., Liou, K., Zhang, Y., Sotirelis, T., Paxton, L. J., & Mitchell, E. J. (2014). OVATION Prime-2013: Extension of auroral precipitation model to higher disturbance levels. *Space Weather*, *12*(6), 368–379. https://doi.org/10.1002/2014SW001056

Newell, P. T., Ruohoniemi, J. M., & Meng, C.-I. (2004). Maps of precipitation by source region, binned by IMF, with inertial convection streamlines. *Journal of Geophysical Research*, *109*(A10), 1–20. https://doi.org/10.1029/2004JA010499

Newell, P. T., Sotirelis, T., Liou, K., Meng, C. I., & Rich, F. J. (2007). A nearly universal solar wind-magnetosphere coupling function inferred from 10 magnetospheric state variables. *Journal of Geophysical Research*, *112*(1), 1–16. https://doi.org/10.1029/2006JA012015

Newell, P. T., Sotirelis, T., & Wing, S. (2009). Diffuse, monoenergetic, and broadband aurora: The global precipitation budget. *Journal of Geophysical Research*, *114*(A9). https://doi.org/10.1029/2009JA014326

Ohma, A., Laundal, K. M., Madelaire, M., Hatch, S. M., Gasparini, S., Reistad, J. P., et al. (2023). Excitation and decay of the auroral oval. *Journal of Geophysical Research: Space Physics*. https://doi.org/10.22541/essoar.169447428.84472457/v1

Ohtani, S., & Gjerloev, J. W. (2020). Is the substorm current wedge an ensemble of wedgelets?: Revisit to midlatitude positive bays. *Journal of Geophysical Research: Space Physics*, *125*(9), e2020JA027902. https://doi.org/10.1029/2020JA027902

Papitashvili, N. (2005). NASA/GSFC SPDF OMNI data [Dataset]. OMNIWeb Plus. http://spdf.gsfc.nasa.gov/pub/data/omni/high{_}res{_}omni/

Redmon, R. J., Peterson, W. K., Andersson, L., Kihn, E. A., Denig, W. F., Hairston, M., & Coley, R. (2010). Vertical thermal O+ flows at 850 km in dynamic auroral boundary coordinates. *Journal of Geophysical Research*, *115*(11), 1–10. https://doi.org/10.1029/2010JA015589

Richmond, A. D. (1995). Ionospheric electrodynamics using magnetic Apex coordinates. *Journal of Geomagnetism and Geoelectricity*, *47*(2), 191–212. https://doi.org/10.5636/jgg.47.191

Ritter, P., Lühr, H., & Rauberg, J. (2013). Determining field-aligned currents with the Swarm constellation mission. *Earth Planets and Space*, *65*(11), 1285–1294. https://doi.org/10.5047/eps.2013.09.006

Robinson, R. M., Zhang, Y., Anderson, B. J., Zanetti, L. J., Korth, H., & Fitzmaurice, A. (2018). Statistical relations between field-aligned currents and precipitating electron energy flux. *Geophysical Research Letters*, *45*(17), 8738–8745. https://doi.org/10.1029/2018GL078718

Sato, N., Wright, D. M., Carlson, C. W., Ebihara, Y., Sato, M., Saemundsson, T., et al. (2004). Generation region of pulsating aurora obtained simultaneously by the FAST satellite and a Syowa-Iceland conjugate pair of observatories. *Journal of Geophysical Research*, *109*(A10). https://doi.org/10.1029/2004JA010419

Smith, A. R. A., & Pačes, M. (2022). Python tools for ESA's Swarm mission: VirES for Swarm and surrounding ecosystem. *Frontiers in Astronomy and Space Sciences*, *9*(October), 1–10. https://doi.org/10.3389/fspas.2022.1002697

Smith, A. R. A., Pačes, M., & Santillan, D. (2023). ESA-VirES/VirES-Python-Client [Software]. Zenodo. https://doi.org/10.5281/zenodo.10372683

Stasiewicz, K., Bellan, P., Chaston, C., Kletzing, C., Lysak, R., Maggs, J., et al. (2000). Small scale Alfvenic structure in the aurora. *Space Science Reviews*, *92*(3–4), 423–533. https://doi.org/10.1023/A:1005207202143/METRICS

Strangeway, R. J., Elphic, R. C., Peria, W. J., & Carlson, C. W. (2000). FAST observations of electromagnetic stresses applied to the polar ionosphere. In *Geophysical monograph series* (Vol. 118, pp. 21–29). https://doi.org/10.1029/GM118P0021

Thayer, J. P., & Semeter, J. (2004). The convergence of magnetospheric energy flux in the polar atmosphere. *Journal of Atmospheric and Solar-Terrestrial Physics*, *66*(10), 807–824. https://doi.org/10.1016/j.jastp.2004.01.035

Walker, S. J., Laundal, K., Reistad, J. P., Ohma, A., Hatch, S. M., Chisham, G., & Decotte, M. (2023). A comparison of auroral oval proxies with the boundaries of the auroral electrojets. *Space Weather*. https://doi.org/10.22541/essoar.170515970.00907705/v1

Wu, J., Bryant, M. S., Ridley, C. G., Shen, Y., Yang, L., Clausen, L. B., et al. (2017). A comparison of small-scale magnetic fluctuations in the Region 1 and 2 field-aligned current systems. *Journal of Geophysical Research: Space Physics*, *122*(3), 3277–3290. https://doi.org/10.1002/2016JA023453

Wu, J., Knudsen, D. J., Gillies, D. M., & Burchill, J. K. (2020). Swarm survey of Alfvénic fluctuations and their relation to nightside field-aligned current and auroral arc systems. *Journal of Geophysical Research: Space Physics*, *125*(3), 1–19. https://doi.org/10.1029/2019JA027220

Xiong, C., & Lühr, H. (2014). An empirical model of the auroral oval derived from CHAMP field-aligned current signatures – Part 2. *Annales Geophysicae*, *32*(6), 623–631. https://doi.org/10.5194/angeo-32-623-2014

Xiong, C., Lühr, H., Wang, H., & Johnsen, M. G. (2014). Determining the boundaries of the auroral oval from CHAMP field-aligned current signatures – Part 1. *Annales Geophysicae*, *32*(6), 609–622. https://doi.org/10.5194/angeo-32-609-2014

Xiong, C., Stolle, C., Alken, P., & Rauberg, J. (2020). Relationship between large-scale ionospheric field-aligned currents and electron/ion precipitations: DMSP observations. *Earth Planets and Space*, *72*(1). https://doi.org/10.1186/s40623-020-01286-z

Zhang, Y., & Paxton, L. J. (2008). An empirical Kp-dependent global auroral model based on TIMED/GUVI FUV data. *Journal of Atmospheric and Solar-Terrestrial Physics*, *70*(8–9), 1231–1242. https://doi.org/10.1016/j.jastp.2008.03.008

21699402, 2024, 2, Downloaded from https://agupubs.onlinelibrary.wiley.com/doi/10.1029/2023JA032191 by UNIVERSITY OF BERGEN, Wiley Online Library on [07/02/2024]. See the Terms and Conditions (https://onlinelibrary.wiley.com/terms-and-conditions) on Wiley Online Library for rules of use; OA articles are governed by the applicable Creative Commons License

Paper III

Revealing the effect of Earth's rotation on geospace

Margot Decotte, Karl M. Laundal, Josephine A. Salice, Spencer M. Hatch, Stein Haaland, Anders Ohma
Submitted to Nature Communications on 15-March-2024

Graphic design: Communication Division, UiB / Print: Skipnes Kommunikasjon AS

uib.no

ISBN: 9788230854341 (print)
9788230849934 (PDF)